Supplemental Information: Photochemical post-functionalization of polystyrene enables accelerated chemical recycling

Stanley Lo[a,b], Angela Lin[a], Cher Tian Ser[a,b], Alán Aspuru-Guzik[a,b,c,d,e,f,g,h,i,*], Helen Tran[a,d,e,*]

[a]Department of Chemistry, University of Toronto, 80 St. George St., Toronto, ON M5S 3H6, Canada

[b]Vector Institute for Artificial Intelligence, W1140-108 College St., Schwartz Reisman Innovation Campus, Toronto, ON M5G 0C6, Canada

[c]Department of Computer Science, University of Toronto, 40 St George St., Toronto, ON M5S 2E4, Canada

[d]Department of Chemical Engineering and Applied Chemistry, University of Toronto, Toronto, ON, M5S 3E5, Canada

[e]Acceleration Consortium, 700 University Ave., Toronto, ON M7A 2S4, Canada

[f]Department of Materials Science and Engineering, University of Toronto, ON M5S

3E4, Canada

[g]Institute of Medical Science, 1 King's College Circle, Medical Sciences Building, Room 2374, Toronto, ON M5S 1A8, Canada

[h]Senior Fellow, Canadian Institute for Advanced Research (CIFAR), 661 University Ave., Toronto,

ON M5G 1M1, Canada

[i]NVIDIA, 431 King St. W #6th, Toronto, ON M5V 1K4, Canada

Correspondence: aspuru@utoronto.ca, and tran@utoronto.ca.

Table of Contents

Supplementary Tables

Supplementary Fig.

Materials

Polystyrene PS-2934-S (M_w = 6.4kg/mol, Polymer Source Inc.), polystyrene dimer (M_w = 266.2 g/mol, Polymer Source Inc.), polystyrene standard A-1000 (M_w = 1.12kg/mol, Tosoh Co.), polystyrene standard F-1 (M_w = 10kg/mol, Tosoh Co.), polystyrene standard F-2 (M_w = 19.6kg/mol, Tosoh Co.), polystyrene standard F-4 (M_w = 40.4kg/mol, Tosoh Co.), polystyrene standard F-10 (M_w = 110kg/mol, Tosoh Co.), 2-(4-Isopropylphenyl)-4,4,5,5-tetramethyl-1,3,2-dioxaborolane (96%, Ambeed, Inc.), N-(Trifluoromethylthio)phthalimide (98%, TCI America, Inc.), potassium carbonate (K_2CO_3) (99%, Fisher Scientific), 1,3,5-trimethoxybenzene (99%, Sigma Aldrich), 4,4'-difluorobenzophenone (4,4-DFBP) (99%, Sigma Aldrich), 2,4,5,6-Tetra(9H-carbazol-9-yl)-1,3-Dicyanobenzene (4CzIPN) (97%, Ambeed, Inc.), anhydrous acetonitrile (99.8%, Sigma Aldrich), anhydrous 1,2-dichloroethane (99.8%, Sigma Aldrich), anhydrous tetrahydrofuran (99.9% inhibitor-free, Sigma Aldrich), anhydrous chloroform (99% 0.5-1.0% ethanol as stabilizer, Sigma Aldrich), anhydrous ethyl acetate (99.8%, Sigma Aldrich), anhydrous propylene carbonate(99.7%, Sigma Aldrich), anhydrous benzene (99.8%, Sigma Aldrich), anhydrous N-methylpyrrolidone (99.5%, Sigma Aldrich), anhydrous dichloromethane (99.8%, Sigma Aldrich), anhydrous acetone (99.8% Extra Dry AcroSeal™, ThermoFisher Scientific),cyclohexane (99% ACS grade, Sigma Aldrich), ethyl acetate (99.5% ACS grade, Sigma Aldrich), water (HPLC grade, Sigma Aldrich), hexane (98.5% ACS grade, Fisher Scientific), chloroform (99.8% ACS grade, Sigma Aldrich), methanol (99.8% ACS grade, Millipore Sigma), acetonitrile (HPLC grade, Sigma Aldrich), anti-static Styrofoam peanut (ULINE), deuterated chloroform (99.8%, Sigma Aldrich), deuterated dimethyl sulfoxide (99.9%, Sigma Aldrich), silver trifluoroacetate (99.99%, Sigma Aldrich), trans-2-[3-(4-tert-butylphenyl)-2-methyl-2-propenylidene]malononitrile (DCTB) (98%, TCI America, Inc.), 3Å molecular sieves (Sigma Aldrich), Silica gel (technical grade, 230-400 mesh, Supelco), formic acid (88% ACS grade, VWR Chemicals BDH), tetrahydrofuran (99.9% inhibitor-free, Sigma Aldrich), dichloromethane (99.5% ACS grade, Sigma Aldrich), TOYOPEARL® HW-55F Bulk Media (Supelco).

Instrument Information

Photoreactor: The Kessil PhotoReaction PR160L-370 Gen 2 (max 44W) was placed horizontally 4cm away from the reaction vessel at 100% intensity. A fan was placed above the reaction vessel for cooling.

Normal-phase preparative chromatography (FLASH): The BUCHI Pure C-810 FLASH was used to purify Isopropylbenzene-SCF_3-Bpin and all the polymer samples. The EcoFlex Silica 25g column was used for purification with ACS grade hexane (small molecule), ACS grade cyclohexane (polymers), and ACS grade ethyl acetate (small molecule and polymers) as the eluent. The parameters were manually input using the BUCHI Pure software.

Gel permeation chromatography (GPC): Number average molecular weight (M_n), weight average molecular weight (M_w), and dispersity (Đ) were characterized by gel permeation chromatography (GPC) on a Tosoh EcoSEC instrument (model HLC-8320 version 2.01) equipped with two Tosoh TSKgel SuperHM-M columns and a dual-flow refractive-index detector. HPLC (high performance liquid chromatography) grade THF (tetrahydrofuran) stabilized with 250 ppm BHT (butylated hydroxytoluene) and 2.5 g/L tetrabutylammonium

bromide was used as the eluent at 40 °C with a flow rate of 0.6 mL/min. The system was calibrated against monodisperse polystyrene standards and data processing was performed using the EcoSEC Data Analysis software (version 1.14). Samples within a study were all measured on the same day. Data was normalized to the highest intensity peak.

Preparative Recycling GPC (rGPC): The LaboACE LC-7080 Plus Series preparative recycling GPC was used to purify p(CP-hexyl). The instrument is equipped with JAIGEL-1-H-F and JAIGEL-2-H-F columns, using ACS 99% reagent grade chloroform with 10 mL/min flow rate and dual UV and RI detectors. The parameters were controlled via the JAI Scan software.

Manual column chromatography with TOYOPEARL® HW-55F Bulk Media: The TOYOPEARL® HW-55F Bulk Media was transferred from the original matrix to THF. The media was packed into a 250mL manual column. The sample was dissolved in minimal THF and liquid loaded onto the media. The purification process was monitored via thin-layer chromatography.

Reverse-phase preparative liquid chromatography (PrepLC): The Agilent 1260/1290 Infinity II PrepLC System was used to purify the small molecule product, Isopropylbenzene-SCF_3-Bpin, at 100mg scale. The Agilent 5 Prep-C18 50x21.2mm was the column equipped for separation. HPLC grade water with 0.1% formic acid and HPLC grade acetonitrile was used as the eluent.

Reverse-phase liquid chromatography coupled with electrospray Ionization (LC-MS): The Agilent 1260/1290 Infinity II LC System coupled with the InfinityLab LC/MSD was used to characterize and quantify the small molecule product, Isopropylbenzene-SCF_3-Bpin. The instrument is equipped with the Agilent ZORBAX Rapid Resolution High-Definition SB-C18 (1.8 µm) column for separation and heated to 40°C. The Infinity LC/MSD is a single quadrupole equipped with an electrospray ionization source (ESI). HPLC grade water with 0.1% formic acid and HPLC grade acetonitrile was used as the eluent. Prior to injection, the samples were filtered through a 0.22µm PTFE filter.

Nuclear magnetic resonance spectroscopy (NMR): ^{1}H, ^{13}C and ^{19}F nuclear magnetic resonance (NMR) spectra were recorded on a Bruker Ascend NMR 400 MHz spectrometer with a liquid N_2-cooled cryoprobe at 25 °C. Quantitative ^{19}F NMR was collected with a pulse angle of 30° using the reported T1 time of the internal standard (T1 = 2.4 seconds), 4,4'-difluorobenzophenone, and then setting the d_1 of consequent ^{19}F spectra to at least seven times the length of that T1 (d_1 = 20 seconds). Chemical shifts for all NMR spectra reported in parts per million (ppm) and were referenced to residual protonated solvent ($CDCl_3$: δ 7.26 for ^{1}H, DMSO-d_6: δ 2.50 for ^{1}H, and 4,4`-difluorobenzophenone: δ -105.8 for ^{19}F).

Matrix-assisted laser desorption ionization (MALDI): The Bruker Autoflex Speed was used for matrix-assisted laser desorption ionization time-of-flight mass spectrometer (MALDI-TOF/MS). Reflectron mode and positive polarity was used. The instrument is equipped with a 2kHz frequency tripled Nd:YAG laser (λ = 355 nm). The samples were prepared with stock solutions of polymer (5mg/mL), DCTB matrix (10mg/mL), and silver trifluoroacetate as the cationization agent (20mg/mL) in THF. The ideal ratio was 2:60:1 of polymer:matrix:cationization agent. Data was normalized to the highest intensity peak.

Gas chromatography coupled with electron ionization (GC-MS): The Thermo ISQ-7000 GC/MS coupled with electron ionization mode was used to identify functionalization on PS dimer, and the composition of the distillation products. The carrier gas was Helium. The column

temperature starts at 150°C and ends at 250°C. Samples were dissolved in CH_2Cl_2 at 10ppm and ionized with positive polarity. Data was normalized to the highest intensity peak.

Direct Analysis in Real Time Mass Spectrometry (DART): The JEOL AccuTof Plus 4G mass spectrometer was used for DART. Samples were dissolved in $CHCl_3$ at ~1mg/mL and ionized with positive polarity.

Thermogravimetric analysis coupled with electron ionization (TGA-MS): The Netzsch STA449 F5 Jupiter with automatic sample changer coupled to QMS 403 Aeolos Quadro was used to study the depolymerization kinetics of PS and PS-SCF_3. The analysis was carried out in cupolas made of alumina oxide. The MS is a quadrupole mass spectrometer that can measure between 1 – 300 amu. 5mg of sample is weighed for every measurement.

Ultraviolet-visible Spectroscopy (UV-Vis): UV-Vis (ultraviolet – visible) spectra of all compounds and polymers were recorded on the Agilent Cary 7000 UV-Vis-NIR Universal Measurement spectrophotometer (spectral range 170 - 3000 nm, double beam instrument). A 100% transmittance sample was recorded as a blank using $CHCl_3$ in a quartz cuvette.

Fluorescence Spectrophotometry: The PerkinElmer FL6500 was used to measure photoluminescence of samples. The excitation wavelength was 365nm, and the samples were dissolved in $CHCl_3$.

Density functional theory calculations: As the depolymerization occurs in the solid/melt phase, toluene was chosen as a model solvent to approximate the chemical environment that the proposed processes take place. Each structure was subjected to a conformational search using CREST v3.0.1,[1–3] with structural energies evaluated by the GFN2-xTB[4] semiempirical quantum chemical method using the ALPB solvation model for toluene.[5] The 50 lowest energy conformers were selected for further refinement via a single-point energy calculation at the PBE0-D4/def2-SVP level of theory,[6–11] and with the C-PCM implicit solvation model accounting for toluene (ε = 2.387).[12] The lowest energy conformer identified this way was subjected to full geometry optimization and frequency calculations at the same level of theory. All energy minima and transition states were verified to possess zero and one negative frequency respectively, and the thermochemical analysis was performed at 573 K. Finally, a single-point energy calculation was performed on the optimized structure at the DLPNO-CCSD(T1)/def2-TZVP level of theory,[13–20] and the CPCM implicit solvation model for toluene. All DFT calculations were performed using ORCA v6.0.0.[21–27] The reported ΔH_{573K} and ΔG_{573K} values are obtained from the combination of the DLPNO-CCSD(T1)/def2-TZVP single-point energy with the enthalpic and entropic corrections from the PBE0-D4/def2-SVP level of theory. Solvated-phase corrections[28] to the ideal gas approximation used in the calculation of entropy were applied to each structure's final Gibbs free energy at 573 K ($RT\ln(RT/p^\circ)$ = 40.34kJ/mol). Computed structures and energies are available on https://iochem-bd.matter.toronto.edu.

General Methods

%-SCF_3 functionalization determination on post-functionalized polystyrene.

To determine the approximate % functionalization of SCF_3 on PS, we acquired ^{19}F qNMR and compare the integration of PS-SCF_3 to the internal standard 4,4'-difluorobenzophenone (4,4-DFBP). There are two assumptions made: 1) the polymer sample is 100% pure, and 2) the mass of the polymer's end-group is negligible. Although some polymer samples have trace impurities (i.e., grease, water, and solvent) as shown by ^1H NMR, we continue the approximation of %-SCF_3 functionalization as we do not expect these impurities to contribute significantly to peak integrations. We measure 5mg of sample with a microbalance, add 100µL of $CDCl_3$, and add 100µL of a stock solution of 10mg/mL (0.0458mmol/mL) 4,4-DFBP in $CDCl_3$. Using the following equations, we can approximate the %-SCF_3 functionalization:

$$n_{PS-SCF3} = \frac{I_{PS-SCF3}}{I_{2F-BP}} \times \frac{N_{2F-BP}}{N_{PS-SCF3}} \times \frac{m_{2F-BP}}{M_{2F-BP}}$$

$$n_{PS} = \frac{(m_{sample} - (n_{PS-SCF3} \times M_{PS-SCF3}))}{M_{PS}}$$

$$mol\ \%SCF3\ functionalization = \frac{n_{PS-SCF3} \times 100\%}{n_{PS} + n_{PS-SCF3}}$$

Where I = integration of ^{19}F NMR peak, N = number of fluorines, M = molecular weight, m = mass, PS-SCF_3 refers to one unit of styrene that is functionalized with SCF_3 ($M_{PS\text{-}SCF3}$ = 204.2g/mol).

% Yield of Monomer Conversion

Similar to the description above, to determine the amount of styrene, we acquire ^1H qNMR and compare the integration of styrene to the internal standard 1,3,5-trimethoxybenzene (1,3,5-TMB). We add approximately 1mL of $CDCl_3$ to the reaction vial/cannula/collection vial and add 0.1mL of a stock solution of 0.1M of 1,3,5-TMB.

$$m_{styrene} = \frac{I_{styrene}}{I_{1,3,5-TMB}} \times \frac{N_{1,3,5-TMB}}{N_{styrene}} \times \frac{M_{styrene}}{M_{1,3,5-TMB}} \times m_{1,3,5-TMB}$$

Experimental Studies

Safety Note

The risk of exposure to high intensity low wavelength UV light was mitigated by wearing UV safety goggles and containing the light within aluminum foil barriers. Aside from the light hazard, no unexpected or unusually high safety hazards were encountered.

Solvent Screening Study on Isopropylbenzene-Bpin (small molecule model system for polystyrene)

To synthesize 4,4,5,5-tetramethyl-2-(4-(2-((trifluoromethyl)thio)propan-2-yl)phenyl)-1,3,2-dioxaborolane (Isopropylbenzene-SCF_3-Bpin), the general method was adapted. 2-(4-Isopropylphenyl)-4,4,5,5-tetramethyl-1,3,2-dioxaborolane (Isopropylbenzene-Bpin) was used as the benzylic C-H small molecule substrate for solvent screening. K_2CO_3 was placed in a 2-dram vial and dried in a vacuum oven at 120^{o}C overnight. Isopropylbenzene-Bpin, Phth-SCF_3, and 4CzIPN were placed in a 2-dram vial in the glovebox vacuum antechamber overnight. The vials were vacuum cycled 3 times prior to adding solvent. The solvents were added to the respective vial and then combined into one reaction vial. The reaction mixture was stirred at 1400rpm under the irradiation of one 45W 365nm LED (approximately 4.0cm from the bulb) for 16h, under a cooling fan at ~35^{o}C (measured by handheld infrared gun). A 100µL aliquot of the reaction was diluted by 1mL of MeCN and further analyzed via LC-MS.

To prepare the linear calibration of the product, Isopropylbenzene-SCF_3-Bpin was synthesized via the aforementioned procedure. The crude mixture was dry-loaded onto silica gel and purified by flash column chromatography on silica gel (95% hexane: 5% ethyl acetate); R_f: 0.5 (90% hexane: 10% ethyl acetate); and further purified by preparative HPLC (MeCN: H_2O with 1% v/v formic acid).

ESI-MS m/z calculated for $C_{16}H_{22}BF_3O_2S$ [M+H]+ = 347.15; found = 347.2

Fig. S1. [1]H qNMR of Isopropylbenzene-SCF_3-Bpin.

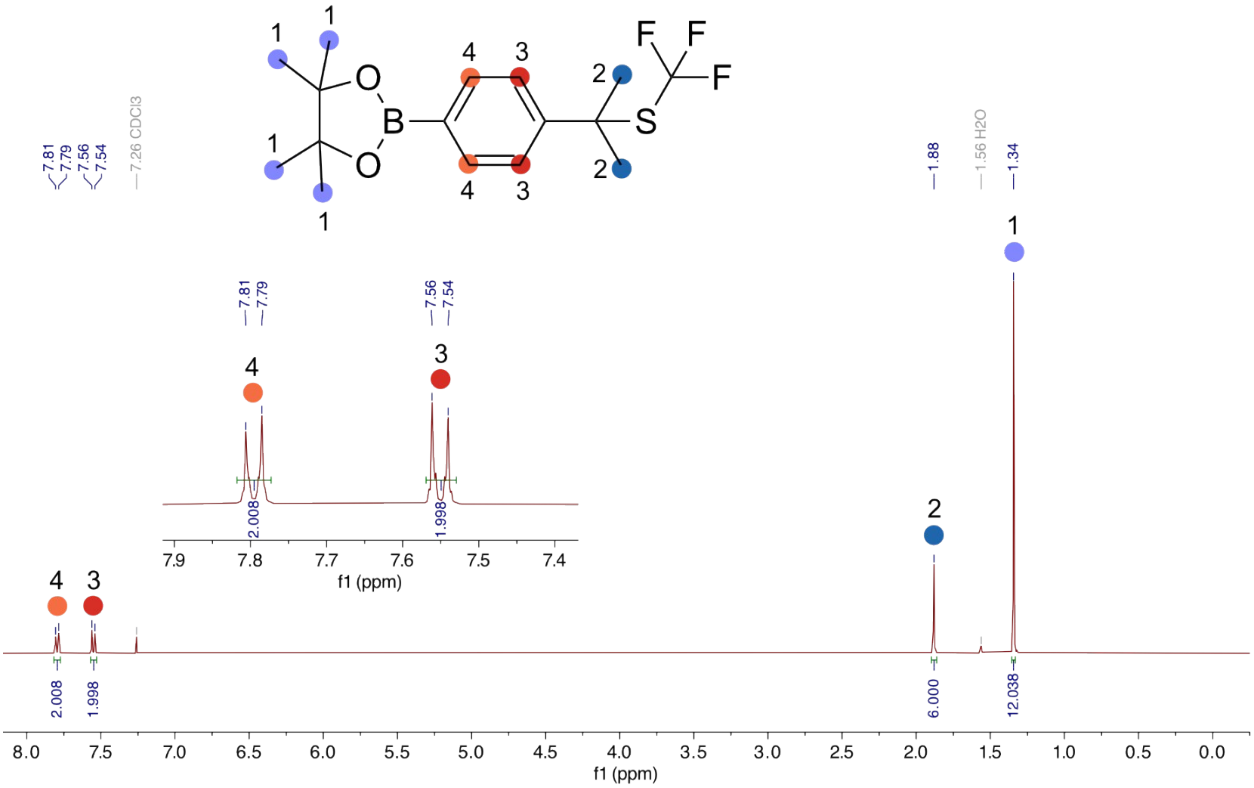

[1]H NMR (400 MHz, $CDCl_3$) δ 7.80 (d, *J* = 8.4 Hz, 2H), 7.55 (d, *J* = 8.4 Hz, 2H), 1.88 (s, 6H), 1.34 (s, 12H).

Fig. S2. [13]C NMR of Isopropylbenzene-SCF_3-Bpin.

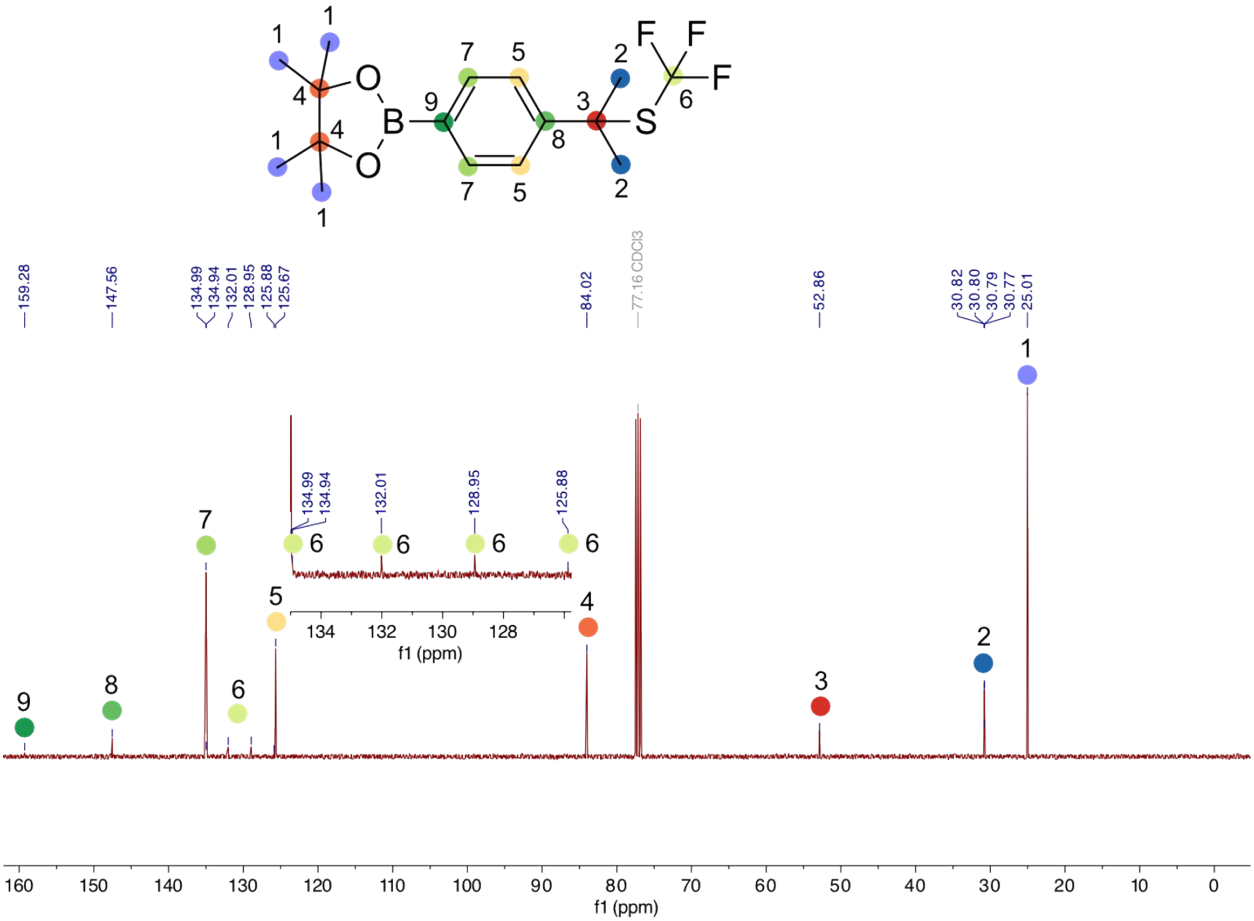

^{13}C NMR (101 MHz, $CDCl_3$) δ 159.28, 147.56, 134.99, 130.48 (q, J = 308.76 Hz), 125.67, 84.02, 52.86, 30.80 (q, J = 1.6 Hz), 25.01.

Fig. S3. ^{19}F NMR of Isopropylbenzene-SCF_3-Bpin.

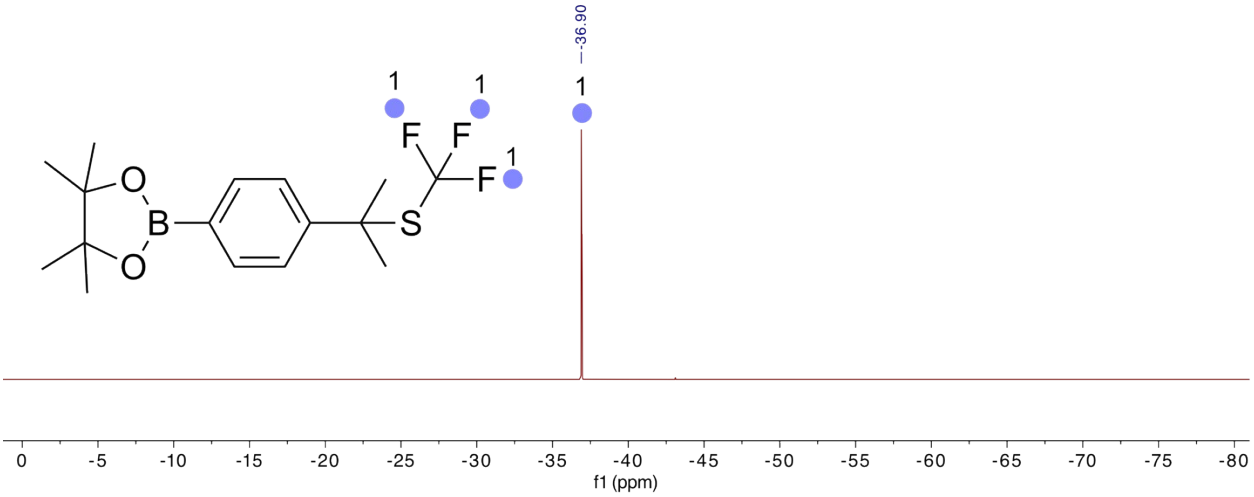

^{19}F NMR (376 MHz, $CDCl_3$) δ -36.90.

Fig. S4. Linear Calibration of Isopropylbenzene-SCF_3-Bpin on the HPLC.

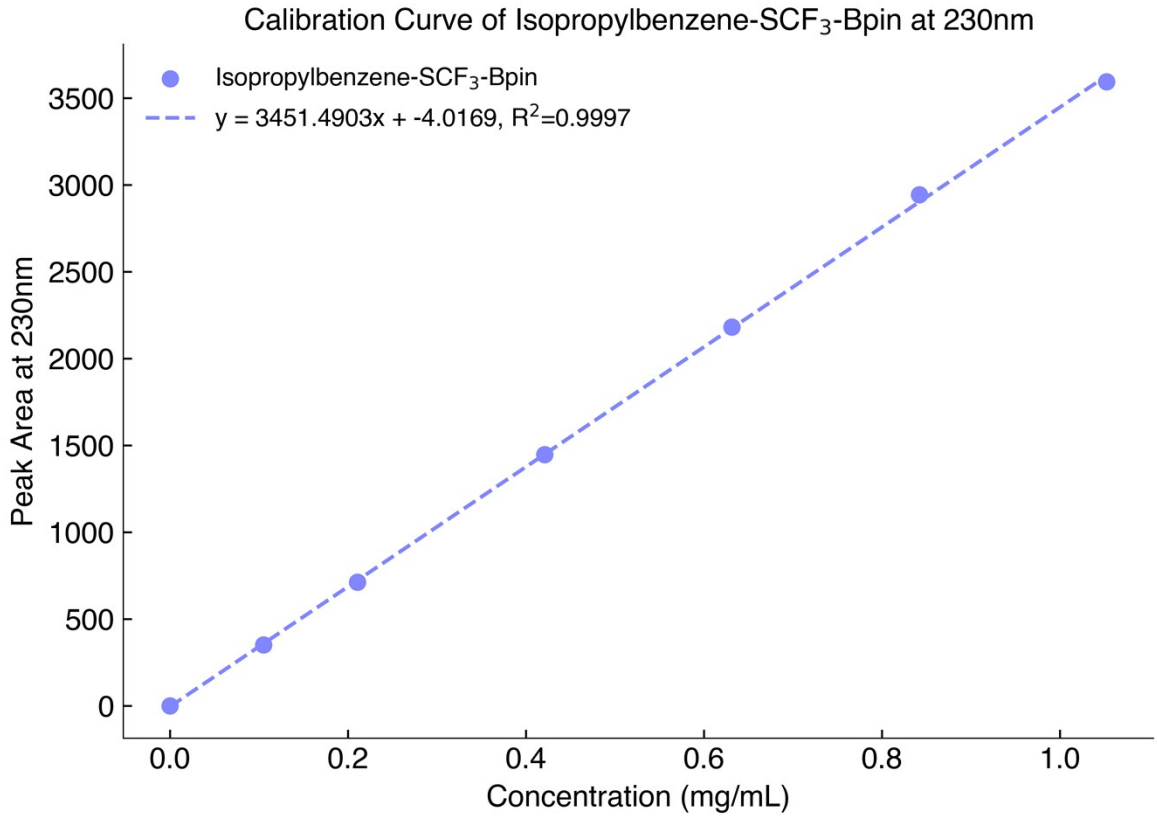

The reaction screening samples were analyzed via HPLC, and the yield was determined with the linear calibration provided in **Fig. S4**.

Exploring experimental conditions to reduce crosslinking of the PS-SCF_3 functionalization.

When the optimized trifluoromethylthiolation reaction condition for isopropylbenzene-Bpin was applied to PS (**Figure 2b**, entry 14), uncontrolled and undesirable crosslinking occurred between polymer chains as observed by gel permeation chromatography (GPC) traces and visual observation of insoluble solids formed (**Fig. S5**). This crosslinking occurred primarily when post-functionalizing higher molecular weight PS (M_n > 50 kg/mol), where insoluble solids formed during the reaction and a higher number-averaged molecular weight (M_n) peak (at least twice the starting material's M_n, **Fig. S5**) were observed by GPC. Initially, we hypothesized that this was due to the benzylic radicals on the PS backbone recombining between chains, in alignment with the proposed mechanism by Xu et al.[33] However, we observed that the electrophilic SCF_3 source (2-((trifluoromethyl)thio)isoindoline-1,3-dione, Phth-SCF_3) must be present in the reaction to observe crosslinking (**Table S1**, Entry 22-23). We found that a greater amount of K_2CO_3 reduced the extent of crosslinking. For all the subsequent studies, we used the optimized reaction condition (0.1 equivalence of Phth-SCF_3 which was modified with 1.0 equivalent of K_2CO_3 instead of 0.2 equivalent as shown in **Fig. 2c**.

We observe the formation of significantly higher M_n peaks (2x the starting material M_n) by GPC. We suspect that this can be explained by crosslinking of PS. According to the mechanism proposed by Xu et al., the benzylic radical is formed on PS which has the potential to crosslink with another PS chain that has the benzylic radical.[29] The recombination of the two benzylic radicals is highly improbable because the lifetime of these two radicals must be greater than the rate of diffusion (on the order of milliseconds). In addition, the proposed mechanism claims that the benzylic radical can be formed without Phth-SCF_3. To prove that it is unlikely for two benzylic radical PS chains to crosslink, we perform a control study without the presence of Phth-SCF_3. The observed M_n of the product does not change despite the lack of Phth-SCF_3 (**Fig. S5**). However, with the addition of Phth-SCF_3, the presence of the higher M_n peak is present. Furthermore, the higher M_n peak decreases in M_n, peak area, and the extent of fronting as more K_2CO_3 is added (**Fig. S5**). However, K_2CO_3 is hygroscopic which tends to introduce more water into the reaction despite our stringent protocols, increasing the amount of impurity functionalization as discussed in the section of O_2 vs. water experiment on PS (Table S2, **Fig. S7-8**). We found that there is a saturation point at which adding more K_2CO_3 does not largely affect the extent of crosslinking. We conclude that 1 eq. of K_2CO_3 is sufficient, which will be used for the rest of the reactions in this study.

Table S1. Results and reaction conditions for reaction optimization to reduce crosslinking.

Entry	**PS-10K (eq. by monomer)**	**4CzIPN (eq.)**	**Phth-SCF_3 (eq.)**	**K_2CO_3 (eq.)**	**Reaction Time (hrs)**	**Solvent**	**Normalized Peak Intensity of Crosslinking Peak by GPC**	**^{19}F-NMR (I_{-40ppm} : I_{-60ppm})***
1	1	0.02	0	0.025	4	MeCN:1,2-DCE (1:1), 5mL	N/A (0)	N/A
2	1	0.02	0.125	0.025	4	MeCN:1,2-DCE (1:1), 5mL	0.1903	1:0.064
3	1	0.02	0.125	0.125	4	MeCN:1,2-DCE (1:1), 5mL	0.1618	1:0.09
4	1	0.02	0.125	0.25	4	MeCN:1,2-DCE (1:1), 5mL	0.1312	1:0.08
5	1	0.02	0.125	0.5	4	MeCN:1,2-DCE (1:1), 5mL	0.1103	1:0.11
6	1	0.02	0.125	1	4	MeCN:1	0.0888	1:0.15

						,2-DCE (1:1), 5mL		
7	1	0.02	0.125	6	4	MeCN:1 ,2-DCE (1:1), 5mL	0.0534	1:0.65

*Ratio between the integration of the product peak (PS-SCF_3, -40ppm), and the impurity peak (-60ppm).

Fig. S5. GPC overlay of the reaction crude from the reaction optimization to reduce crosslinking.

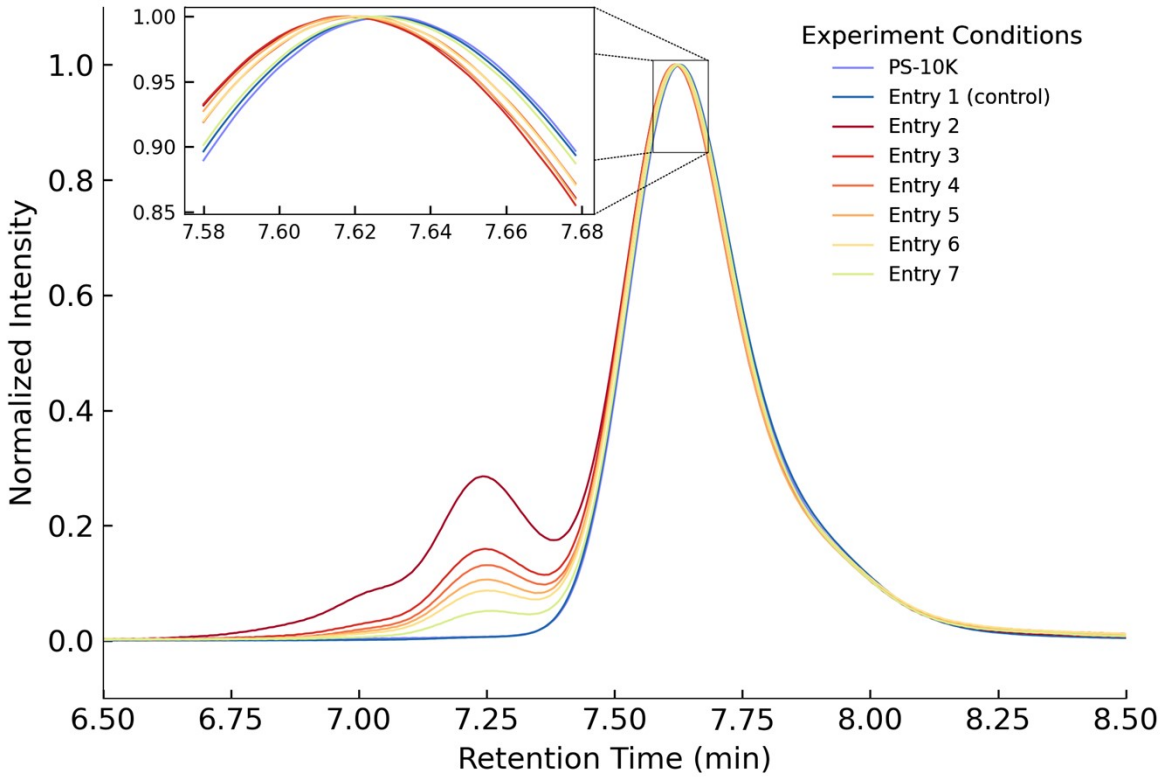

Evaluating the purification methods for Polystyrene SCF_3.

The crude reaction was concentrated under vacuo, re-dissolved in minimal $CHCl_3$, and precipitated into methanol. The precipitate was divided into three parts for separate purification using the three different methods (i.e., FLASH, rGPC, and toyopearls).

Table S2. Results from the purification technique comparisons.

Entry	Method of purification	PS-6.4K (mmol)	4CzIPN (mmol)	Phth-SCF_3 (mmol)	K_2CO_3 (mmol)	Reaction Time (hrs)	Volume of MeCN (mL)	Volume of 1,2-DCE (mL)	% yield by mass
1		3	0.0075	0.375	0.075	16	7.5	7.5	N/A
	FLASH								96.8
	rGPC								85.2
	toyopearls								71.1

*Reagent equivalents differ from the rest of the study because this experiment was performed earlier, prior to reaction optimization from Table S1 (crosslinking study).

Fig. S6. Stacked ^1H NMR of PS-SCF_3 after the three separate purification methods.

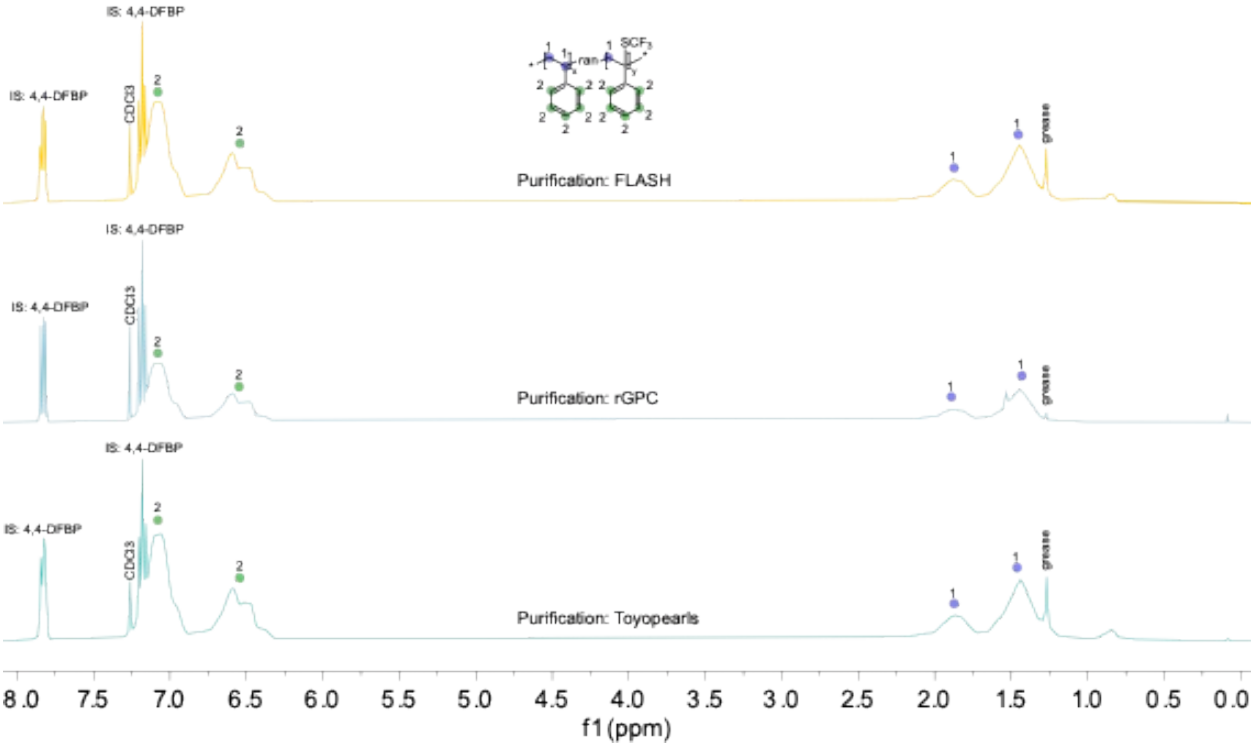

Fig. S7. Stacked ^{19}F NMR of PS-SCF_3 after the three separate purification methods.

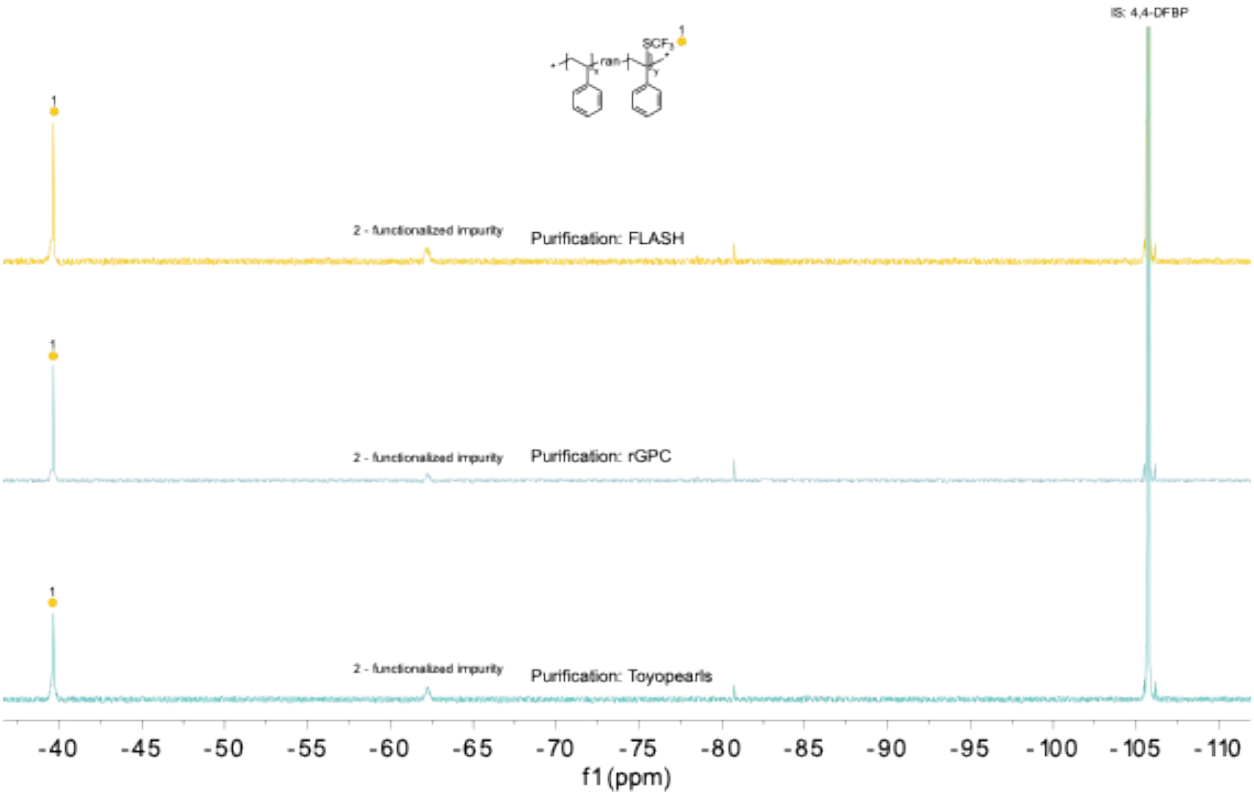

Fig. S8. Stacked GPC of PS-SCF_3 after the three separate purification methods.

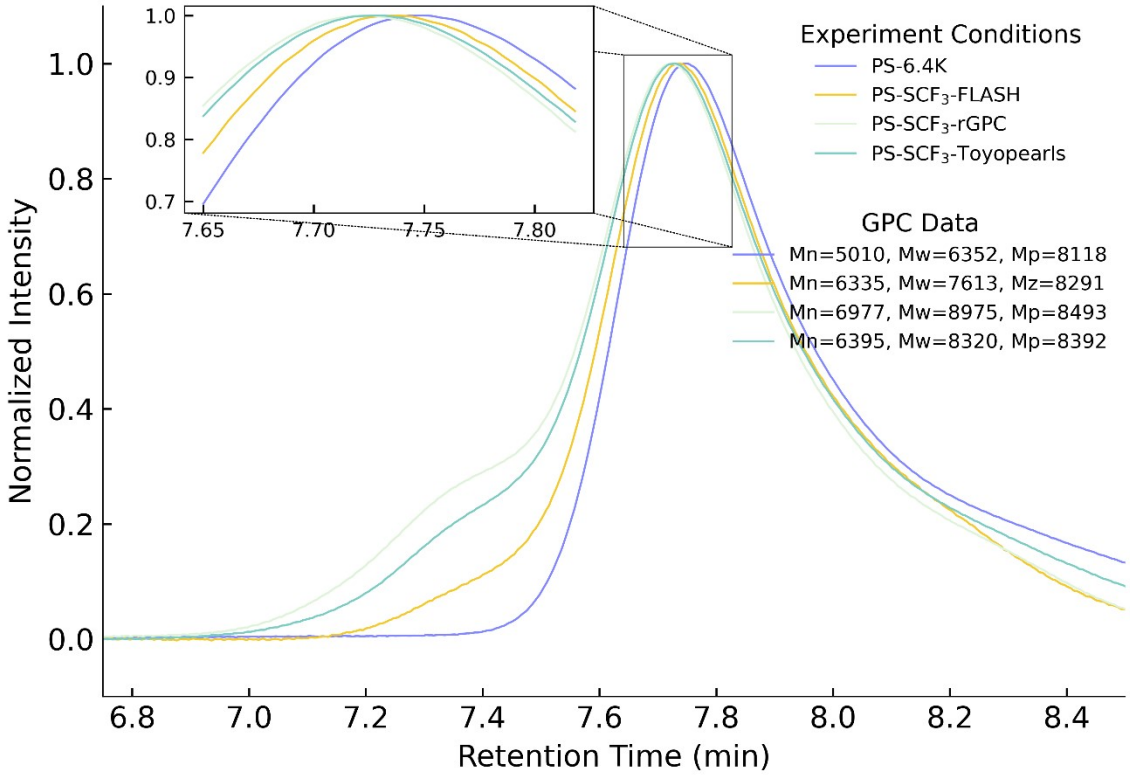

Fig. S9. UV-vis and Photoluminescence of 4CzIPN, PS-6.4K, and PS-SCF_3 after the three separate purification methods.

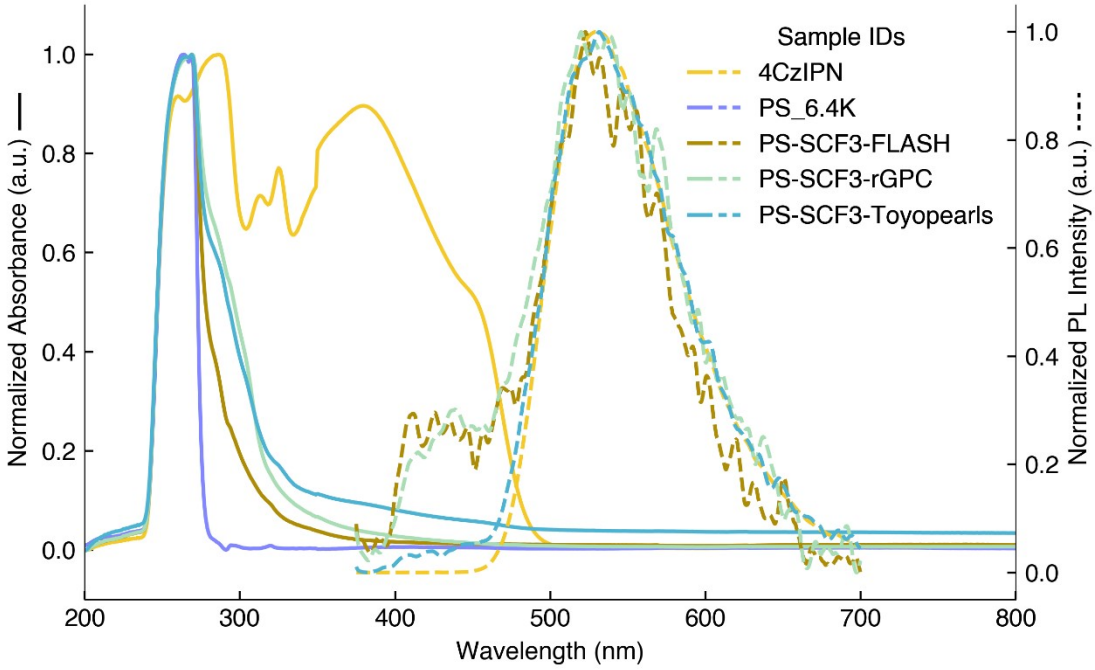

Fig. S10. Isothermal TGA at 300°C of PS-SCF_3 after using the FLASH, rGPC, and toyopearl purification methods.

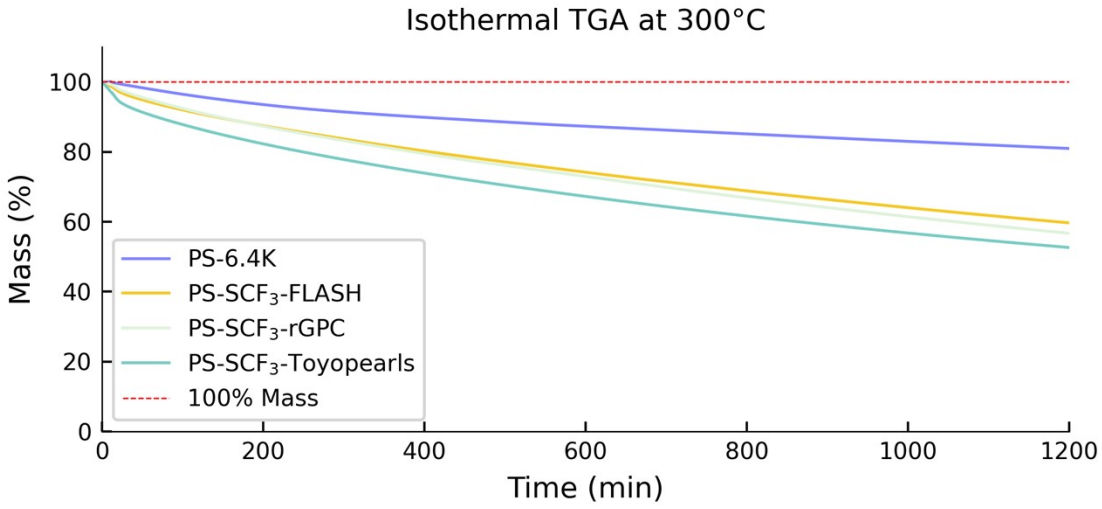

O_2 vs Water Experiment on Polystyrene

Specific protocol modifications to the oxygen-water control studies:

The following reactions were performed in a round bottom flask (RBF). K_2CO_3 was flame-dried in an RBF under Ar atmosphere, using a Schlenk line. PS (PS-2934-S, M_w=6.4kg/mol), PhthSCF$_3$, and 4CzIPN were subsequently added and the RBF was vacuum cycled 3 times.

Table S3, Entry 1 (H_2O + O_2): ACS grade MeCN (5mL), and ACS grade 1,2-dichloroethane (5mL), and 0.1mL of HPLC H_2O were added into the RBF. The dissolved oxygen in the solvents is considered sufficient for assuming the presence of oxygen.

Table S3, Entry 2 (H_2O + no O_2): Anhydrous MeCN (5mL), anhydrous 1,2-dichloroethane (5mL), and 0.1mL of HPLC H_2O were added into the RBF. The RBF was freeze-pump-thawed 3 times to remove any dissolved oxygen.

Table S3, Entry 3 (No H_2O + O_2): Activated 3Å molecular sieves were added to ACS grade MeCN (5mL) and ACS grade 1,2-dichloroethane (5mL) for two days to remove residual water. The dissolved oxygen in the solvents is considered sufficient for assuming the presence of oxygen.

Table S3, Entry 4 (No H_2O + no O_2): The RBF was capped with a septum and transferred into the N_2 glovebox. Anhydrous MeCN (5mL) and anhydrous 1,2-dichloroethane (5mL) stored in the glovebox were added to the RBF.

Table S3. Reaction conditions for the O_2 vs. H_2O experiment on PS trifluoromethylthiolation.

Entry	**Atmosphere**	**PS-6.4K (mmol)**	**4CzIPN (mmol)**	**Phth-SCF$_3$ (mmol)**	**K_2CO_3 (mmol)**	**Reaction Time (hrs)**	**MeCN (mL)**	**1,2-DCE (mL)**	**HPLC H_2O (mL)**
1	ambient (O_2)	2	0.005	0.25	0.05	16	5	5	0.1
2	N_2	2	0.005	0.25	0.05	16	5	5	0.1
3	ambient (O_2)	2	0.005	0.25	0.05	16	5	5	0
4	N_2	2	0.005	0.25	0.05	16	5	5	0

Fig. S11. Stacked ^{1}H NMR of O_2 vs. H_2O Experiment on PS trifluoromethylthiolation in DMSO-d_6.

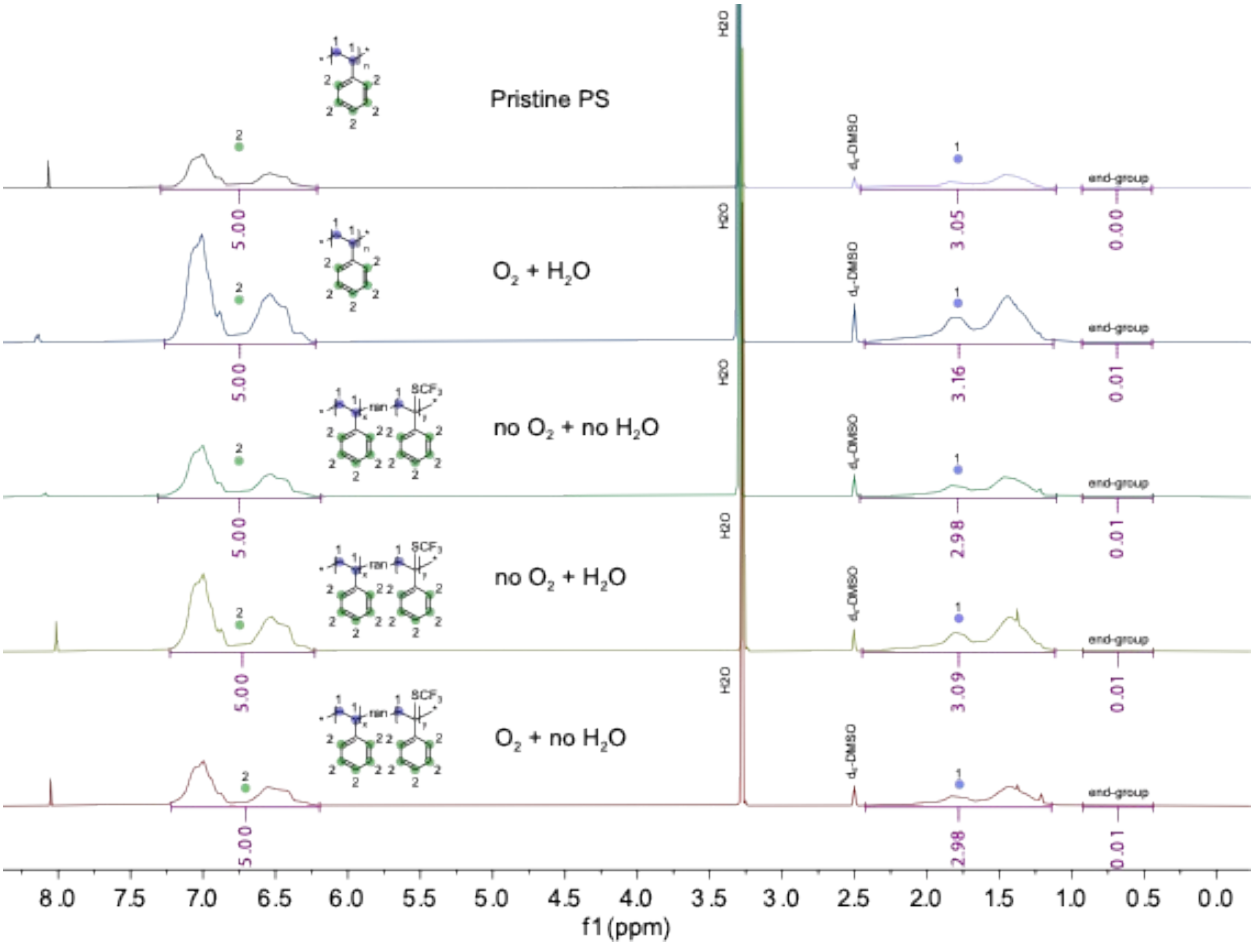

^{1}H qNMR (400 MHz, DMSO-d_6) δ 7.25 – 6.25 (br, 5H), 2.4 – 1.2 (br, 3H), 0.9 – 0.4 (br, 0H).

For the samples without H_2O in the photoreaction, the alkyl protons integrate to less than 3H when comparing to Pristine PS and the samples with H_2O in the photoreaction. This indicates higher functionalization in the alkyl region.

Fig. S12. Stacked ^{19}F NMR of O_2 vs. H_2O Experiment on PS trifluoromethylthiolation in DMSO-d_6.

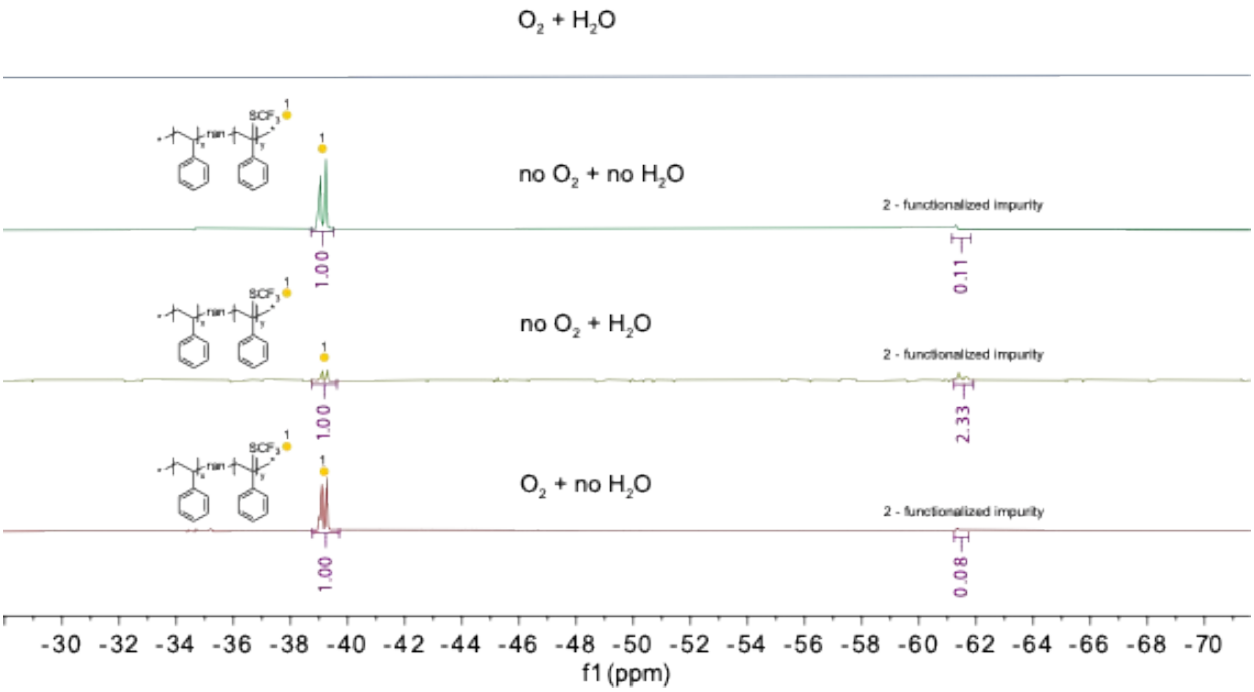

^{19}F NMR (376 MHz, DMSO-d_6) δ -38.94 (br), -39.13 (br), -61.41 (br).

Fig. S13. GPC of purified products from O_2 vs. H_2O Experiment on PS trifluoromethylthiolation.

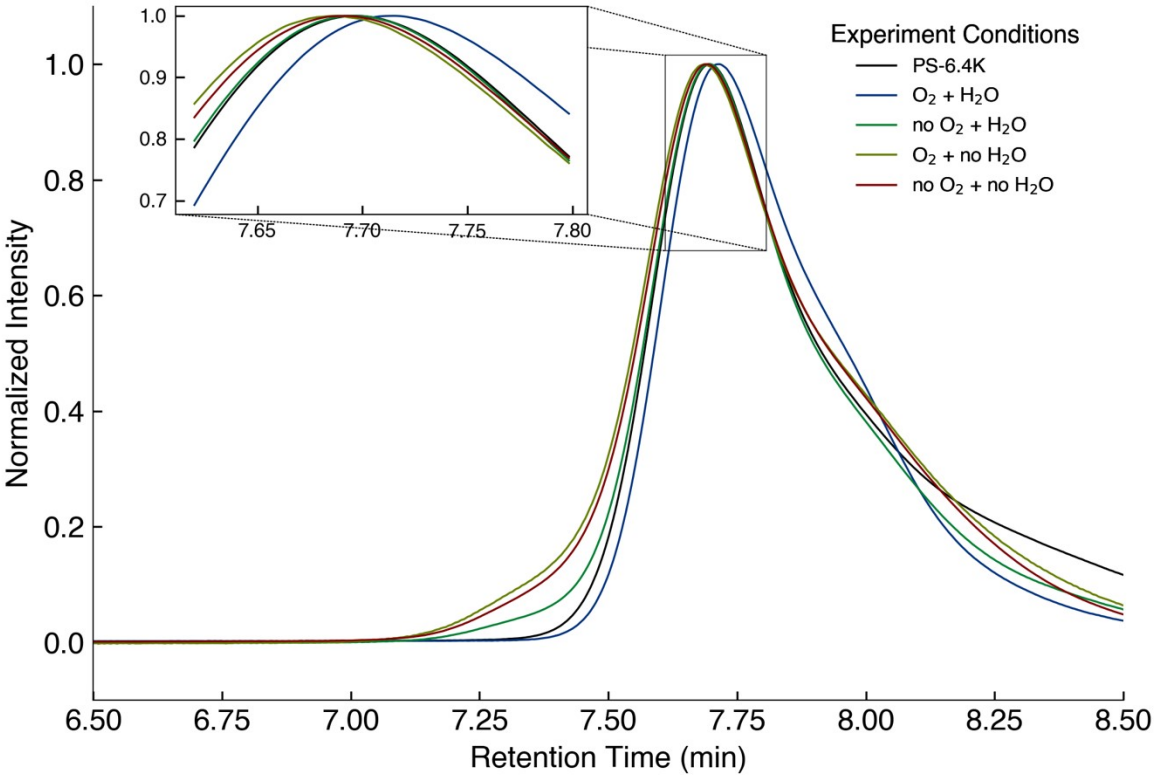

Impurity determination on PS Dimer

Table S4. Reaction conditions for the identification of SCF_3 and impurity functionalization on PS Dimer.

Entry	PS-Dimer (mmol)	4CzIPN (mmol)	$PhthSCF_3$ (mmol)	K_2CO_3 (mmol)	MeCN (mL)	1,2-DCE (mL)	HPLC H_2O (mL)	Reaction Time (hrs)
1	1	0.05	1.3	1	2.5	2.5	0	16
2	1	0.05	1.3	1	2.5	2.5	0.05	16

We found that the ^{19}F impurity was only present in PS samples, and the impurity peak increased with the addition of more K_2CO_3 which we suspect is due to greater H_2O contamination. The impurity was not found in reactions with Isopropylbenzene-Bpin. Thus, we used the PS dimer to study the identity of the impurity via ^{1}H and ^{19}F NMR, GC-MS, and DART.

We attempt to determine the impurity functionalized onto PS by adding H_2O to the reaction with the small molecule model system, and another reaction with a PS dimer. We only observe a significant formation of impurity with the PS dimer. We were unable to separate the SCF_3 functionalized dimer from the impurity functionalized dimer via FLASH, preparative liquid chromatography (prepLC), and gas chromatography coupled with mass spectrometry (GC-MS). Nevertheless, we analyze the purified fraction from prepLC using direct analysis in real time mass spectrometry (DART-MS) which offers the possibility of the functionalization of $-OSO_2F$, $-SCF_2(OH)$ (**Fig.** S22). However, according to literature reports of similar compounds, the observed ^{19}F NMR chemical shift does not match exactly (**Fig.** S14).[30,31] To this end, we hypothesized that these two products (including their regioisomers) may be the impurity functionalized onto the PS. Nevertheless, we minimized this impurity functionalization by reducing the amount of water present in the reaction using stringent protocols (i.e., overnight drying of reagents in vacuum oven, glovebox conditions, and 3Å molecular sieves in solvent dried overnight).

This increased shielding of F atoms relative to $-SCF_3$ likely arises from a reduced number of F atoms that mutually deshields each other and a modified local electronic environment induced by the oxygen-containing functional groups compared to F atoms.[48–50] Nevertheless, the backbone functionalization of $-OSO_2F$ or $-SCF_2(OH)$ could decrease or increase the rate of depolymerization based on their respective bond strengths (C-O: 358 kJ/mol, C-S: 272 kJ/mol).[51]

Fig. S14. Stacked ^{1}H NMR of PS-Dimer, PS-Dimer-SCF_3, and PS-Dimer (w/ functionalized impurity)

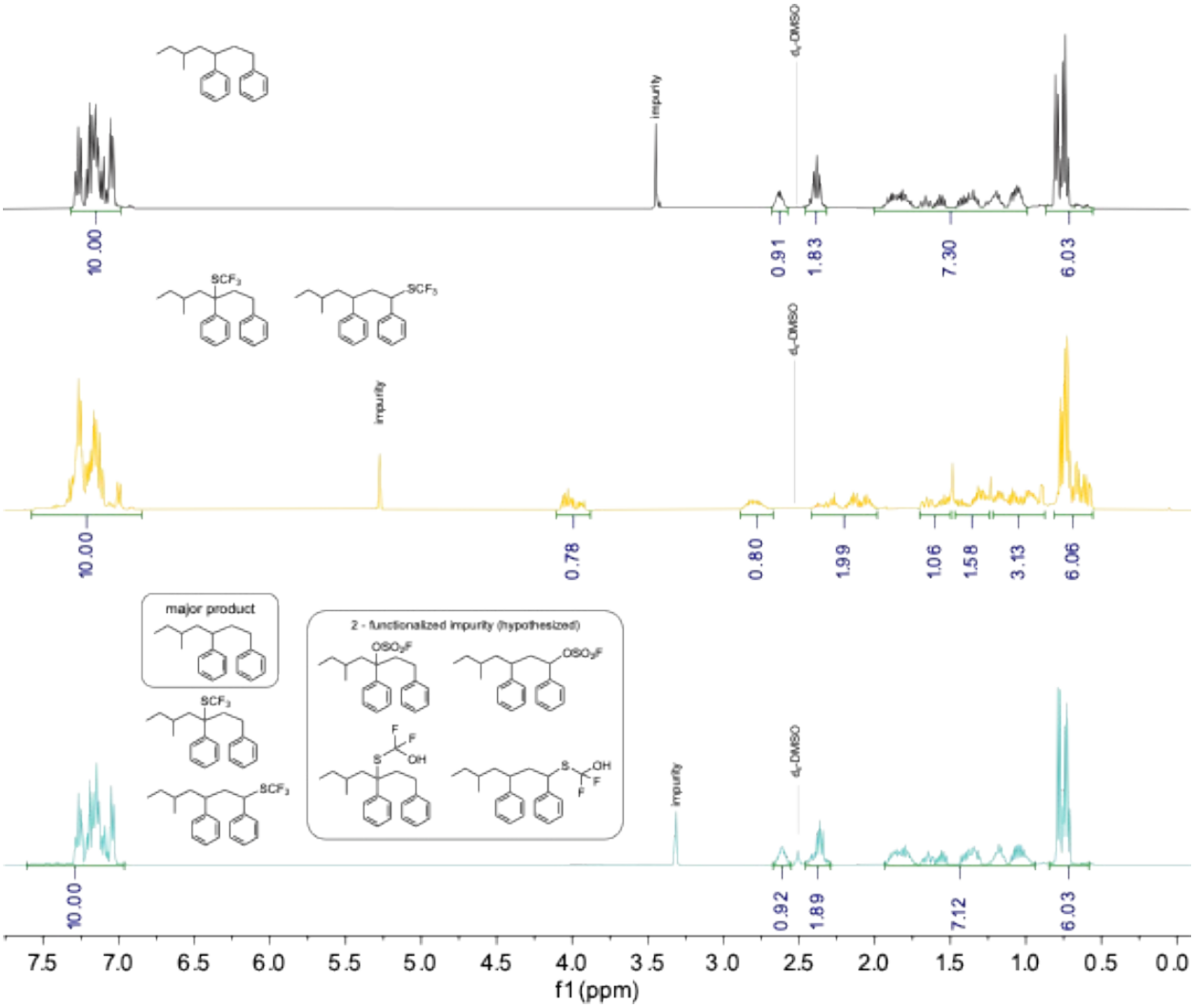

PS-Dimer [top]: ^{1}H NMR (400 MHz, DMSO) δ 7.35 – 7.00 (m, 10H), 2.61 (tq, *J* = 10.6, 5.5 Hz, 1H), 2.47 – 2.28 (m, 2H), 1.94 – 0.93 (m, 7H), 0.82 – 0.67 (m, 6H).

PS-Dimer-SCF_3 [middle]: ^{1}H NMR (400 MHz, DMSO) δ 7.46 – 6.93 (m, 10H), 4.09 – 3.90 (m, 1H), 2.89 – 2.67 (m, 1H), 2.44 – 1.97 (m, 2H), 1.71 – 0.86 (m, 5H), 0.81 – 0.55 (m, 6H).

PS-Dimer-SCF_3 (w/ functionalized impurity) [bottom]: ^{1}H NMR (400 MHz, DMSO) δ 7.35 – 7.00 (m, 10H), 2.61 (tq, *J* = 10.6, 5.5 Hz, 1H), 2.47 – 2.28 (m, 2H), 1.94 – 0.93 (m, 7H), 0.82 – 0.67 (m, 6H).

Fig. S15. Stacked ^{19}F NMR of Isopropylbenzene-SCF_3-Bpin, PS-Dimer-SCF_3, and PS-Dimer (w/ functionalized impurity).

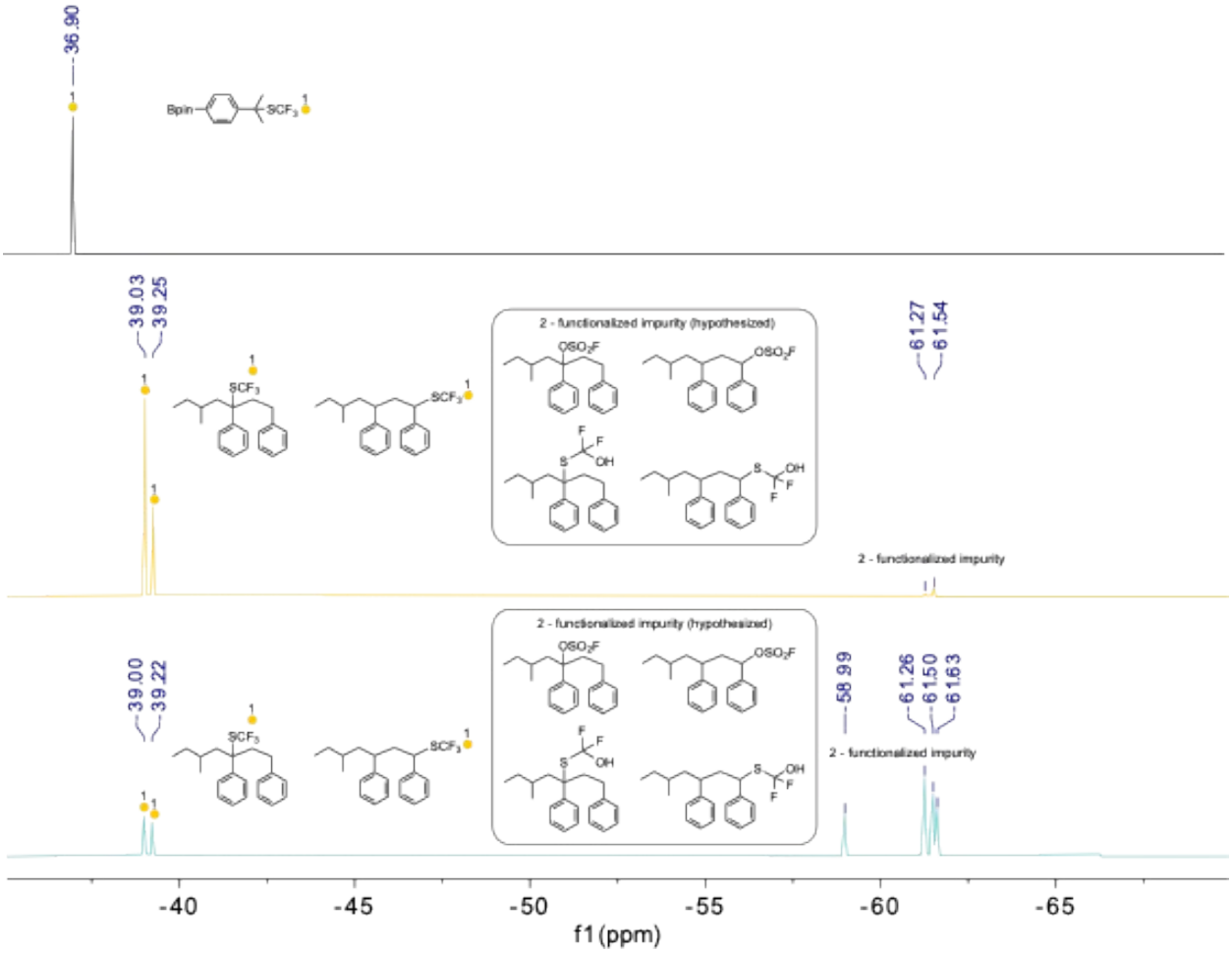

Isopropylbenzene-SCF_3-Bpin [top]: ^{19}F NMR (376 MHz, DMSO) δ -36.90.

PS-Dimer-SCF_3 [middle]: ^{19}F NMR (376 MHz, DMSO) δ -39.03 (s), -39.25 (s), -61.27 (s), -61.54 (s).

PS-Dimer (w/ functionalized impurity) [bottom]: ^{19}F NMR (376 MHz, DMSO) δ -39.00 (s), -39.22 (s), -58.99 (s), -61.26 (s), -61.5 (s), -61.63 (s).

Fig. S16. GC-MS (Total Ion Chromatogram) of the PS-Dimer.

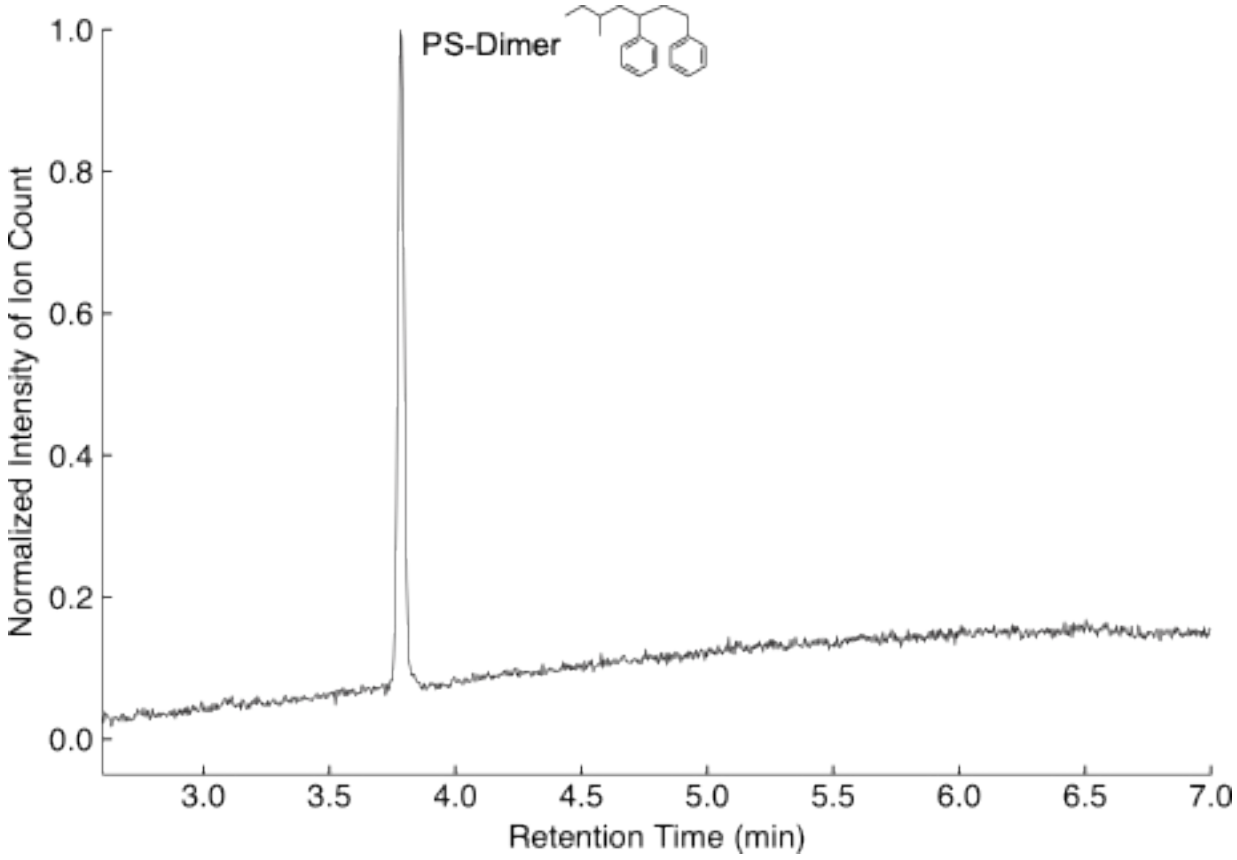

Fig. S17. MS of Peak at t=3.8min of GC of PS-Dimer.

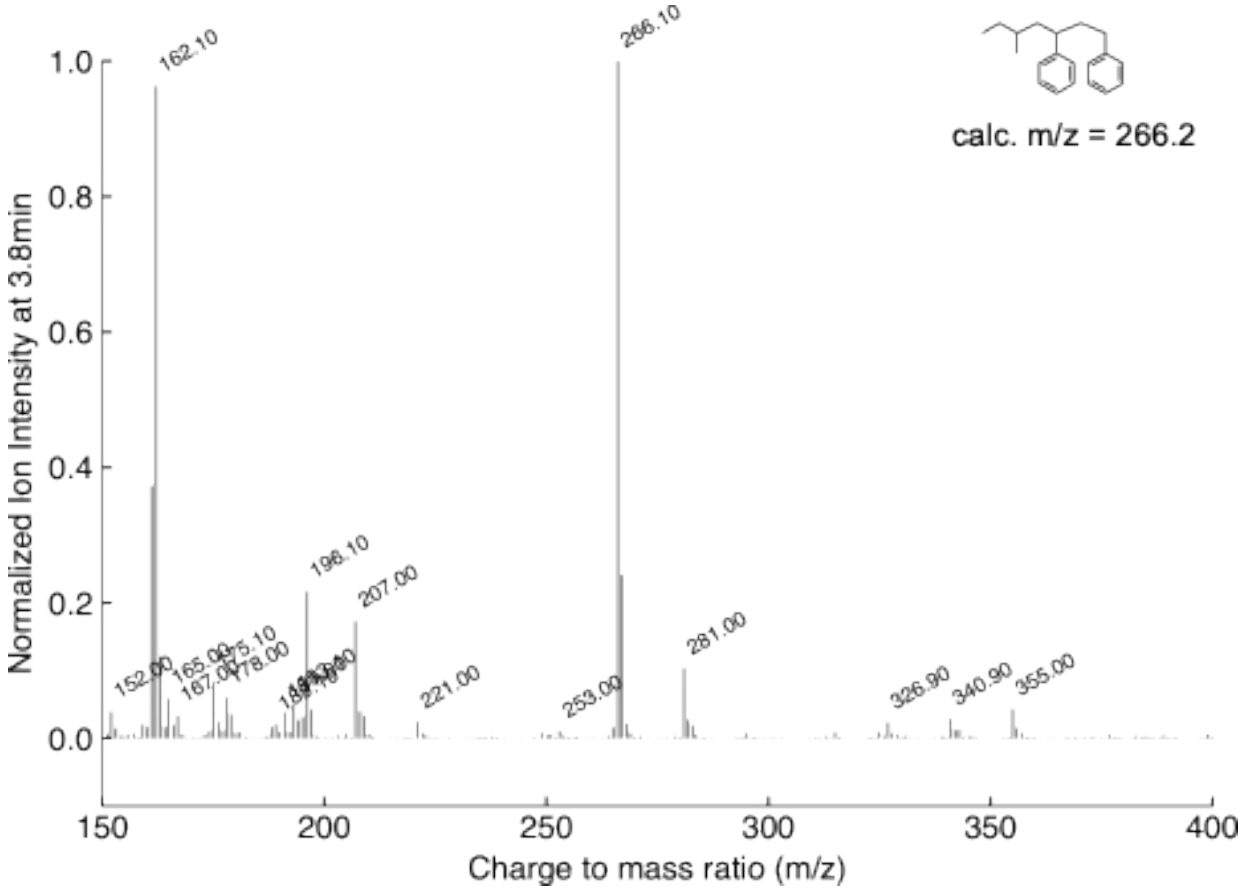

GC-MS (EI+): m/z [M]+ calculated for $[C_{20}H_{26}]$+ m/z 266.20, measured m/z 266.1.

Fig. S18. GC-MS (Total Ion Chromatogram) of PS-Dimer-SCF_3.

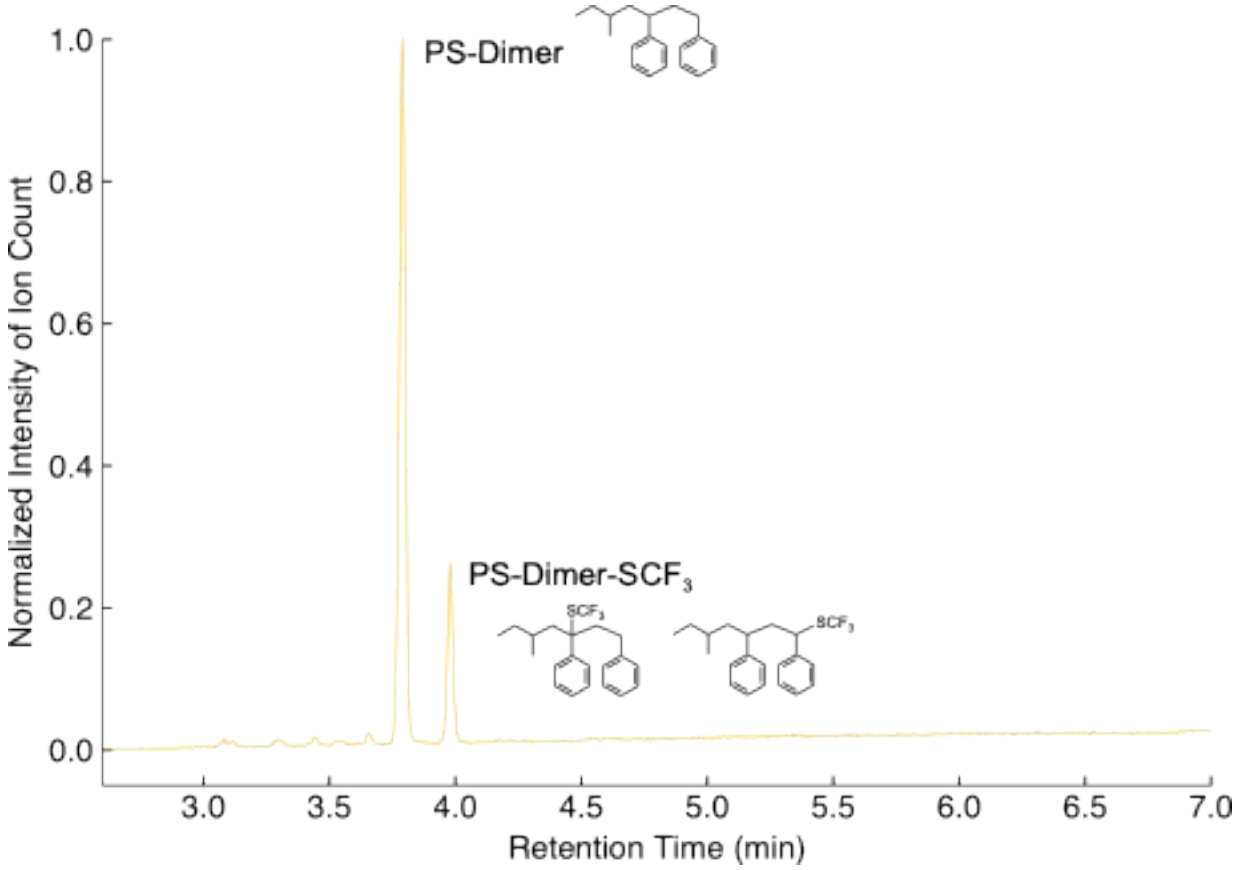

Fig. S19. MS of Peak at t=4.0min for the GC of PS-Dimer-SCF_3.

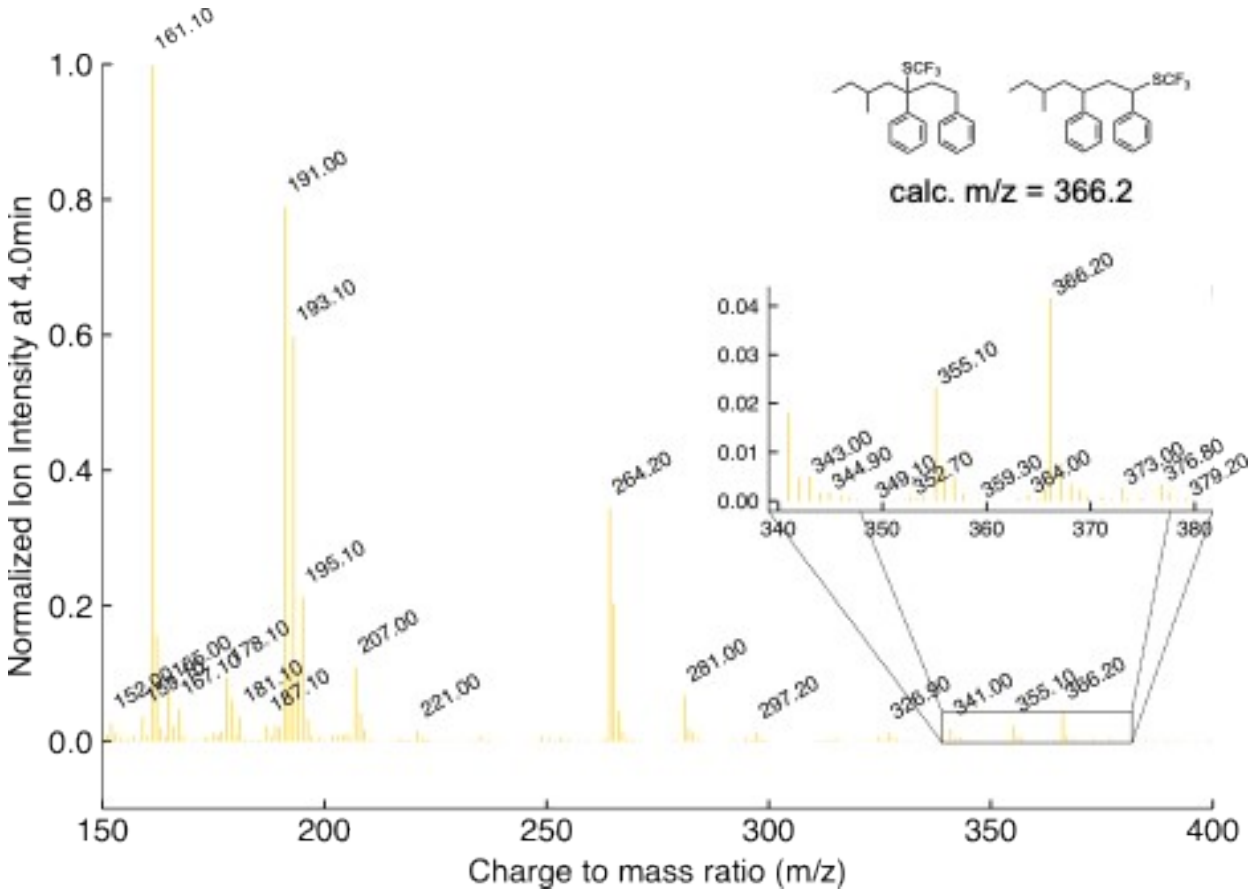

GC-MS (EI+): m/z $[M]^+$ calculated for $[C_{21}H_{25}SF_3]^+$ m/z 366.16, measured m/z 366.2.

Fig. S20. GC-MS (Total Ion Chromatogram) of PS-Dimer-SCF_3 (w/ functionalized impurity).

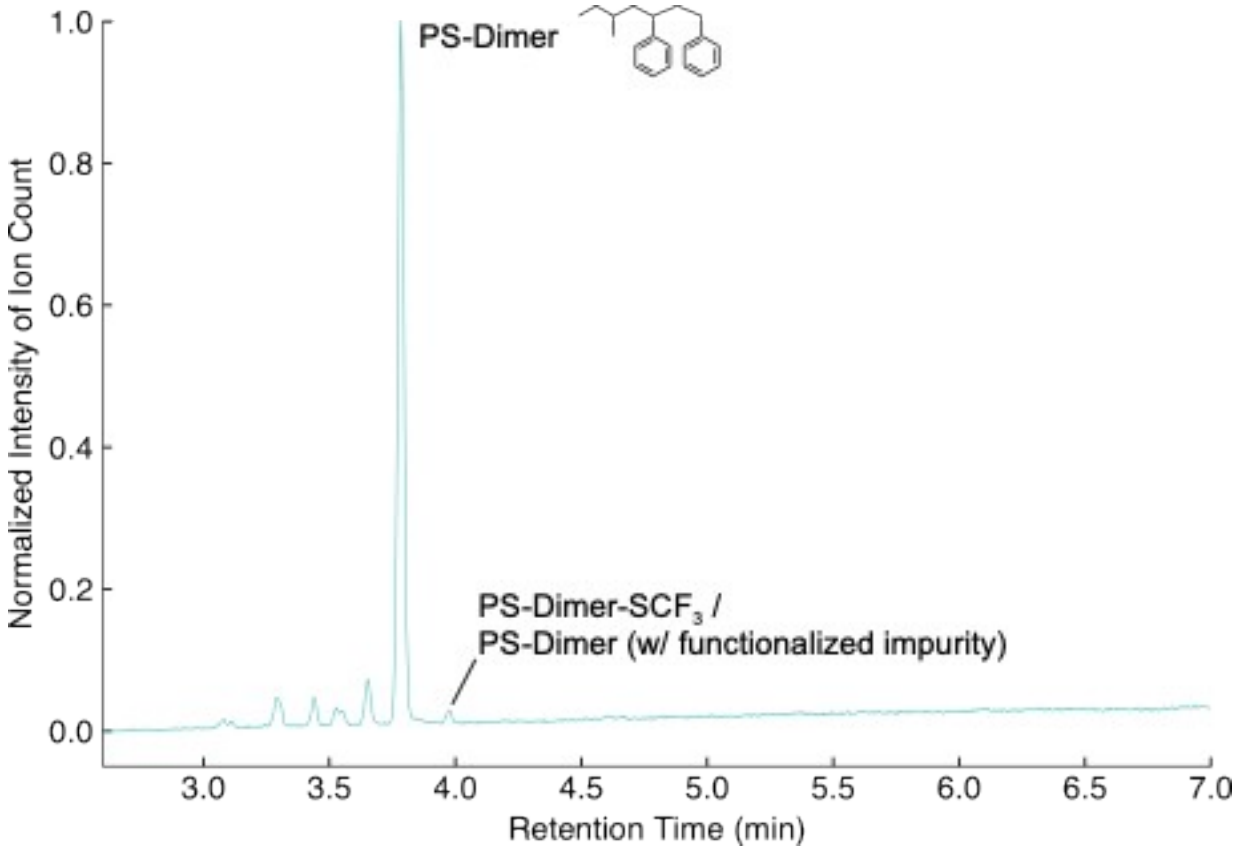

Fig. S21. MS of Peak at t=4.0min for the GC of PS-Dimer-SCF_3 (w/ functionalized impurity).

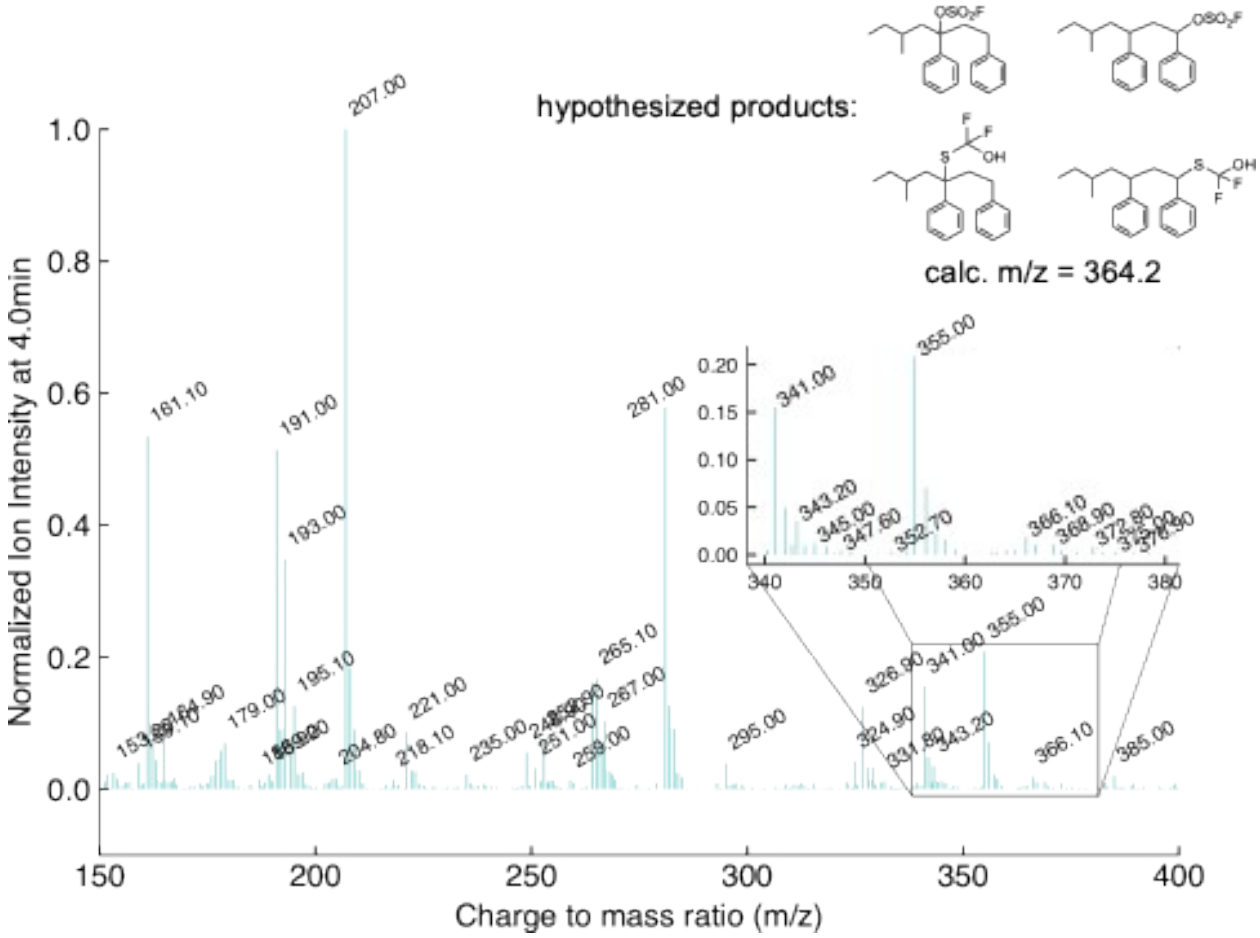

GC-MS (EI+): m/z $[M]^+$ calculated for $[C_{20}H_{25}SO_3F]^+$ m/z 364.15, $[C_{20}H_{25}SCF_2(OH)]^+$ m/z 364.16; measured trace m/z 364.1.

Note: Peaks at 3.1min, 3.3min, 3.4min, 3.5min, and 3.6min of the GC in **Fig.** S19 were analyzed but none of the masses were reasonable products.

Fig. S22. DART of PS-Dimer-SCF_3 (w/ functionalized impurity).

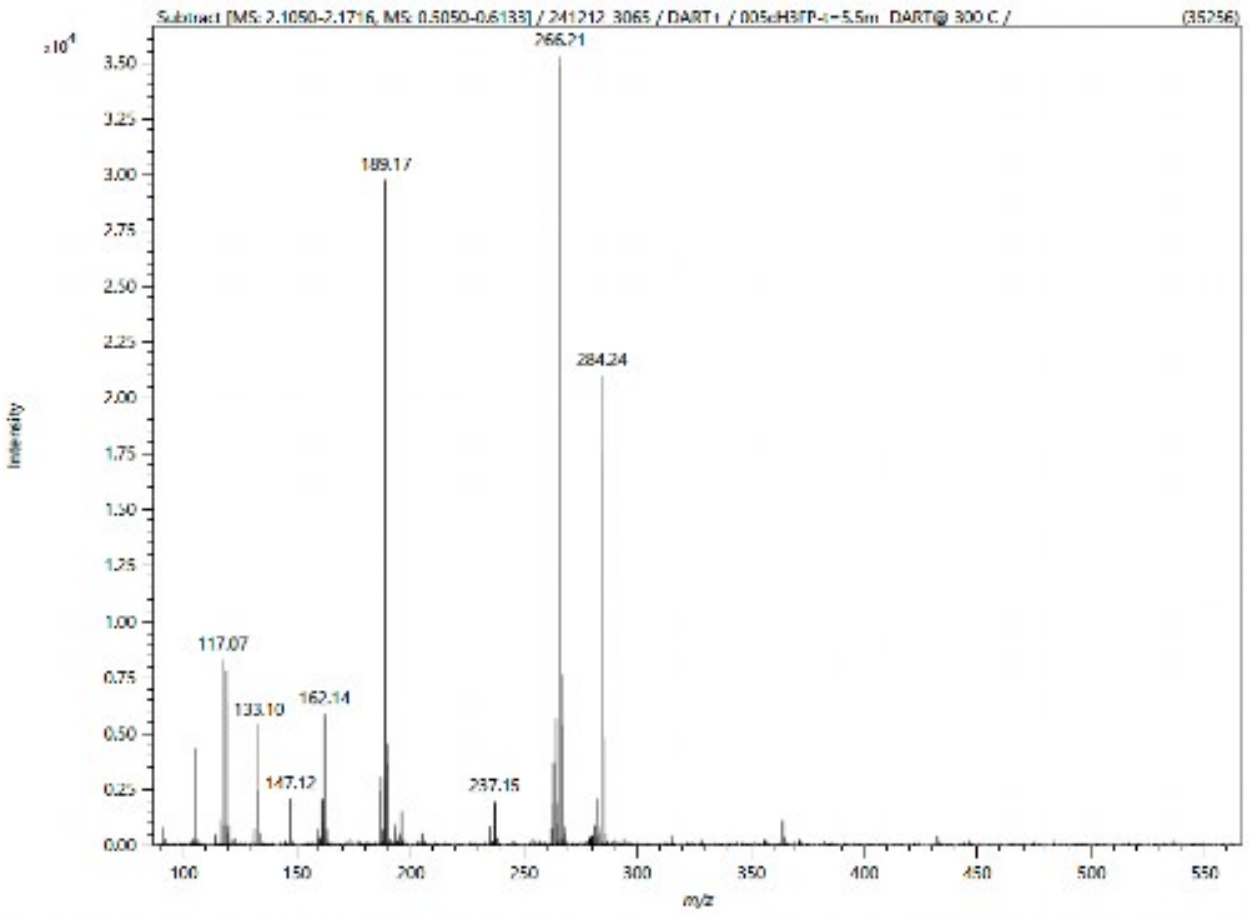

Fig. S23. DART between 330-410m/z of PS-Dimer-SCF_3 (w/ functionalized impurity).

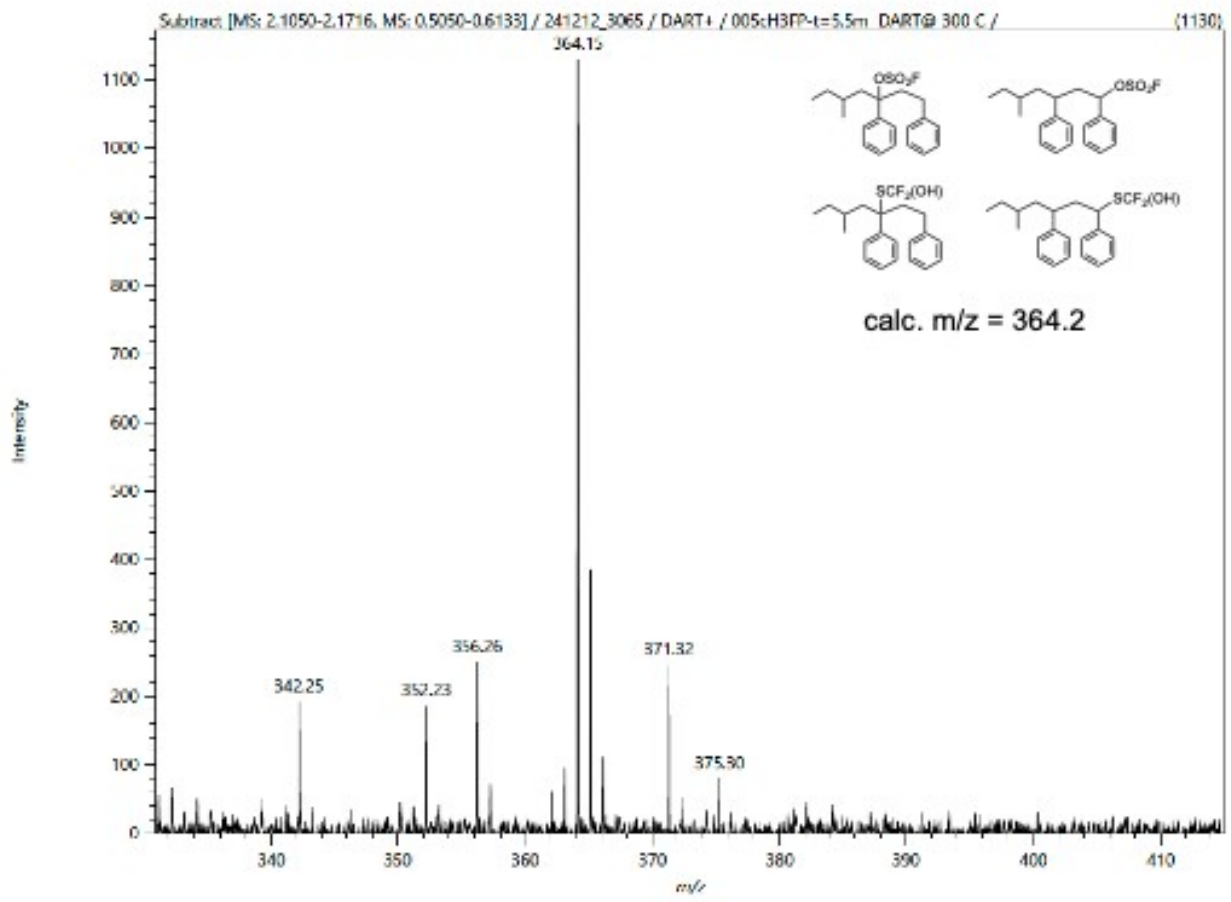

HRMS (DART-TOF+): m/z $[M]^+$ calculated for $[C_{20}H_{25}SO_3F]^+$ m/z 364.15, $[C_{20}H_{25}SCF_2(OH)]^+$ m/z 364.16; measured m/z 364.15.

Molecular Weight Study of PS-SCF_3.

The following samples were synthesized using the General Methods and optimized reaction conditions shown in **Fig. 2c**.

Table S5. Summary of GPC, mol% SCF_3-Functionalization, and Dynamic and Isothermal TGA at 300°C results of the Molecular Weight Study of PS.

Entry	Experiment ID	% yield by mass	M_n of PS (kg/mol)	SCF_3 Functionalization (mol%)	^{19}F-NMR (I_{-40ppm} : I_{-60ppm})*	Isothermal TGA at 300°C: % mass loss after 1200 minutes	Dynamic TGA: Onset temperature (°C)	Dynamic TGA: temperature of 98% depolymerization (°C)
1	PS-1.12K	n/a	0.7	n/a	n/a	43.1	350.7	278.4
2	PS-1.12K-SCF_3	90.3	0.9	1.70	1:0.009	59.8	318.8	282.1
3	PS-10K	n/a	8.5	n/a	n/a	25.6	355.9	340.0
4	PS-10K-SCF_3	112.6	9.5	0.20	1:0.225	58.5	345.4	315.0
5	PS-19.6K	n/a	16.7	n/a	n/a	31.4	356.5	341.8
6	PS-19.6K-SCF_3	77.5	17.2	0.14	1:0.303	51.7	349.3	321.2
7	PS-40.4K	n/a	34.6	n/a	n/a	52.5	356.1	340.3
8	PS-40.4K-SCF_3	77.9	33.8	0.09	1:0.692	57.1	348.6	322.8
9	PS-110K	n/a	94.0	n/a	n/a	32.0	361.6	345.1
10	PS-110K-SCF_3	58.6	84.9	0.04	1:2.166	42.2	353.2	325.8

*Ratio between the integration of the product peak (PS-SCF_3, -40ppm), and the impurity peak (-60ppm).

Unexpectedly, we noticed that the PS-10K and PS-19.6K samples exhibited significantly less mass loss than the lower and higher M_n PS samples (**Fig 3e**). Typically, higher M_n PS systems depolymerize slower because higher M_n PS has greater viscosity which lead to poor monomer diffusion, and lower chain-end concentrations that can offer efficient depolymerization.[32,33] Since we do not know the full synthesis and processing conditions of the PS standards, there may have been less weak links present in the PS-10K and PS-19.6K samples. Nevertheless, after post-functionalization of PS-10K and PS-19.6K, sufficient weak links were introduced to

promote mass loss similar to the other M_n samples. In addition, we observed that the higher M_n PS systems show lower %SCF_3-functionalization (**Table S5**) because there is worse solubility between the PS chains and the solvent molecules during the photoreaction, causing the PS to coil up when forming the collision complex.[34,35] This is true for our solvent system (MeCN:1,2-DCE), which is relatively polar making it less soluble for higher M_n PS systems.[36] The lower %SCF_3-functionalization explains the reduced improvements for the higher M_n PS samples (PS-40K-SCF_3 and PS-110K-SCF_3) compared to the lower M_n samples.

Fig. S24. ^{1}H NMR of PS-1.12K in $CDCl_3$.

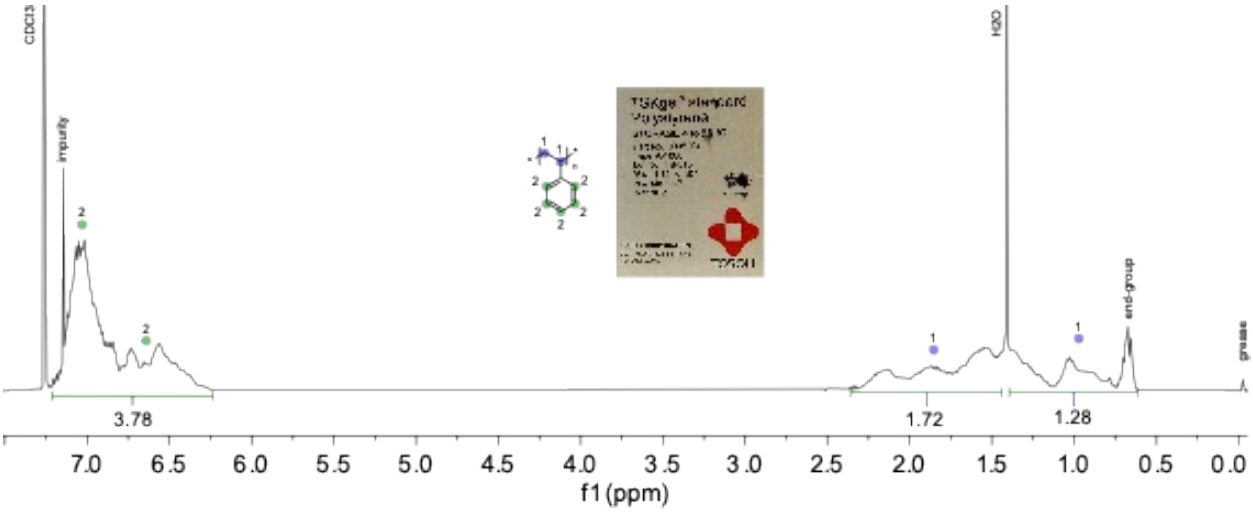

^{1}H NMR (400 MHz, $CDCl_3$) δ 7.12 – 6.27 (broad m), 2.42 – 1.48 (broad m), 1.31 – 0.60 (broad m). Note: Integrations are hard to decipher because end-group of polymer is no longer negligible and interferes with alkyl backbone peaks.

Fig. S25. ^{1}H NMR of PS-1.12K-SCF_3 (1.7mol%) with 4,4-DFBP internal standard in $CDCl_3$. (Entry 39)

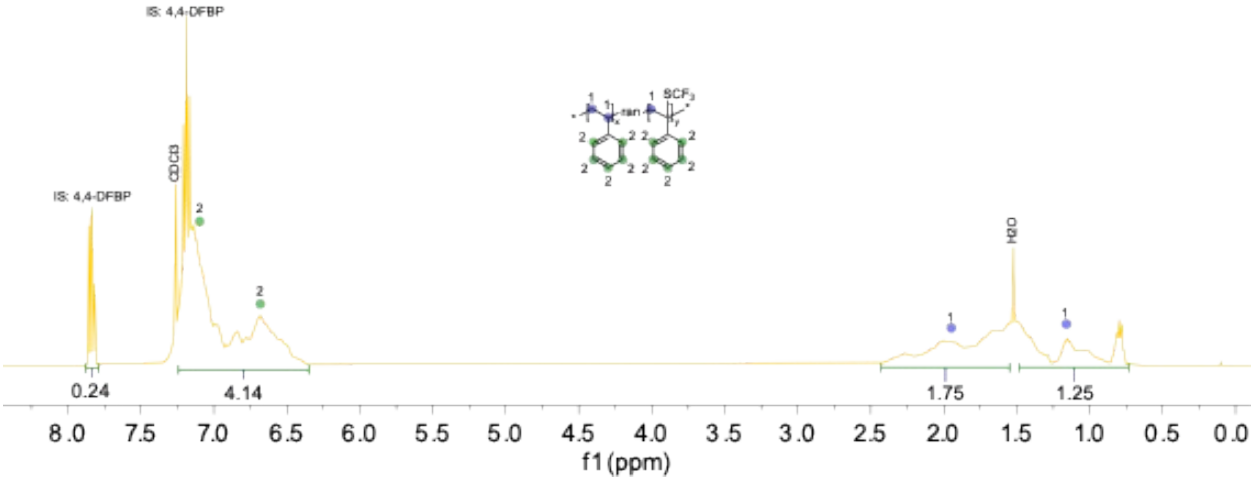

^{1}H NMR (400 MHz, $CDCl_3$) δ 7.84 (dd, *J* = 8.9, 5.4 Hz, 1H), 7.19 (t, *J* = 8.6 Hz, 1H), 7.14 (broad m, 3H), 6.68 (broad m, 2H), 2.00 (broad m), 1.15 (broad m), 0.84 – 0.70 (broad m).

Fig. S26. ^{19}F NMR of PS-1.12K-SCF_3 (1.7mol%) with 4,4-DFBP internal standard in $CDCl_3$. (Entry 39)

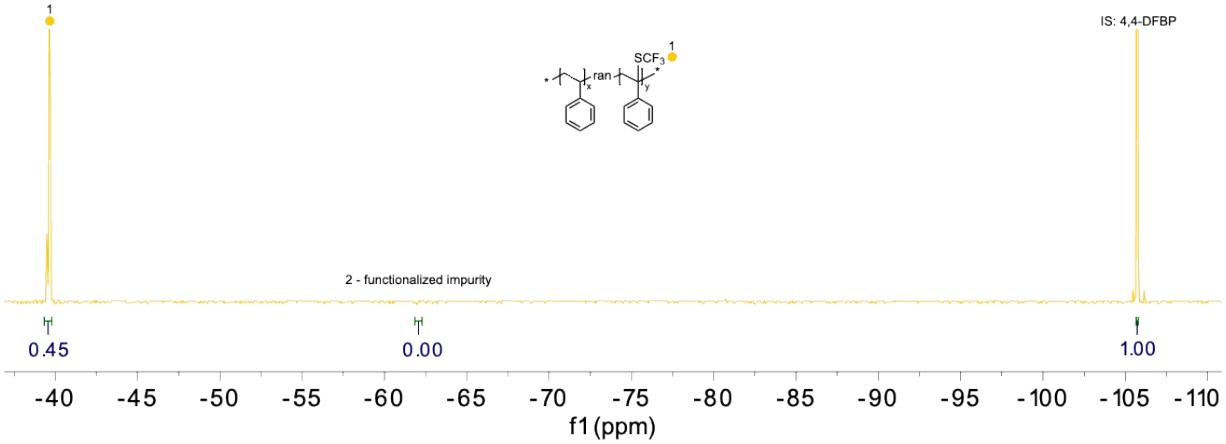

^{19}F NMR (376 MHz, $CDCl_3$) δ -39.33 – -40.01 (broad m), -62.26, -105.72 (s).

Fig. S27. ^{1}H NMR of PS-10K in $CDCl_3$.

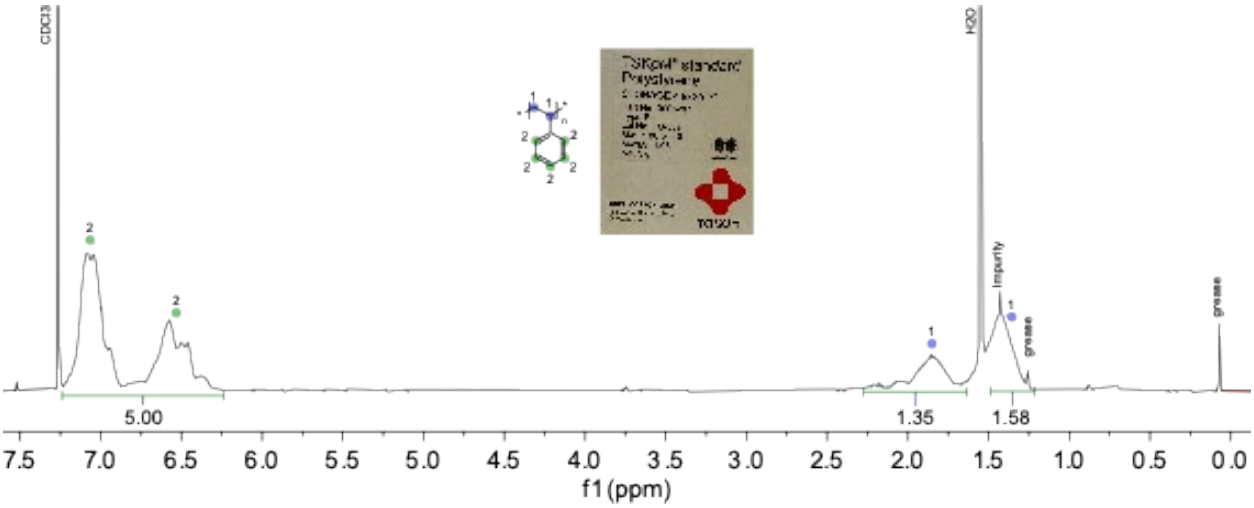

^{1}H NMR (400 MHz, $CDCl_3$) δ 7.23 – 6.28 (broad m, 5H), 2.40 – 1.60 (broad m, 1H), 1.50 – 1.34 (broad m, 2H).

Fig. S28. ^{1}H NMR of PS-10K-SCF_3 with 4,4-DFBP internal standard in $CDCl_3$.

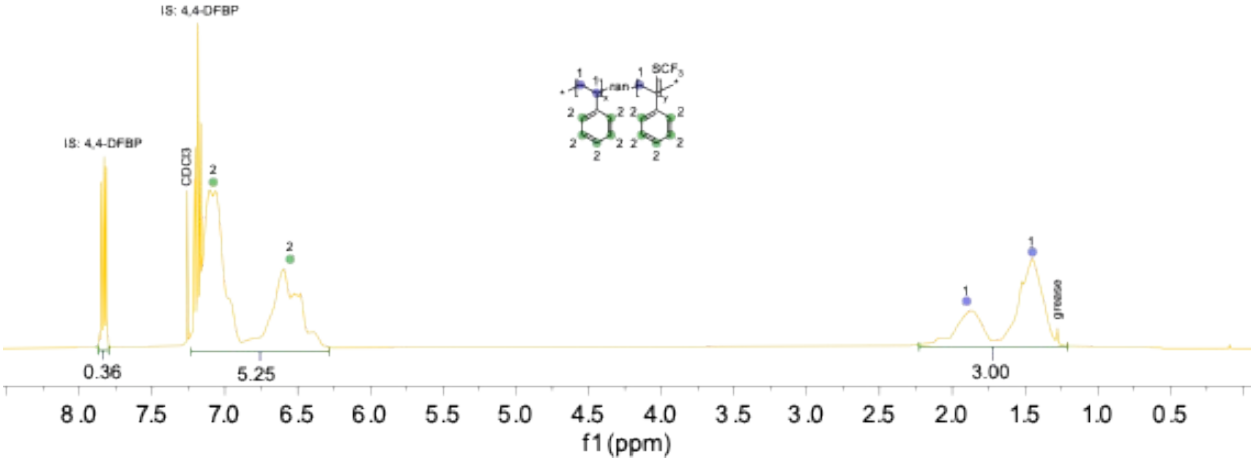

^{1}H NMR (400 MHz, $CDCl_3$) δ 7.83 (dd, *J* = 8.9, 5.4 Hz, 1H), 7.19 (t, *J* = 8.6 Hz, 1H), 7.10 (broad m, 3H), 6.60 (broad m, 2H), 1.87 (broad m, 1H), 1.45 (broad m, 2H).

Fig. S29. ^{19}F NMR of PS-10K-SCF_3 with 4,4-DFBP internal standard in $CDCl_3$.

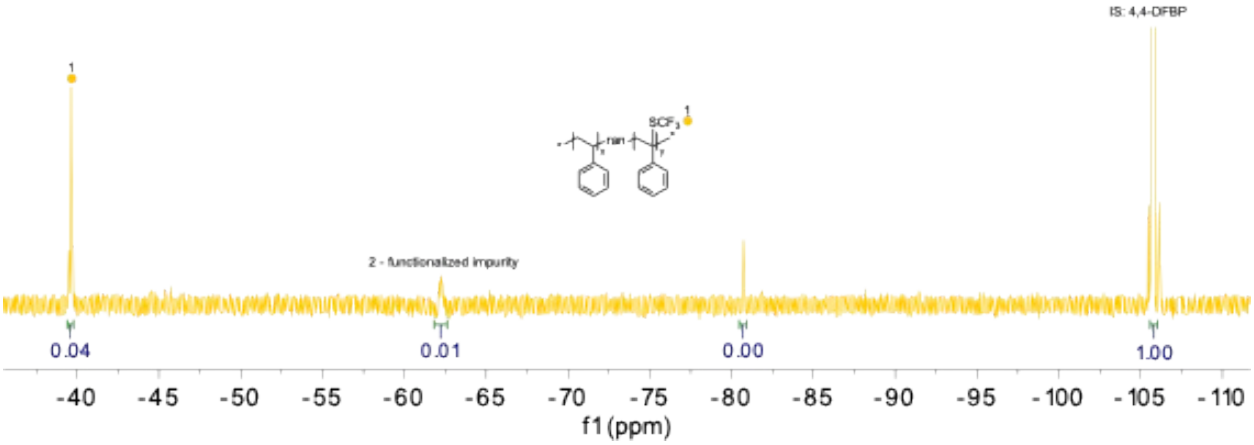

^{19}F NMR (376 MHz, $CDCl_3$) δ -39.64 (broad m), -62.21 (broad m), -80.73 (m), -105.73 (s).

Fig. S30. ^{1}H NMR of PS-19.6K in $CDCl_3$.

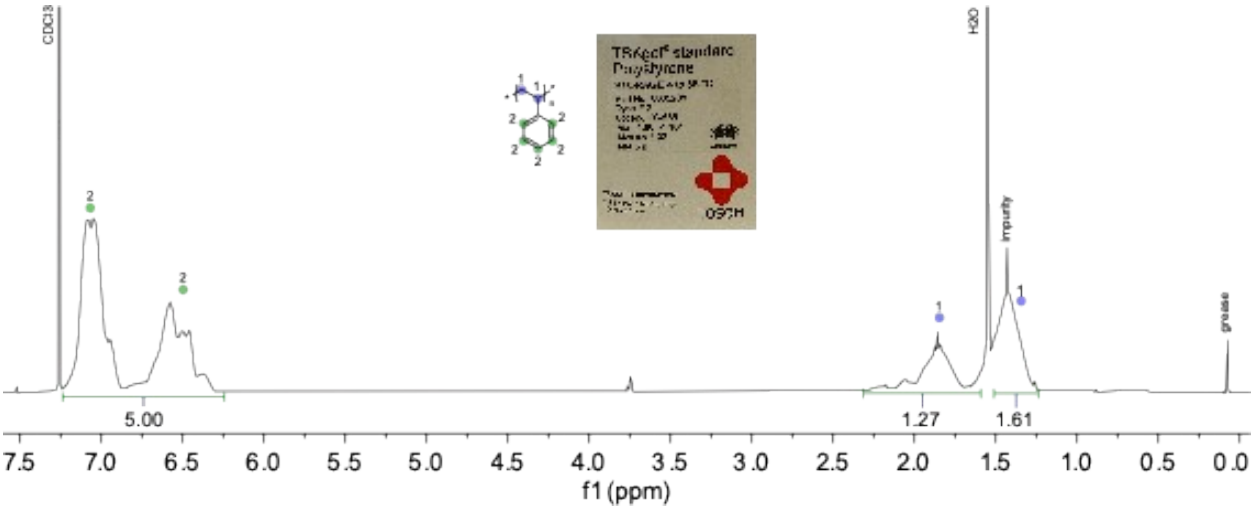

^{1}H NMR (400 MHz, $CDCl_3$) δ 7.23 – 6.30 (broad m, 5H), 2.35 – 1.60 (broad m, 1H), 1.50 – 1.26 (broad m, 2H).

Fig. S31. ^{1}H NMR of PS-19.6K-SCF_3 with 4,4-DFBP internal standard in $CDCl_3$.

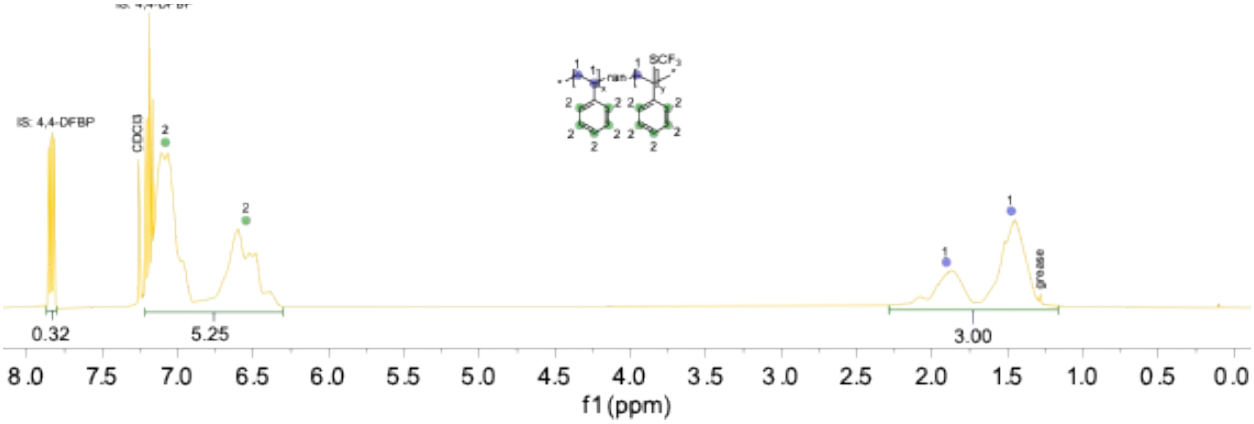

^{1}H NMR (400 MHz, $CDCl_3$) δ 7.83 (dd, *J* = 8.9, 5.4 Hz, 1H), 7.19 (t, *J* = 8.6 Hz, 1H), 7.10 (broad m, 3H), 6.60 (broad m, 2H), 1.87 (broad m, 1H), 1.45 (broad m, 2H).

Fig. S32. ^{19}F NMR of PS-19.6K-SCF_3 with 4,4-DFBP internal standard in $CDCl_3$.

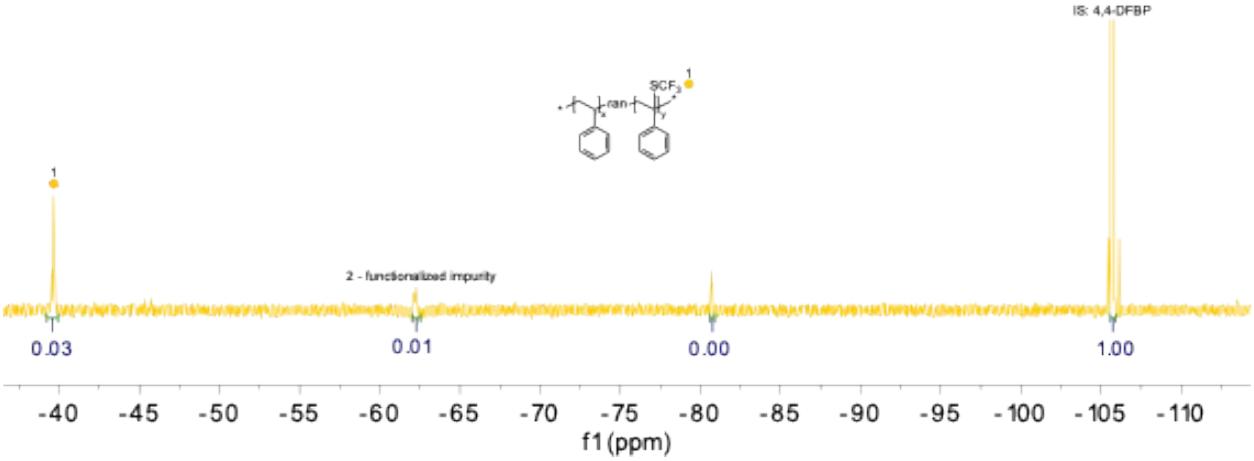

^{19}F NMR (376 MHz, $CDCl_3$) δ -39.64 (broad m), -62.21 (broad m), -80.73 (m), -105.73 (s).

Fig. S33. ^{1}H NMR of PS-40.4K in $CDCl_3$.

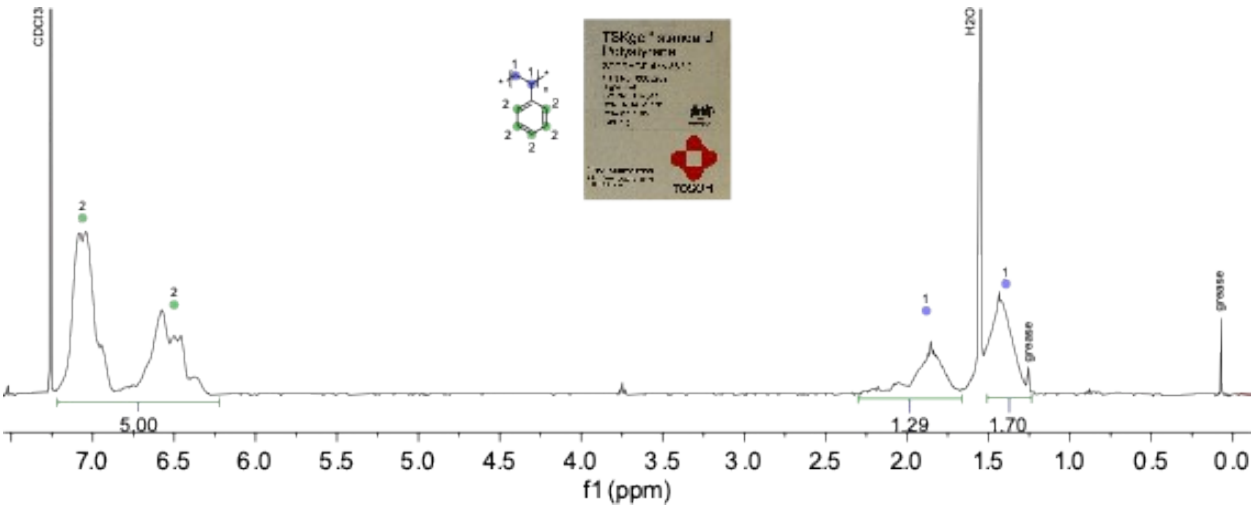

^{1}H NMR (400 MHz, $CDCl_3$) δ 7.23 – 6.28 (broad m, 5H), 2.35 – 1.60 (broad m, 1H), 1.50 – 1.27 (broad m, 2H).

Fig. S34. ^{1}H NMR of PS-40.4K-SCF_3 with 4,4-DFBP internal standard in $CDCl_3$.

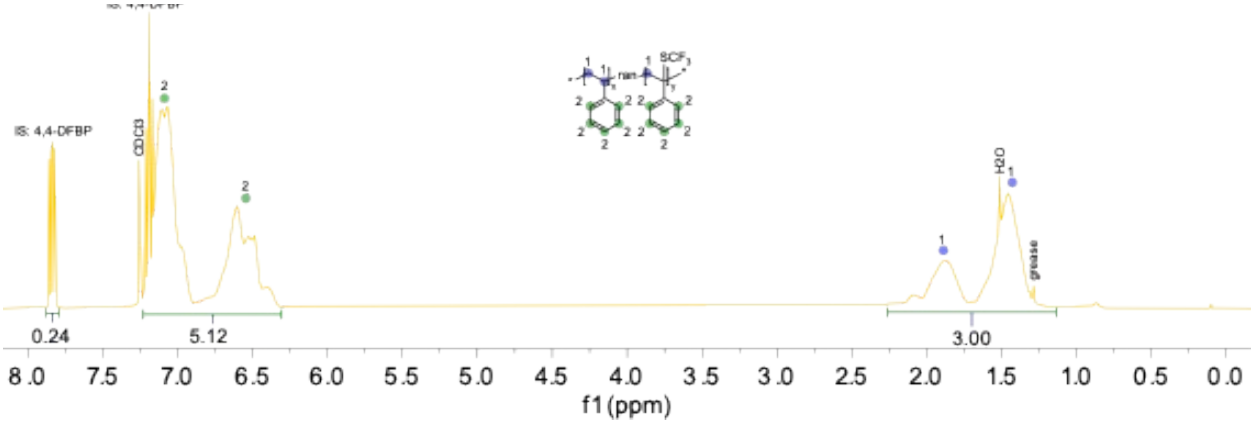

^{1}H NMR (400 MHz, $CDCl_3$) δ 7.83 (dd, *J* = 8.9, 5.4 Hz, 1H), 7.19 (t, *J* = 8.6 Hz, 1H), 7.10 (broad m, 3H), 6.60 (broad m, 2H), 1.87 (broad m, 1H), 1.45 (broad m, 2H).

Fig. S35. ^{19}F NMR of PS-40.4-SCF_3 with 4,4-DFBP internal standard in $CDCl_3$.

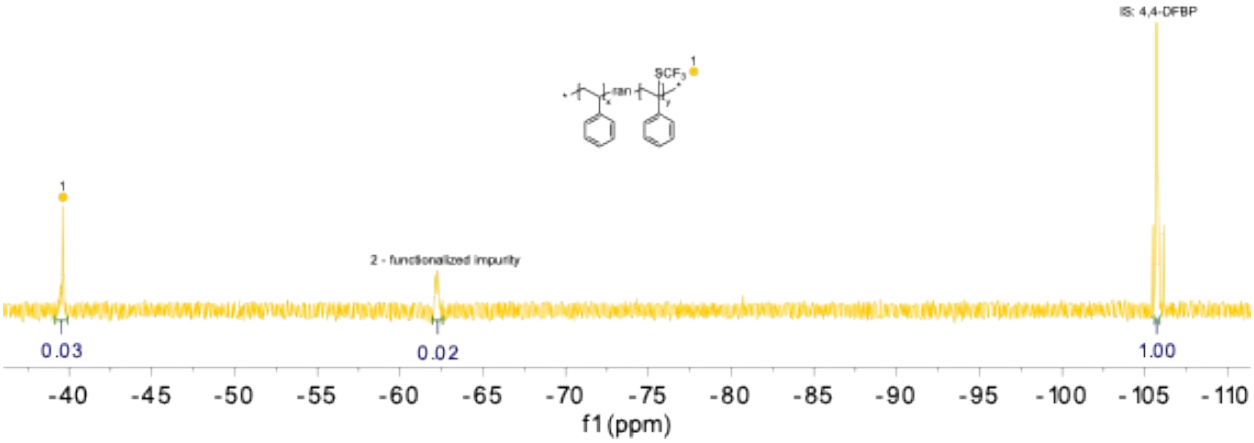

^{19}F NMR (376 MHz, $CDCl_3$) δ -39.64 (broad m), -62.21 (broad m), -105.73 (s).

Fig. S36. ^{1}H NMR of PS-110K in $CDCl_3$.

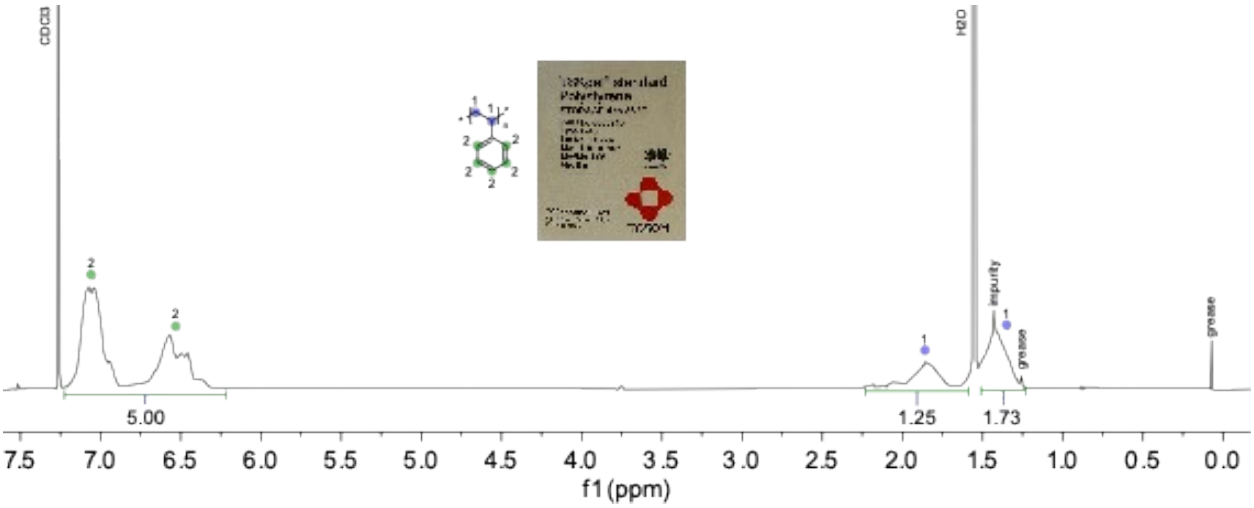

^{1}H NMR (400 MHz, $CDCl_3$) δ 7.20 – 6.25 (broad m, 5H), 2.22 – 1.60 (broad m, 1H), 1.51 – 1.21 (broad m, 2H).

Fig. S37. ^{1}H NMR of PS-110K-SCF_3 with 4,4-DFBP internal standard in $CDCl_3$.

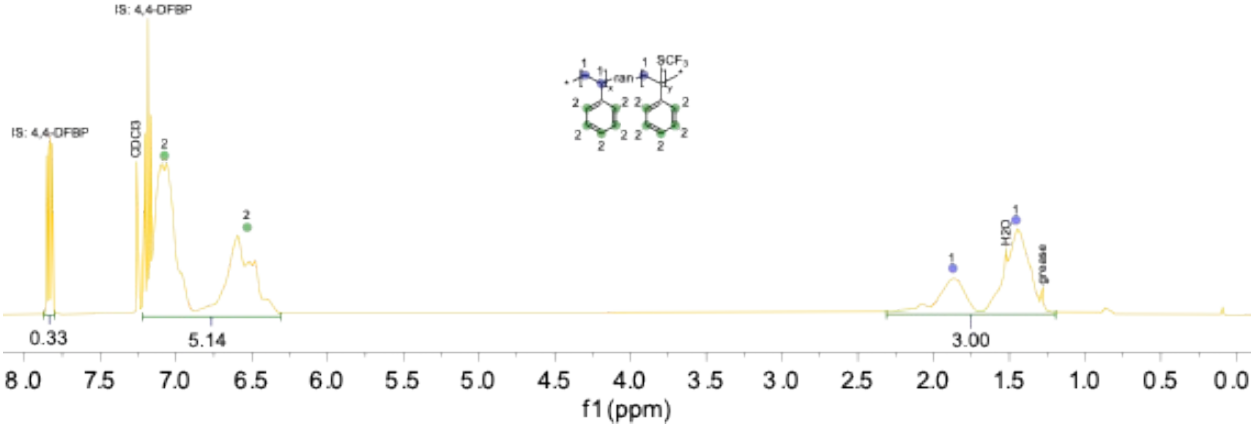

^{1}H NMR (400 MHz, $CDCl_3$) δ 7.83 (dd, *J* = 8.9, 5.4 Hz, 1H), 7.19 (t, *J* = 8.6 Hz, 1H), 7.10 (broad m, 3H), 6.60 (broad m, 2H), 1.87 (broad m, 1H), 1.45 (broad m, 2H).

Fig. S38. ^{19}F NMR of PS-110K-SCF_3 with 4,4-DFBP internal standard in $CDCl_3$.

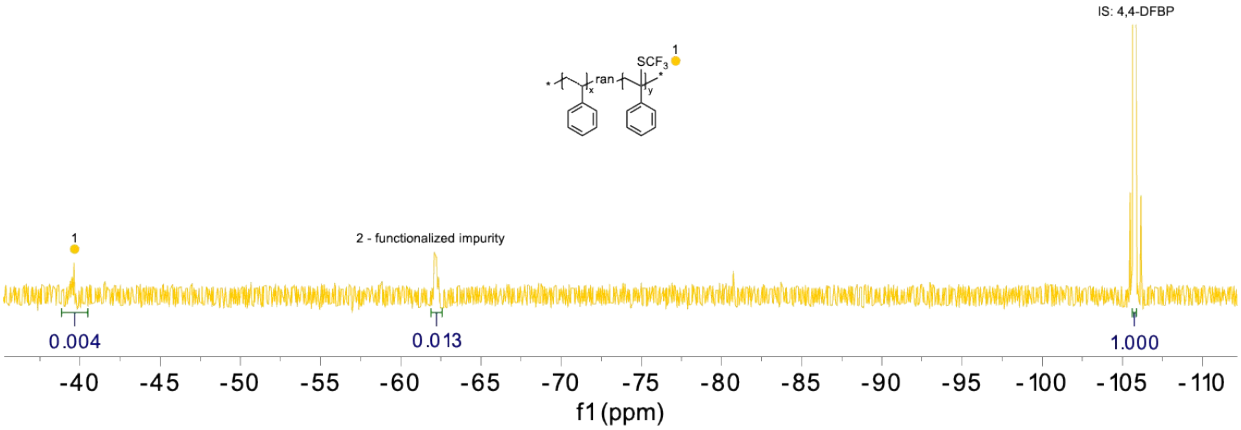

^{19}F NMR (376 MHz, $CDCl_3$) δ -39.64 (broad m), -62.21 (broad m), -105.73 (s).

Fig. S39. GPC of PS-1.12K and PS-1.12K-SCF_3. (Entry 39)

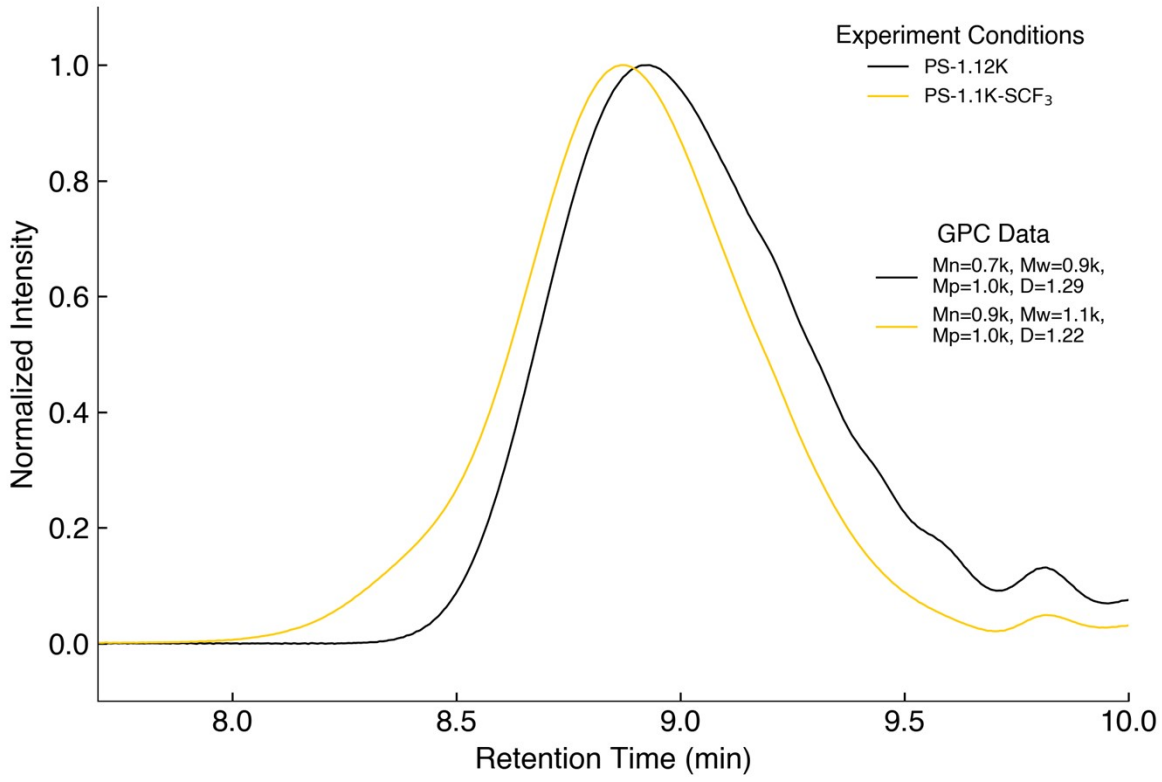

Fig. S40. GPC of PS-10K and PS-10K-SCF_3.

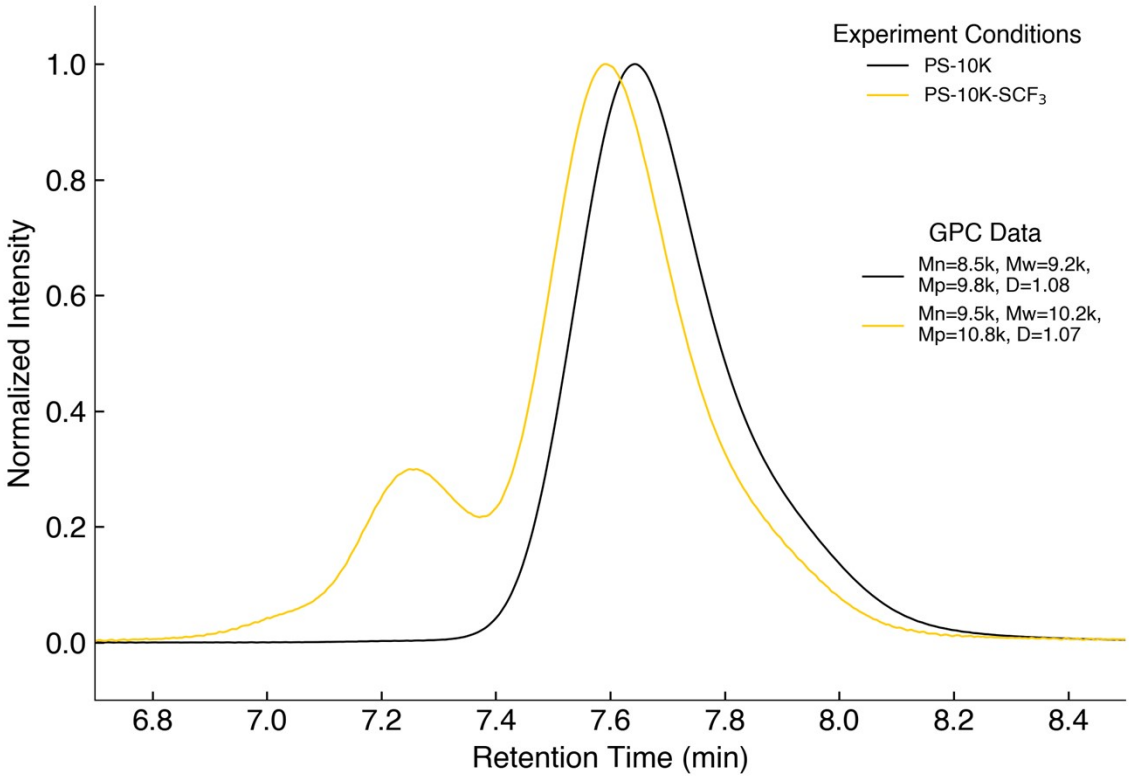

Fig. S41. GPC of PS-19.6K and PS-19.6K-SCF_3.

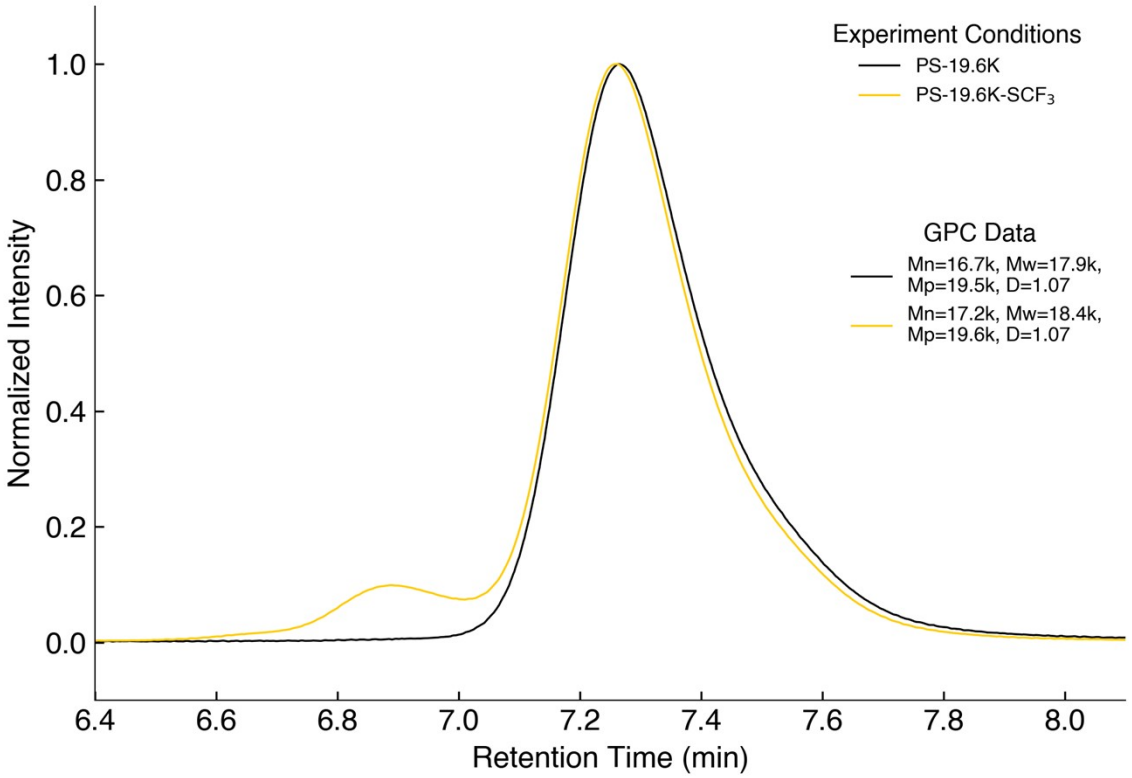

Fig. S42. GPC of PS-40.4K and PS-40.4K-SCF_3.

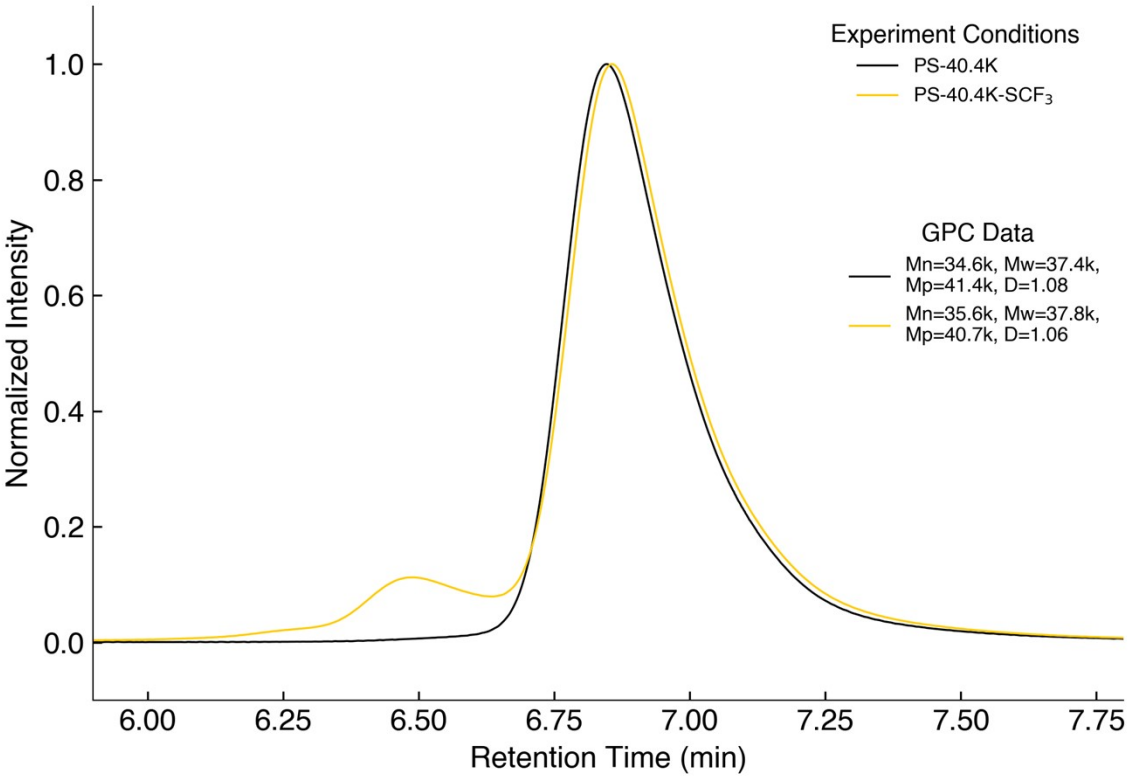

Fig. S43. GPC of PS-110K and PS-110K-SCF_3.

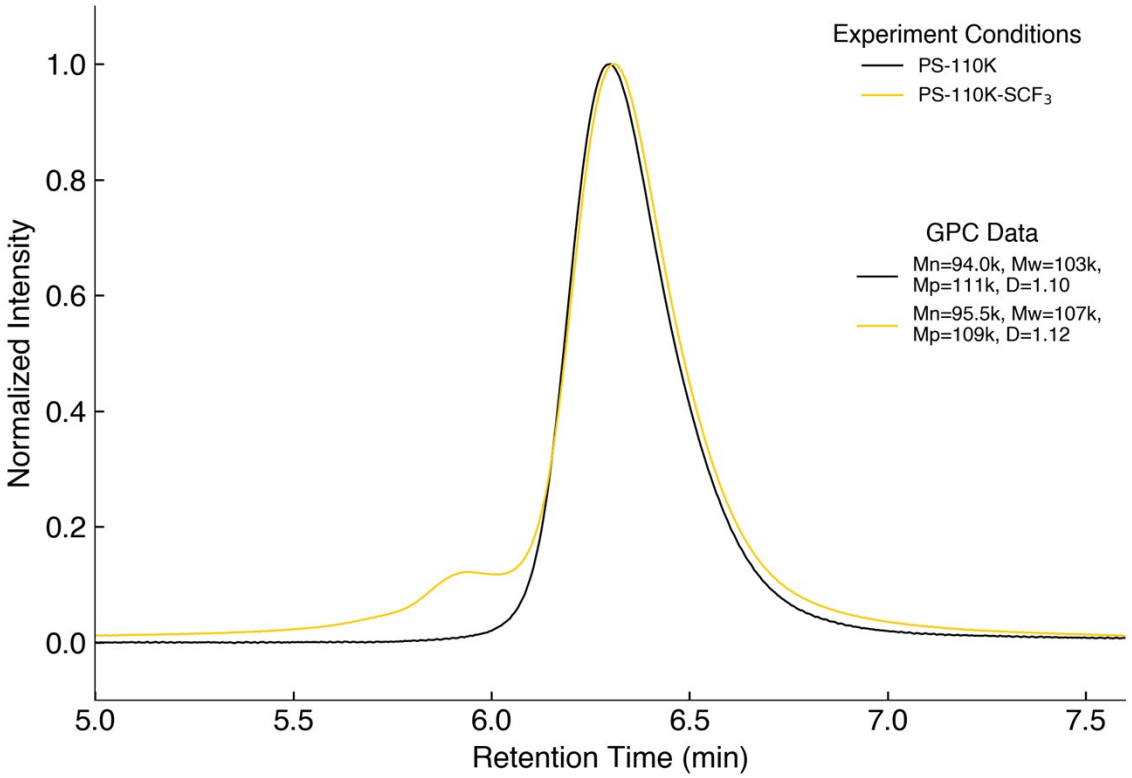

Fig. S44. Stacked MALDI of PS-1.12K and PS-1.12K-SCF_3.

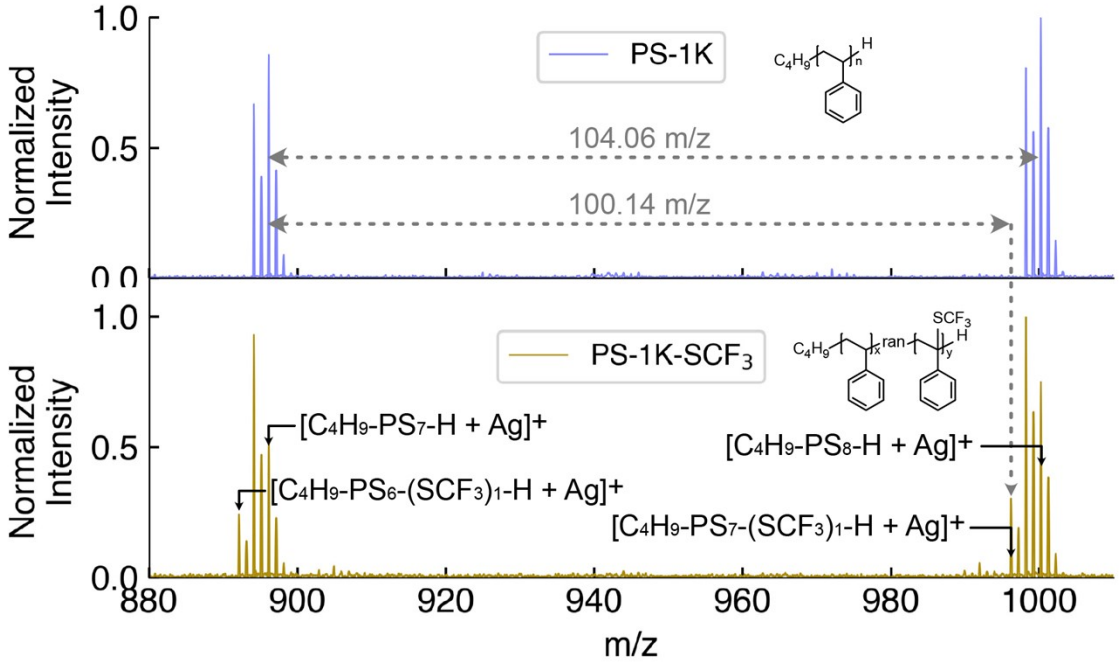

Fig. S45. Isothermal TGA at 300°C of PS-1.12K and PS-1.12K-SCF_3 (1.70mol%). (Table S6, Entry 1)

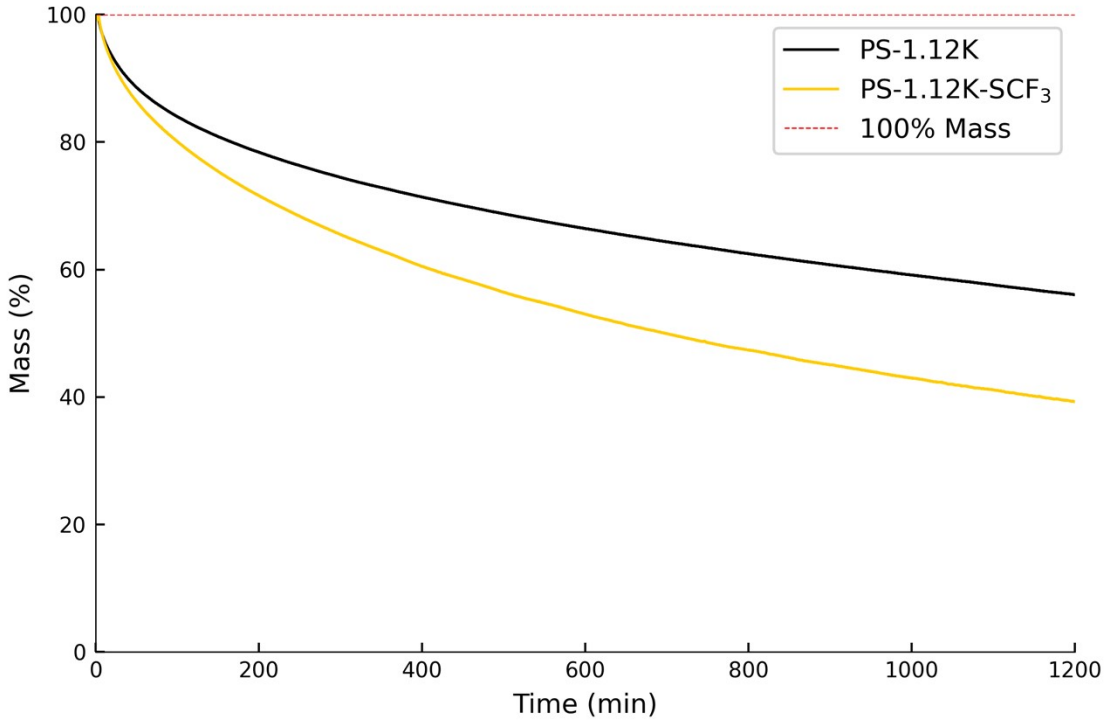

Fig. S46. Dynamic TGA of PS-1.12K and PS-1.12K-SCF_3 (1.70mol%). (Table S6, Entry 1)

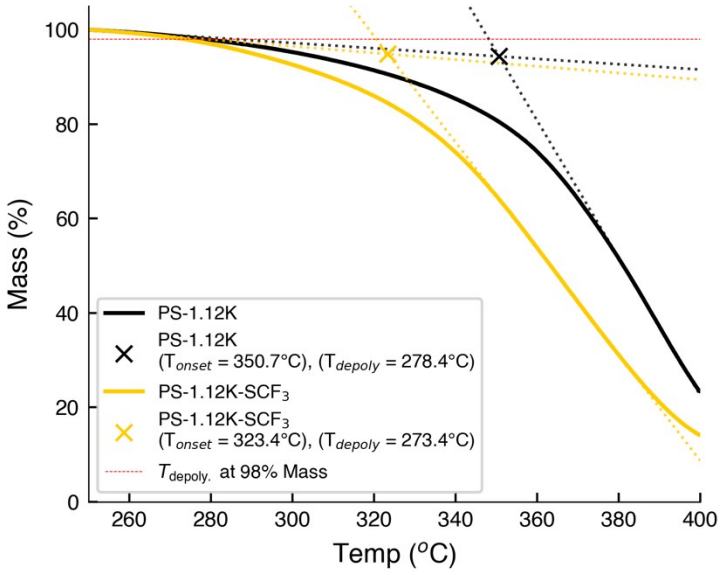

Fig. S47. Isothermal TGA at 300°C of PS-10K and PS-10K-SCF_3.

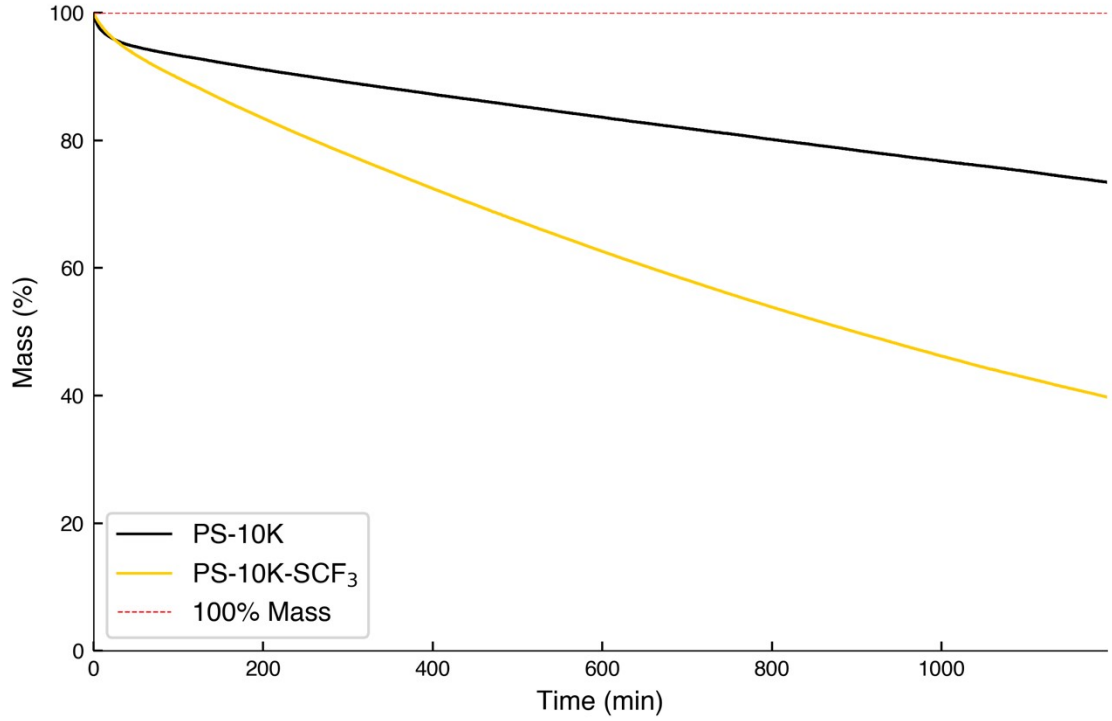

Fig. S48. Dynamic TGA of PS-10K and PS-10K-SCF_3.

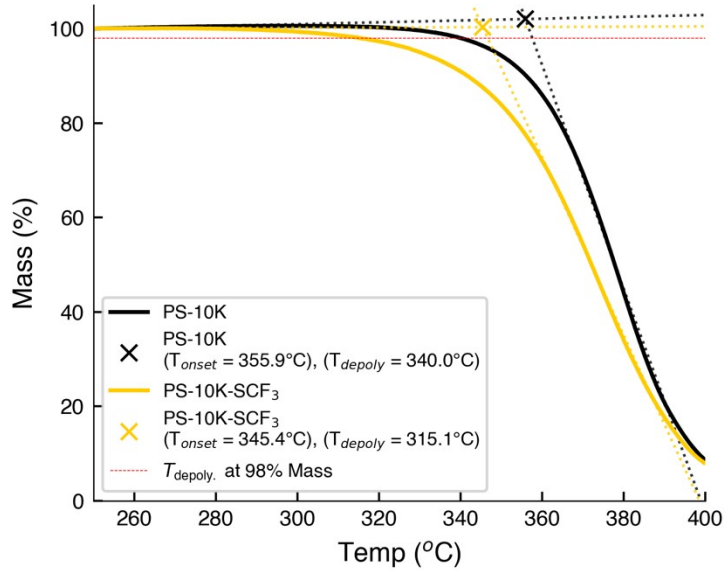

Fig. S49. Isothermal TGA at 300°C of PS-19.6K and PS-19.6K-SCF_3.

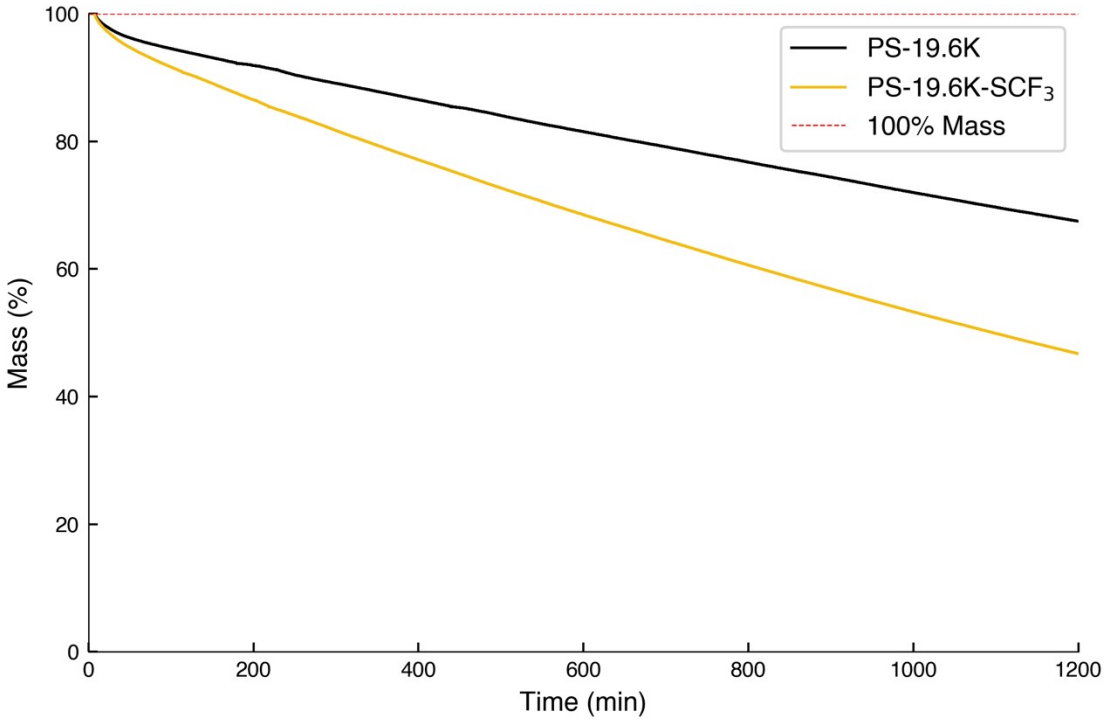

Fig. S50. Dynamic TGA of PS-19.6K and PS-19.6K-SCF_3.

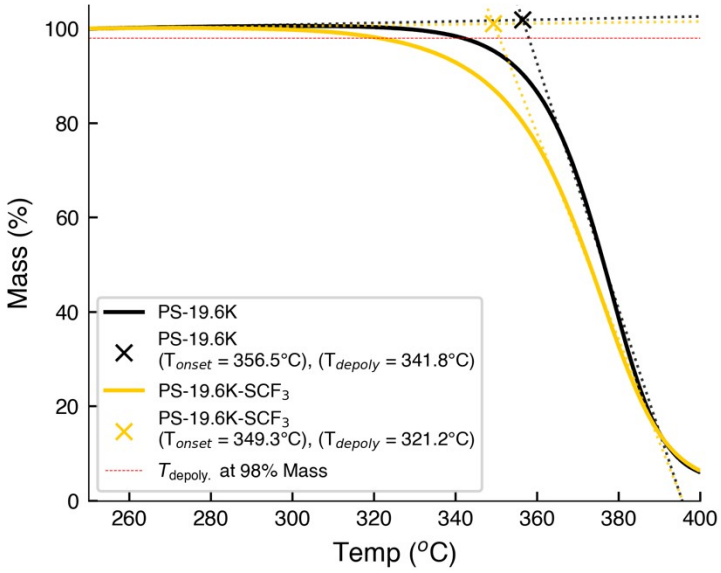

Fig. S51. Isothermal TGA at 300°C of PS-40.4K and PS-40.4K-SCF_3.

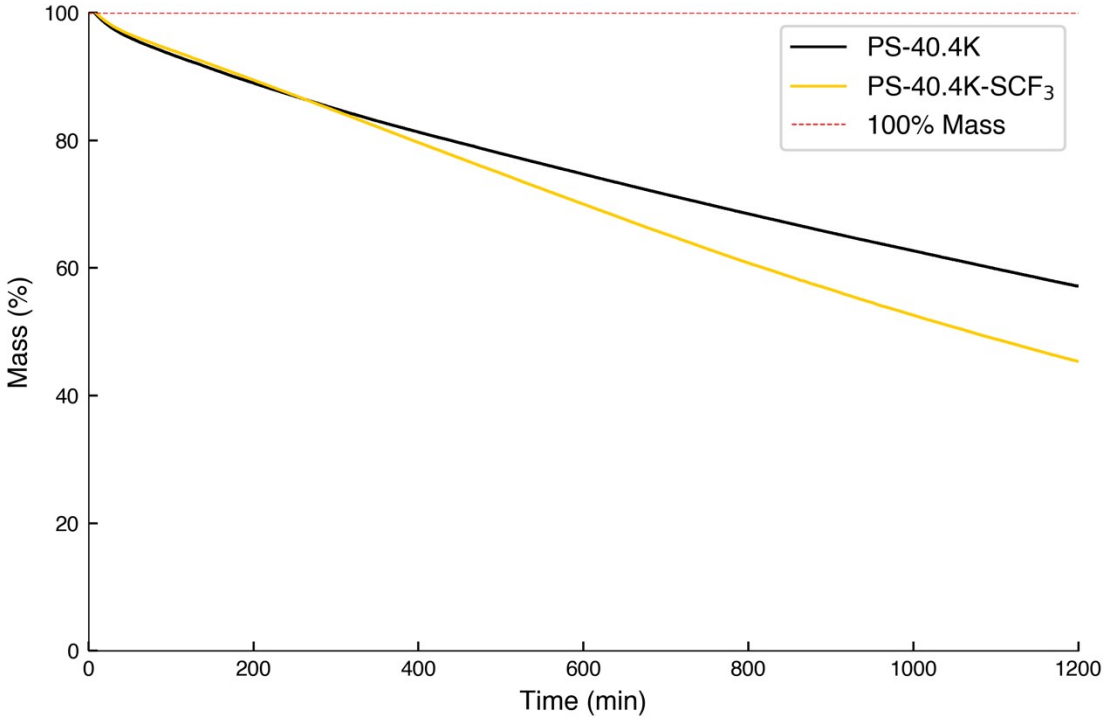

Fig. S52. Dynamic TGA of PS-40.4K and PS-40.4K-SCF_3.

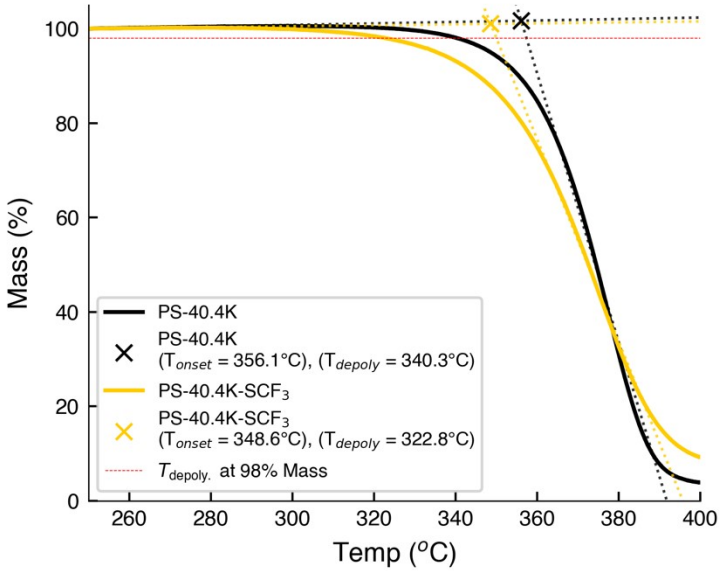

Fig. S53. Isothermal TGA at 300°C of PS-110K and PS-110K-SCF_3.

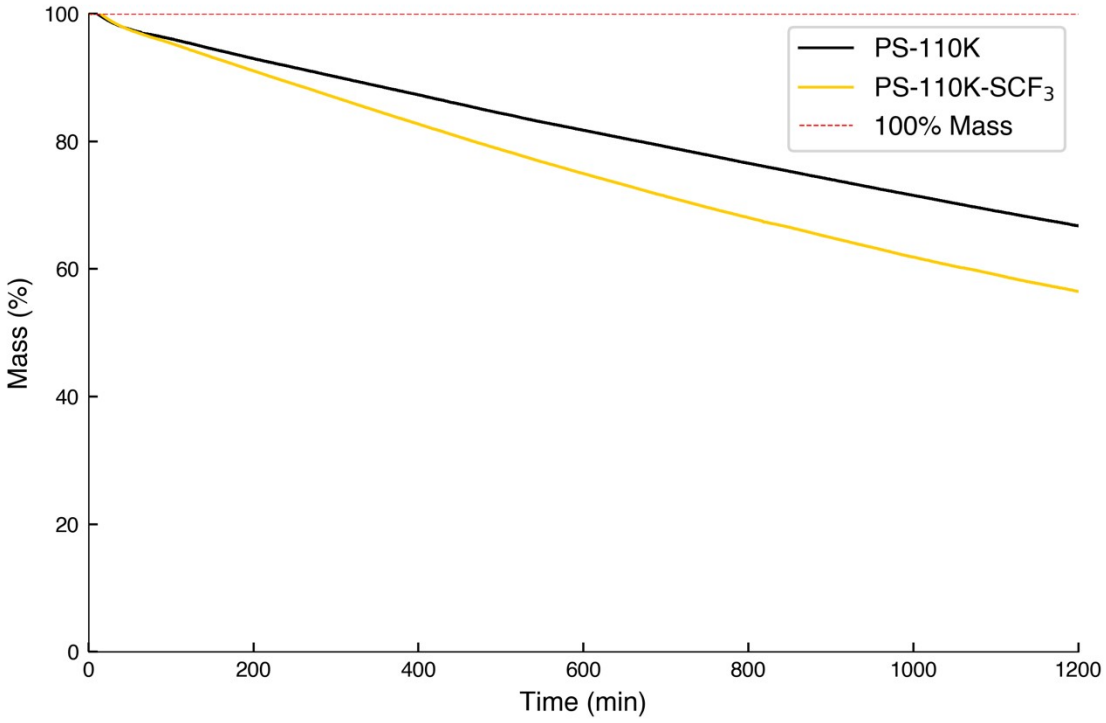

Fig. S54. Dynamic TGA of PS-110K and PS-110K-SCF_3.

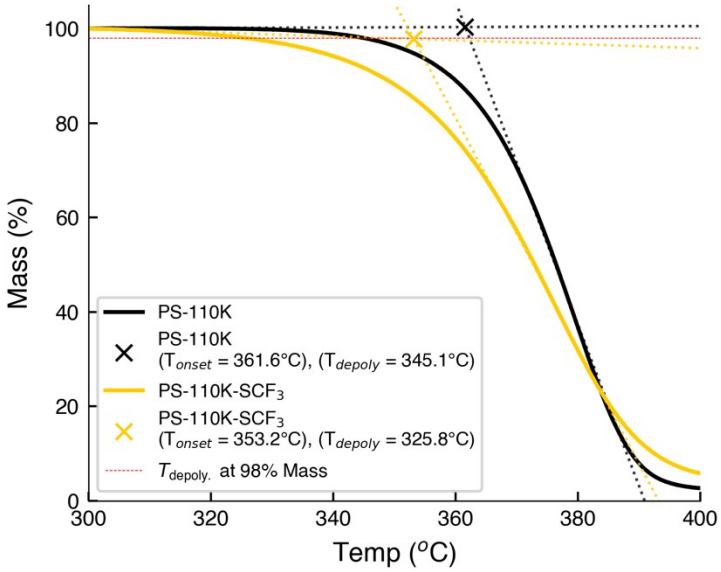

Study of %-SCF_3 Functionalization on Polystyrene.

The following samples were synthesized using the General Methods and PS (M_w=1.12kg/mol).

Table S6. Reaction conditions and results from the %SCF_3-functionalization study.

Entry	PS-1.12K (eq. by monomer)	4CzIPN (eq.)	Phth-SCF_3 (eq.)	K_2CO_3 (eq.)	Reaction Time (hrs)	MeCN (mL)	1,2-DCE (mL)	% Yield by mass	SCF_3-Functionalization (mol %)	^{19}F-NMR (I_{-40ppm} : I_{-60ppm})*
1	2	0.04	0.1	1	16	5	5	90.1	1.7	1:0.02
2	2	0.04	0.5	1	16	5	5	75.1	1.6	1:0.18
3	2	0.04	1	1	16	5	5	45.7	1.9	1:0.29
4	2	0.04	2	1	16	5	5	79.3	2.8	1:0.28
5	2	0.2	2	1	16	5	5	78.8	2.9	1:0.33

*Ratio between the integration of the product peak (PS-SCF_3, -40ppm), and the impurity peak (-60ppm).

Fig. S55. ^{1}H NMR of PS-1.12K-SCF_3 (1.6mol%) with 4,4-DFBP internal standard in $CDCl_3$. (Table S6, Entry 2)

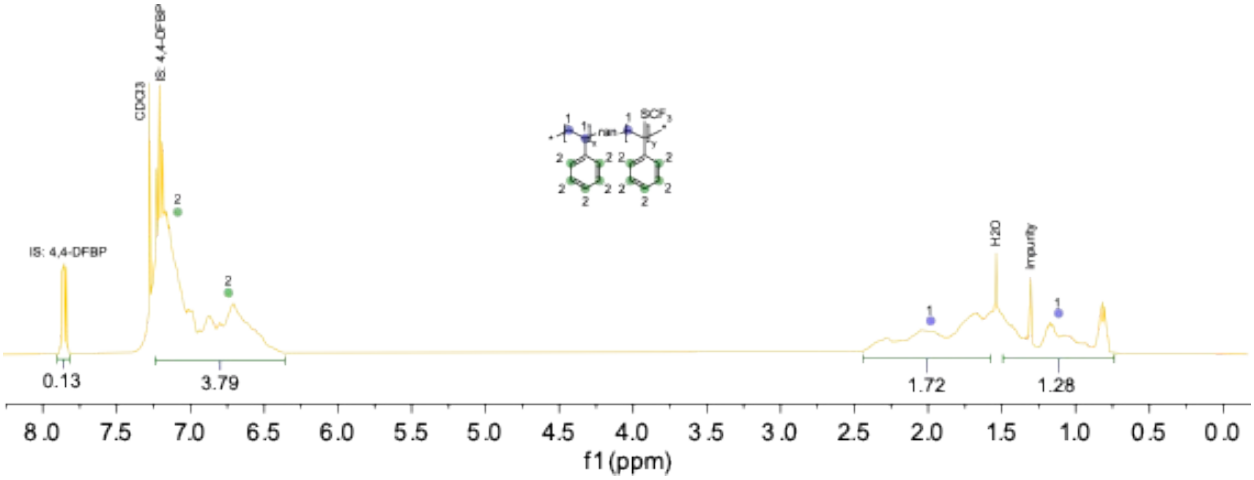

^{1}H NMR (400 MHz, $CDCl_3$) δ 7.84 (dd, *J* = 8.9, 5.4 Hz, 1H), 7.19 (t, *J* = 8.6 Hz, 1H), 7.14 – 6.35 (broad m), 2.40 – 1.60 (broad m), 1.50 – 0.70 (broad m).

Fig. S56.[19]F NMR of PS-1.12K-SCF_3 (1.6mol%) with 4,4-DFBP internal standard in $CDCl_3$. (Table S6, Entry 2)

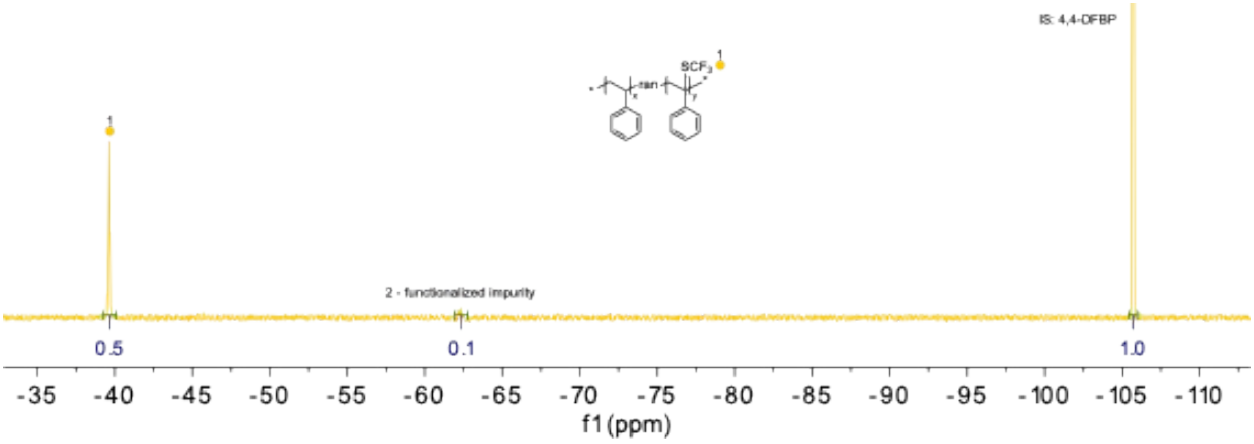

[19]F NMR (377 MHz, $CDCl_3$) δ -39.14 – -40.61 (broad m), -62.32 (broad m), -105.71 (s).

Fig. S57.[1]H NMR of PS-1.12K-SCF_3 (1.9mol%) with 4,4-DFBP internal standard in $CDCl_3$. (Table S6, Entry 3)

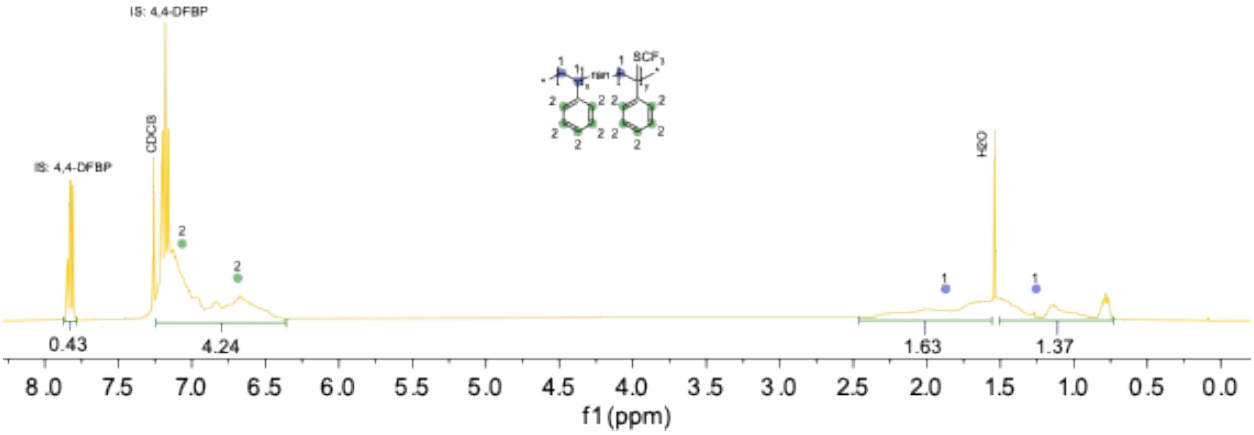

[1]H NMR (400 MHz, $CDCl_3$) δ 7.84 (dd, *J* = 8.9, 5.4 Hz, 1H), 7.19 (t, *J* = 8.6 Hz, 1H), 7.14 – 6.35 (broad m), 2.40 – 1.60 (broad m), 1.50 – 0.70 (broad m).

Fig. S58.[19]F NMR of PS-1.12K-SCF_3 (1.9mol%) with 4,4-DFBP internal standard in $CDCl_3$. (Table S6, Entry 3)

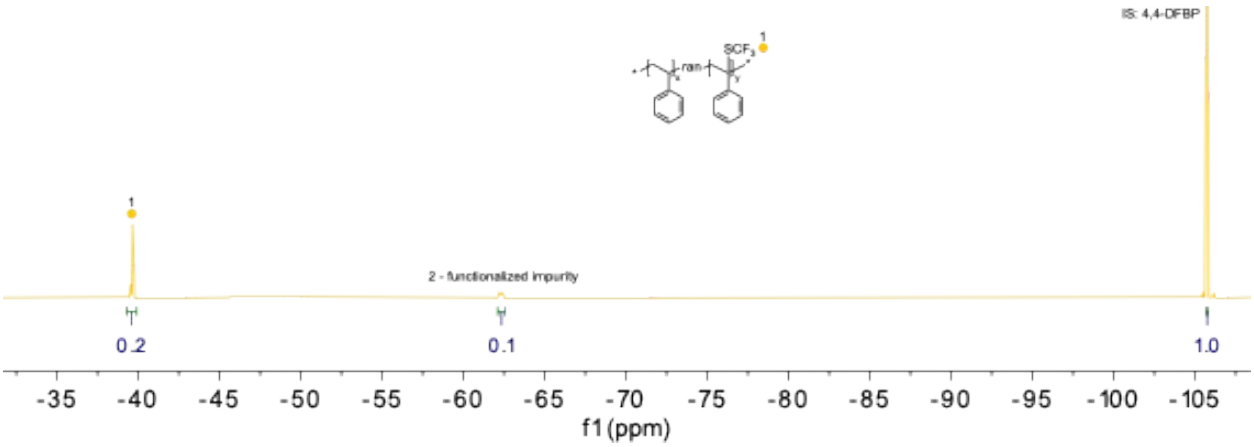

[19]F NMR (377 MHz, $CDCl_3$) δ -39.14 – -40.61 (broad m), -62.32 (broad m), -105.71 (s).

Fig. S59. [1]H NMR of PS-1.12K-SCF_3 (2.8mol%) with 4,4-DFBP internal standard in $CDCl_3$. (Table S6, Entry 4)

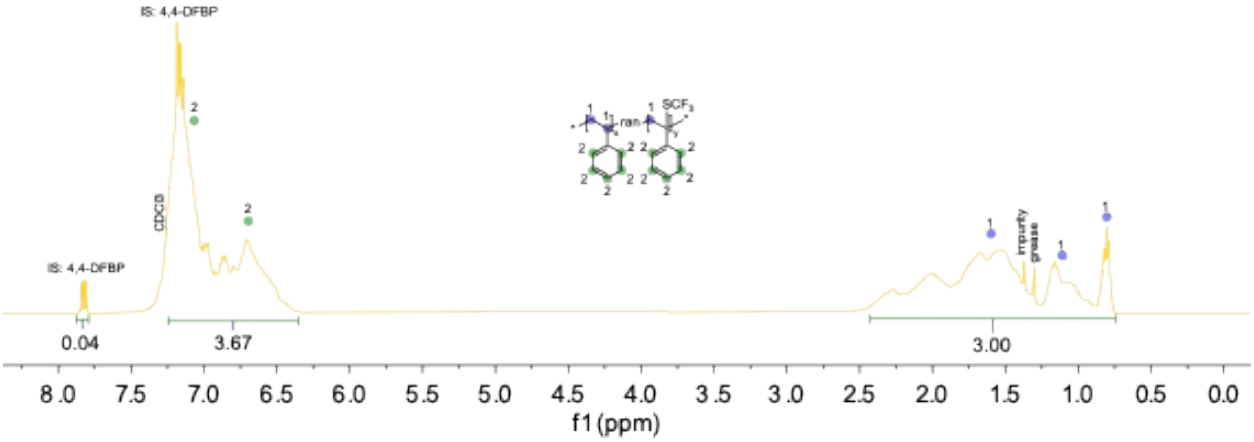

[1]H NMR (400 MHz, $CDCl_3$) δ 7.84 (dd, *J* = 8.9, 5.4 Hz, 1H), 7.19 (t, *J* = 8.6 Hz, 1H), 7.14 – 6.35 (broad m), 2.40 – 0.70 (broad m).

Fig. S60. ^{19}F NMR of PS-1.12K-SCF_3 (2.8mol%) with 4,4-DFBP internal standard in $CDCl_3$. (Table S6, Entry 4)

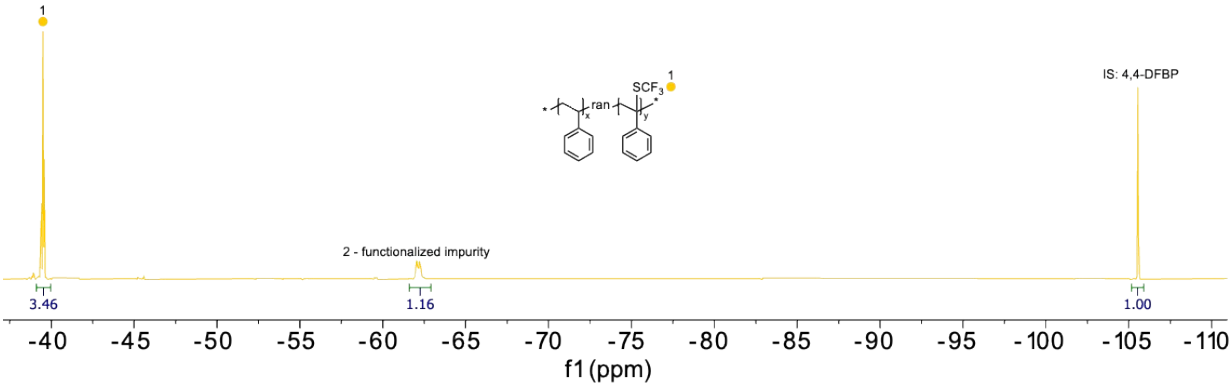

^{19}F NMR (377 MHz, $CDCl_3$) δ -39.14 – -40.61 (broad m), -62.32 (broad m), -105.71 (s).

Fig. S61.^{1}H NMR of PS-1.12K-SCF_3 (2.9mol%) with 4,4-DFBP internal standard in $CDCl_3$. (Table S6, Entry 5)

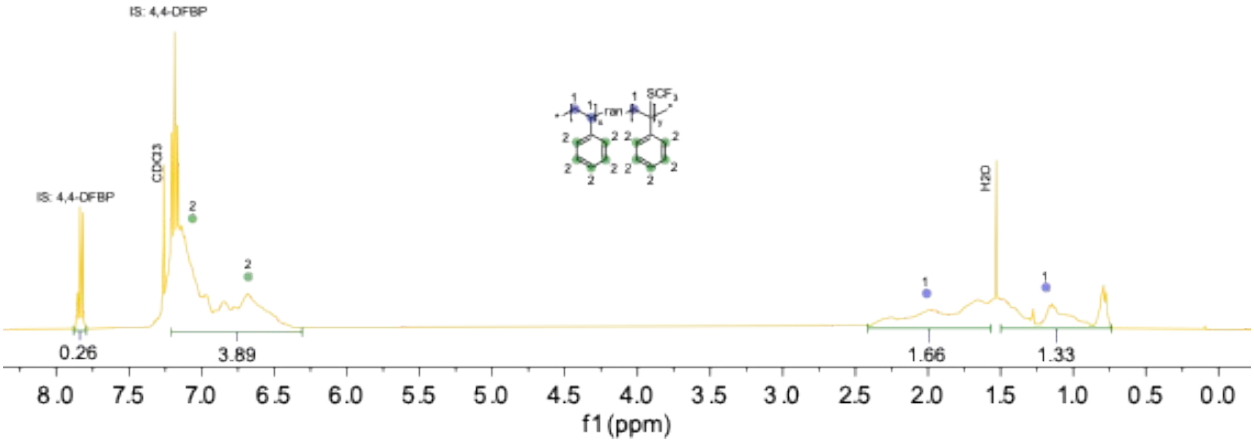

^{1}H NMR (400 MHz, $CDCl_3$) δ 7.84 (dd, *J* = 8.9, 5.4 Hz, 1H), 7.19 (t, *J* = 8.6 Hz, 1H), 7.14 (broad m), 6.68 (broad m), 2.40 – 1.60 (broad m), 1.5 – 0.70 (broad m).

Fig. S62.^{19}F NMR of PS-1.12K-SCF_3 (2.9mol%) with 4,4-DFBP internal standard in $CDCl_3$. (Table S6, Entry 5)

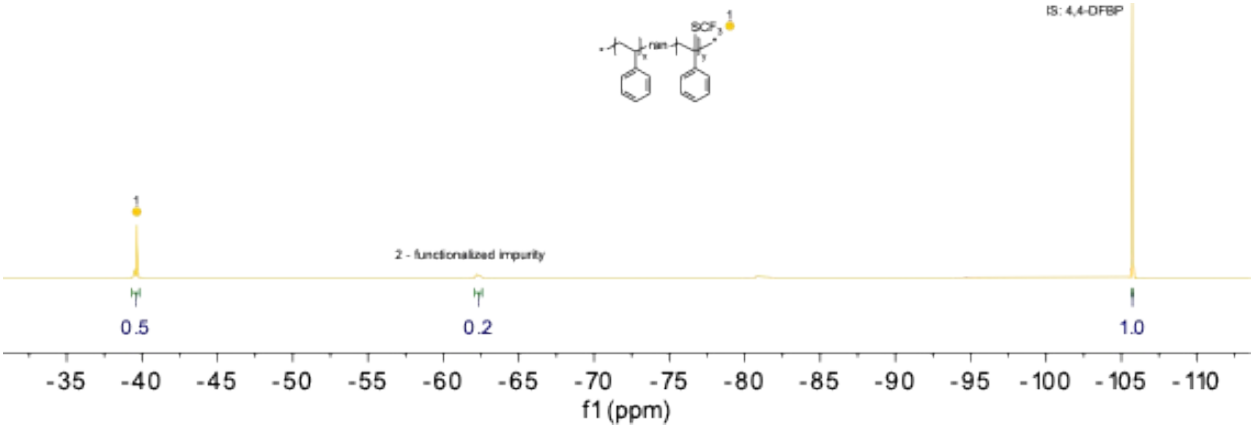

^{19}F NMR (377 MHz, $CDCl_3$) δ -39.14 – -40.61 (broad m), -62.32 (broad m), -105.71 (s).

Fig. S63. Isothermal TGA at 300°C of PS-1.12K and PS-1.12K-SCF_3 with various %SCF_3 functionalizations.

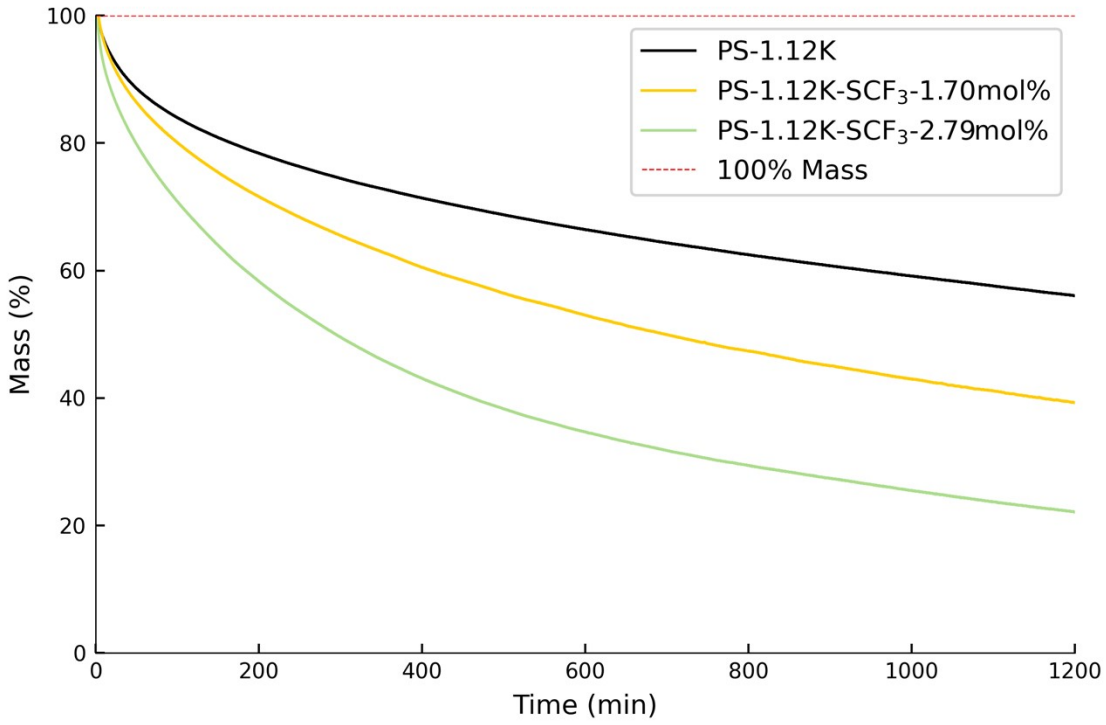

Fig. S64. Dynamic TGA of PS-1.12K and PS-1.12K-SCF_3 with various %SCF_3 functionalizations.

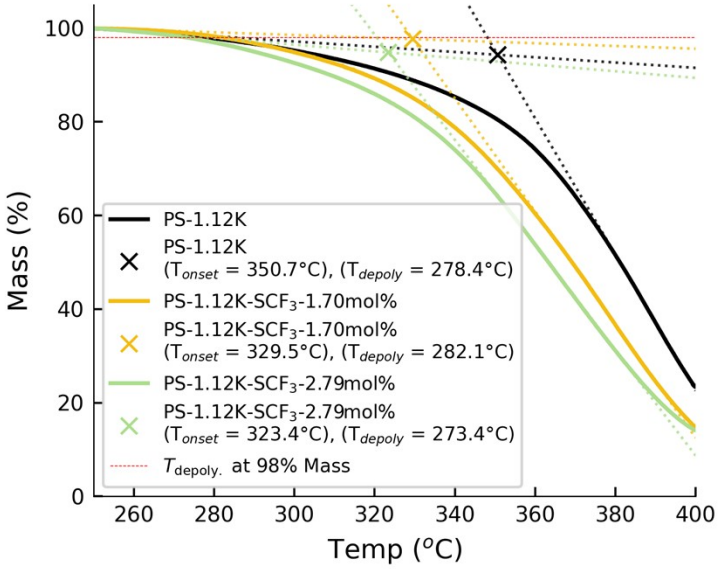

Commercial PS samples

Table S7. Summary of GPC, mol% SCF_3-functionalization, and TGA results for commercial PS samples.

Entry	Experiment ID	Yield by mass (%)	M_n of PS (kg/mol)	SCF_3 functionalization (mol %)	^{19}F-NMR (I_{-40ppm} : I_{-60ppm})*	Isothermal TGA at 300°C: % mass loss after 1200 minutes	Dynamic TGA: Onset temperature (°C)	Dynamic TGA: temperature of 98% depolymerization (°C)
1	PS-Styrofoam	n/a	65.9	n/a	n/a	35.2	355.5	328.4
2	PS-Styrofoam-SCF_3	44.5	69.2	0.14	1:0.65	46.8	356.4	274.2
3	PS-Container	n/a	128	n/a	n/a	30.0	359.6	338.8
4	PS-Container-SCF_3	85.6	164	0.15	1:0.33	40.7	356.5	329.6
5	PS-Coffee-Lid	n/a	90.5	n/a	n/a	9.0	376.8	355.0
6	PS-Coffee-Lid-SCF_3	54.7	135	0.34	1:0.2	32.1	370.8	259.8
7	PS-Petri-Dish	n/a	101	n/a	n/a	41.7	357.7	318.0
8	PS-Petri-Dish-SCF_3	33.2	105	0.29	1:0.23	45.2	357.6	323.3
9	PS-Red-Solo-Cup	n/a	108	n/a	n/a	6.1	375.9	355.8
10	PS-Red-Solo-Cup-SCF_3	66.2	114	0.08	1:1.31	34.1	363.7	273.2
11	PS-Blue-Cup	n/a	118	n/a	n/a	33.7	356.6	323.9
12	PS-Blue-Cup-SCF_3	85.2	133	0.15	1:0.27	36.3	361.1	305.6

*Ratio between the integration of the product peak (PS-SCF_3, -40ppm), and the impurity peak (-60ppm).

Fig. S65. Normalized GPC of PS-Styrofoam and PS-Styrofoam-SCF_3.

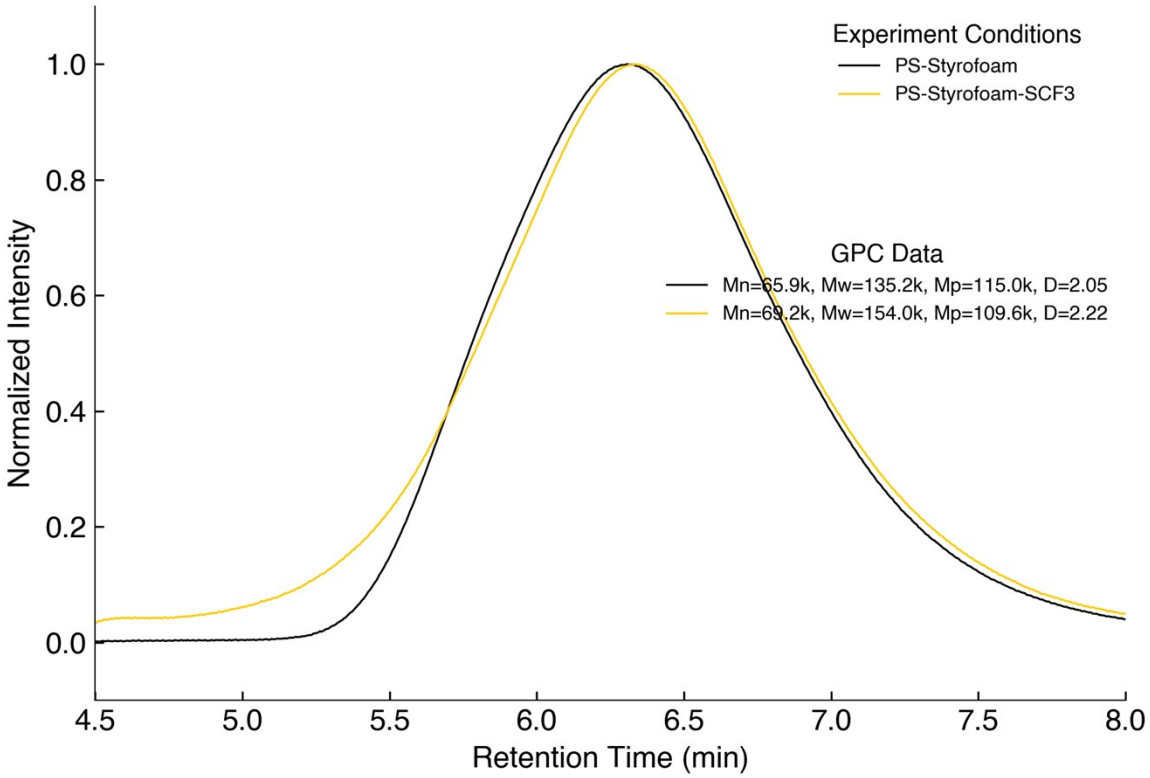

Fig. S66. Normalized GPC of PS-Container and PS-Container-SCF_3.

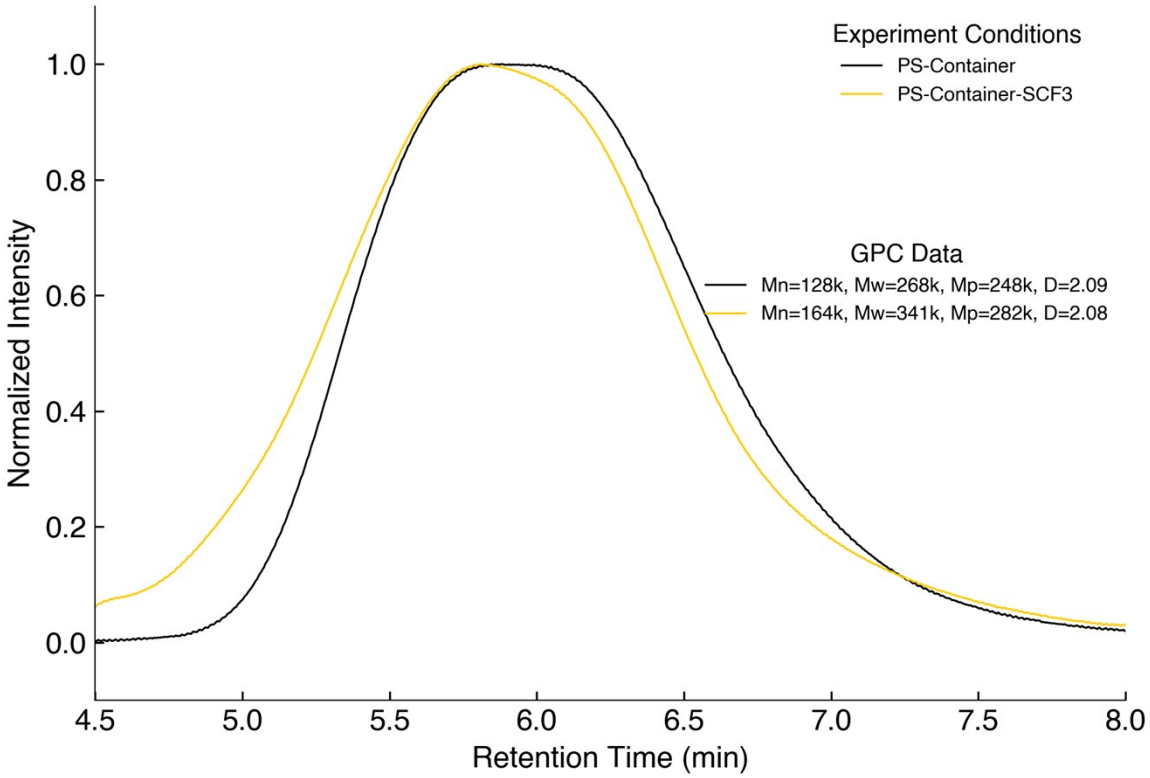

Fig. S67. Normalized GPC of PS-Coffee-Lid and PS-Coffee-Lid-SCF_3.

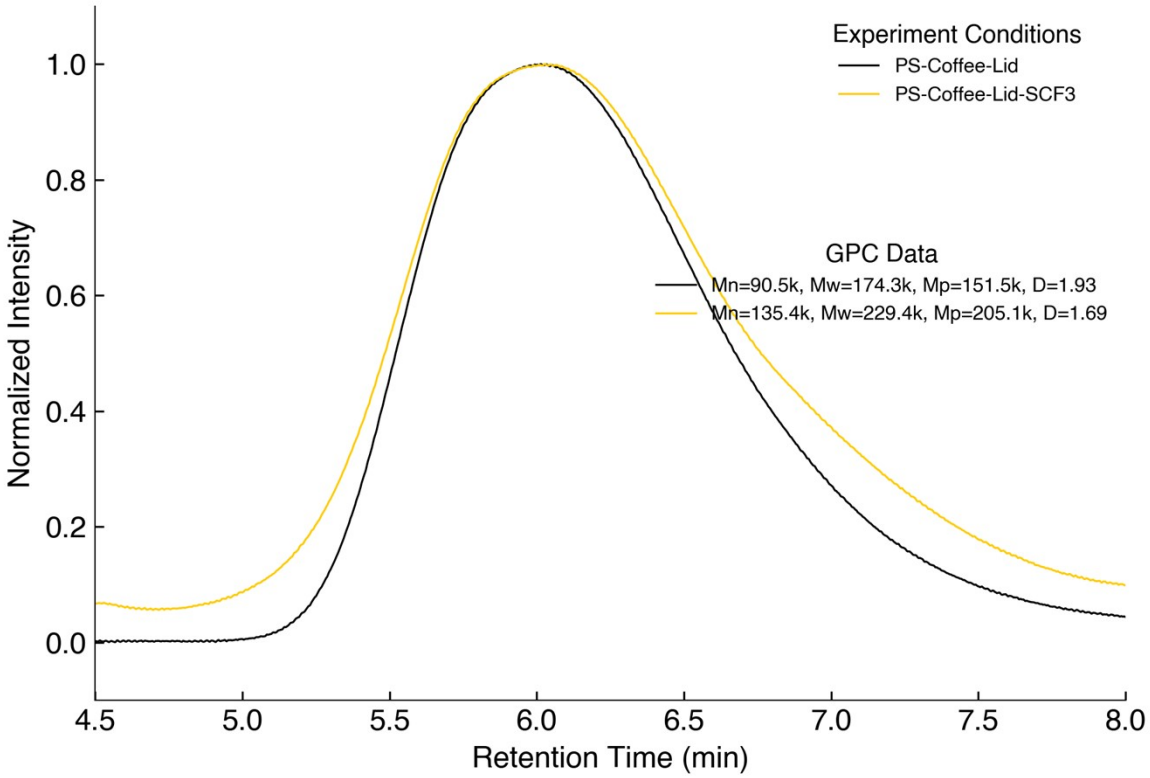

Fig. S68. Normalized GPC of PS-Petri-Dish and PS-Petri-Dish-SCF_3.

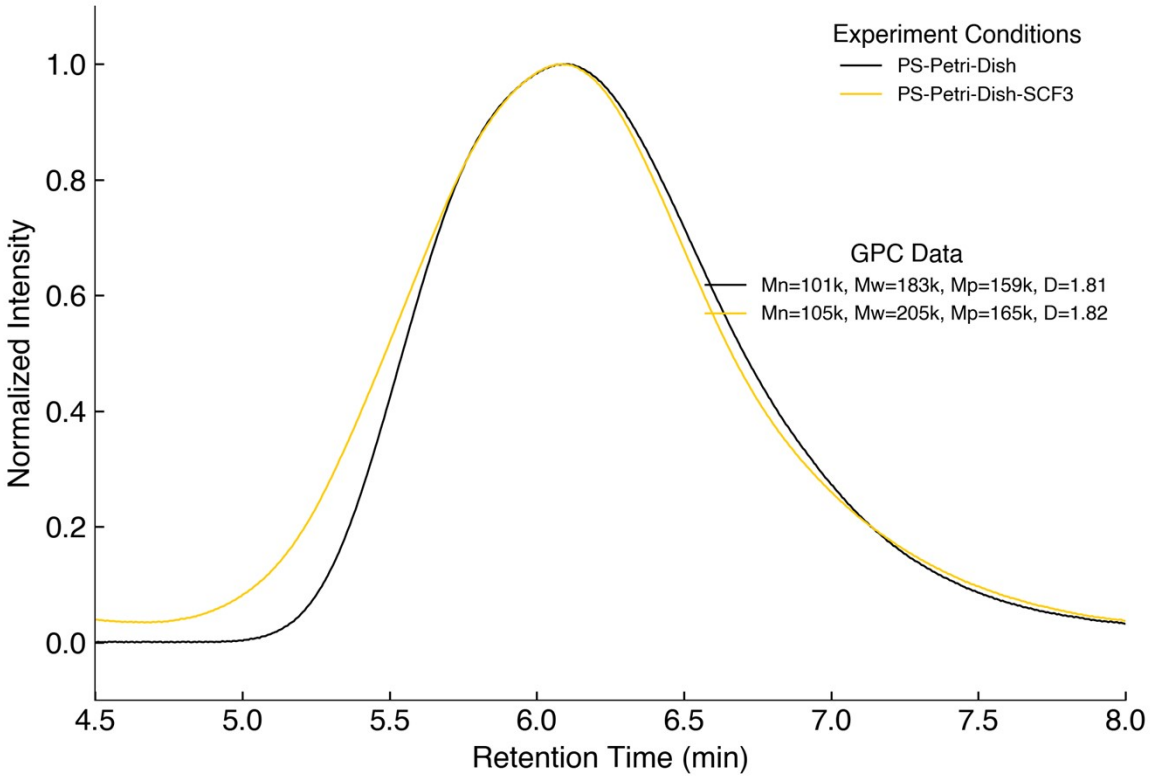

Fig. S69. Normalized GPC of PS-Red-Solo-Cup and PS-Red-Solo-Cup-SCF_3.

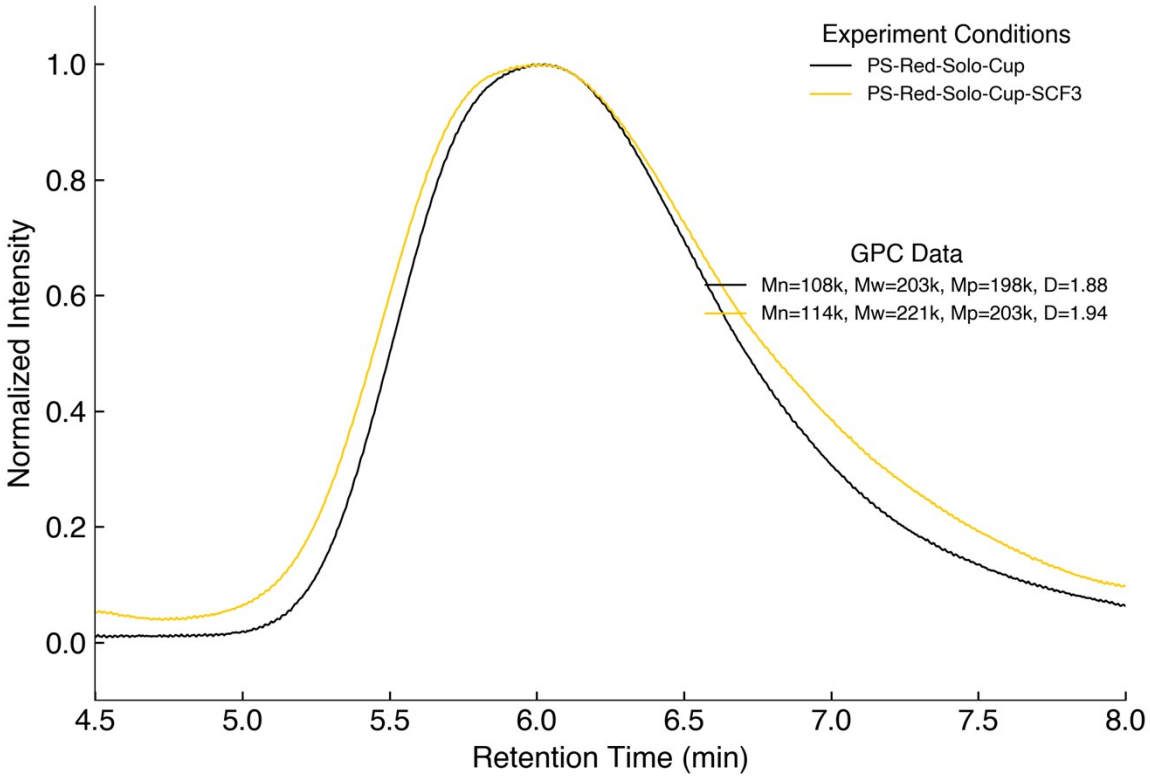

Fig. S70. Normalized GPC of PS-Blue-Cup and PS-Blue-Cup-SCF_3.

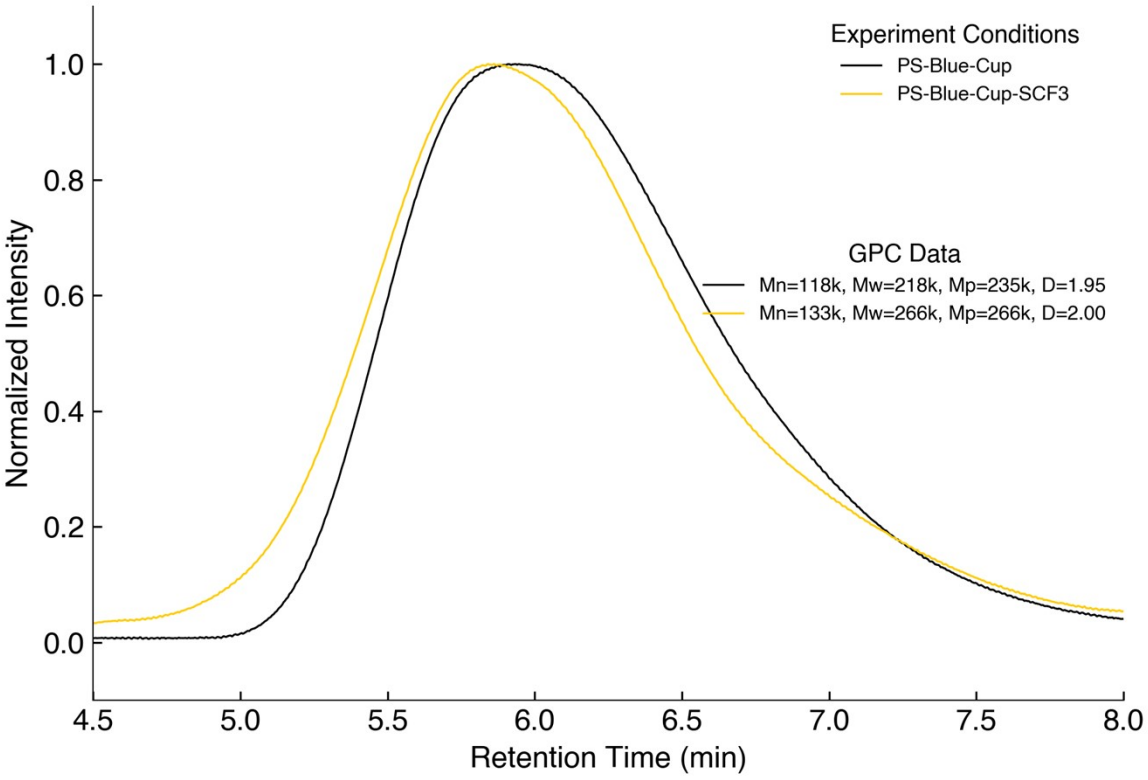

Fig. S71. ^{1}H NMR of PS-Styrofoam in $CDCl_3$.

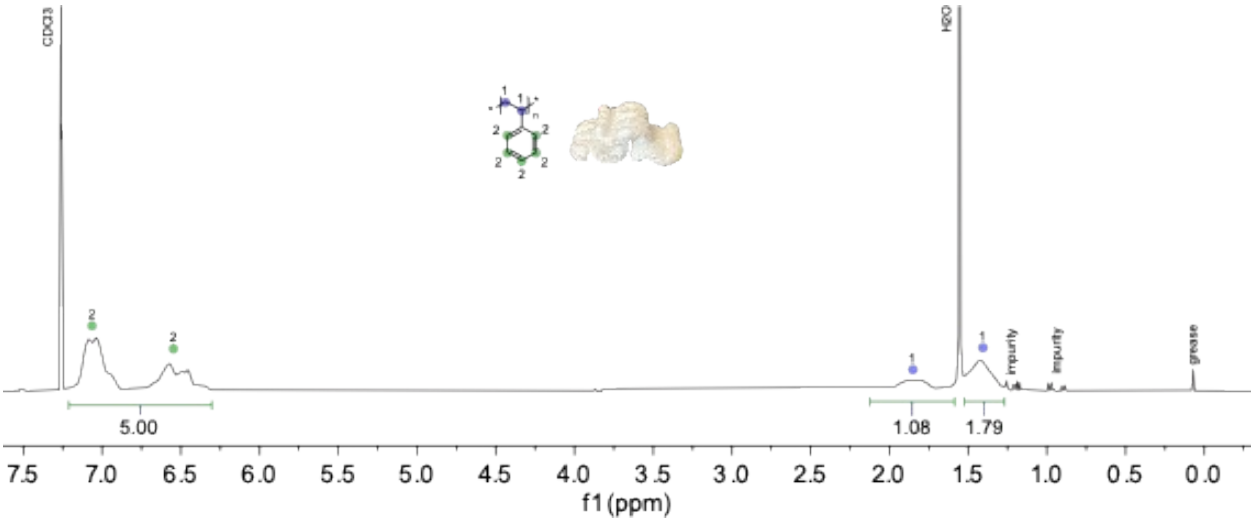

^{1}H NMR (400 MHz, $CDCl_3$) δ 7.15 – 6.21 (broad m, 5H), 2.23 – 1.65 (broad m, 1H), 1.54 – 1.24 (broad m, 2H).

Fig. S72. ^{1}H NMR of PS-Styrofoam-SCF_3 with 4,4-DFBP internal standard in $CDCl_3$.

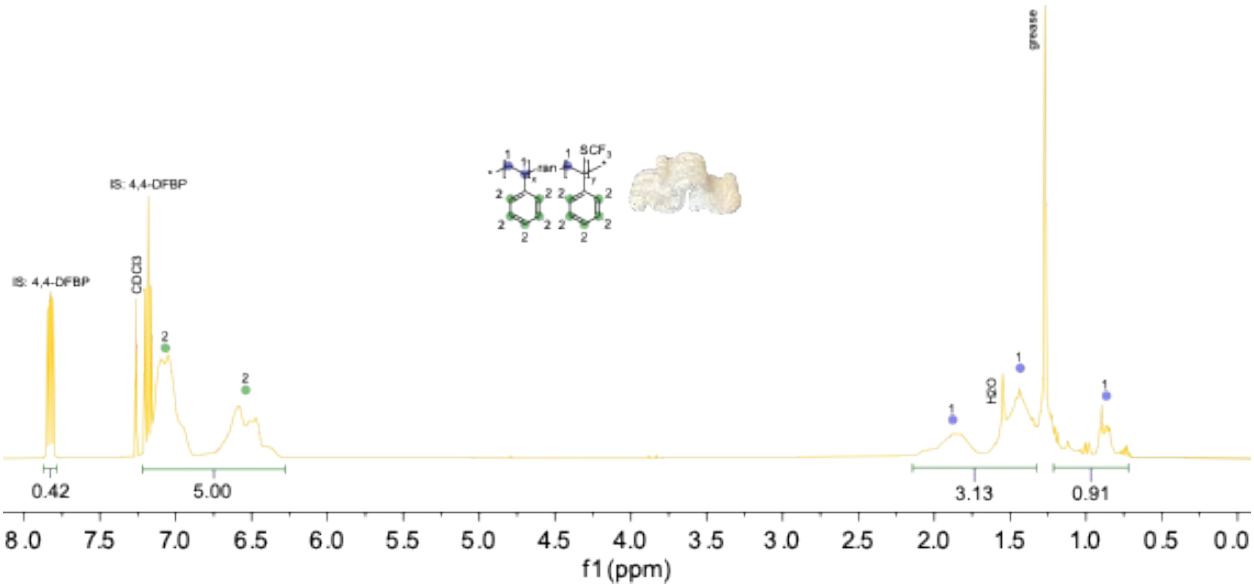

^{1}H NMR (400 MHz, $CDCl_3$) δ 7.83 (dd, *J* = 8.9, 5.4 Hz, 1H), 7.19 (t, *J* = 8.6 Hz, 1H), 7.10 – 6.25 (broad m, 5H), 2.15 – 1.30 (broad m, 1H), 1.20 – 0.80 (broad m, 2H).

Fig. S73. ^{19}F NMR of PS-Styrofoam-SCF_3 with 4,4-DFBP internal standard in $CDCl_3$.

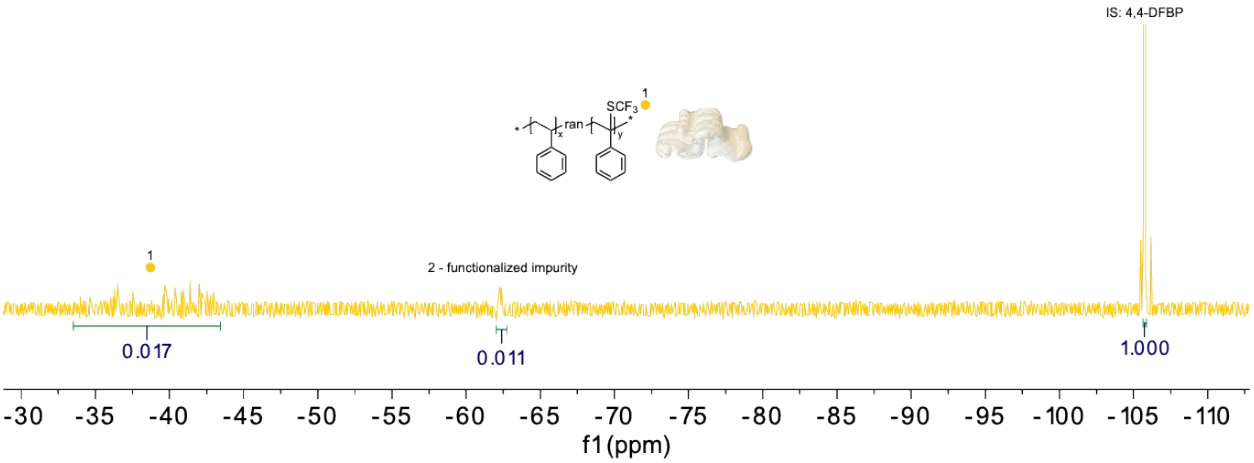

^{19}F NMR (376 MHz, $CDCl_3$) δ -33.89 – 43.10 (broad m), -62.21 (broad m), -105.73 (s).

Fig. S74. ^{1}H NMR of PS-Food-Container in $CDCl_3$.

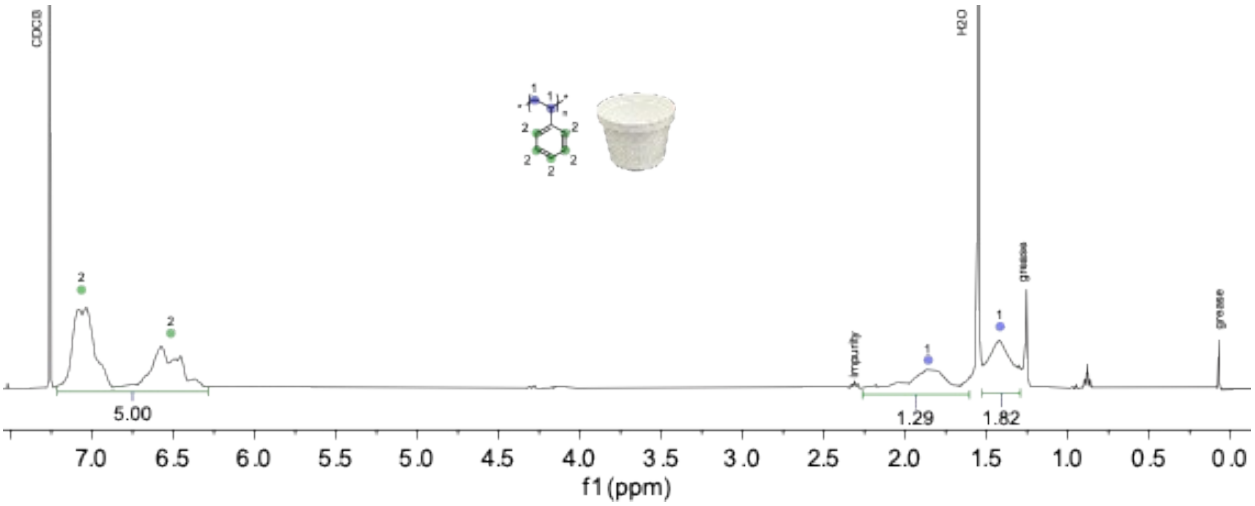

^{1}H NMR (400 MHz, $CDCl_3$) δ 7.19 – 6.27 (m, 5H), 2.25 – 1.60 (broad m, 1H), 1.50 – 1.28 (broad m, 2H).

Fig. S75. ^{1}H NMR of PS-Food-Container-SCF_3 with 4,4-DFBP internal standard in $CDCl_3$.

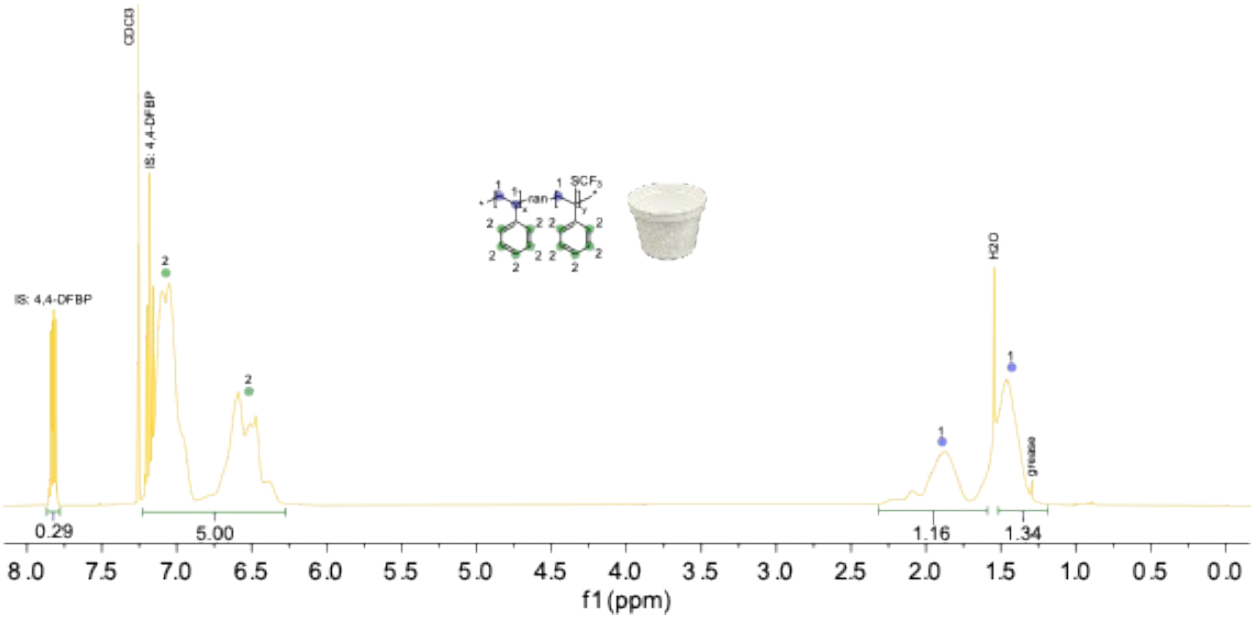

^{1}H NMR (400 MHz, $CDCl_3$) δ 7.83 (dd, *J* = 8.9, 5.4 Hz, 1H), 7.19 (t, *J* = 8.6 Hz, 1H), 7.10 (broad m, 3H), 6.60 (broad m, 2H), 1.87 (broad m, 1H), 1.45 (broad m, 2H).

Fig. S76. ^{19}F NMR of PS-Food-Container-SCF_3 with 4,4-DFBP internal standard in $CDCl_3$.

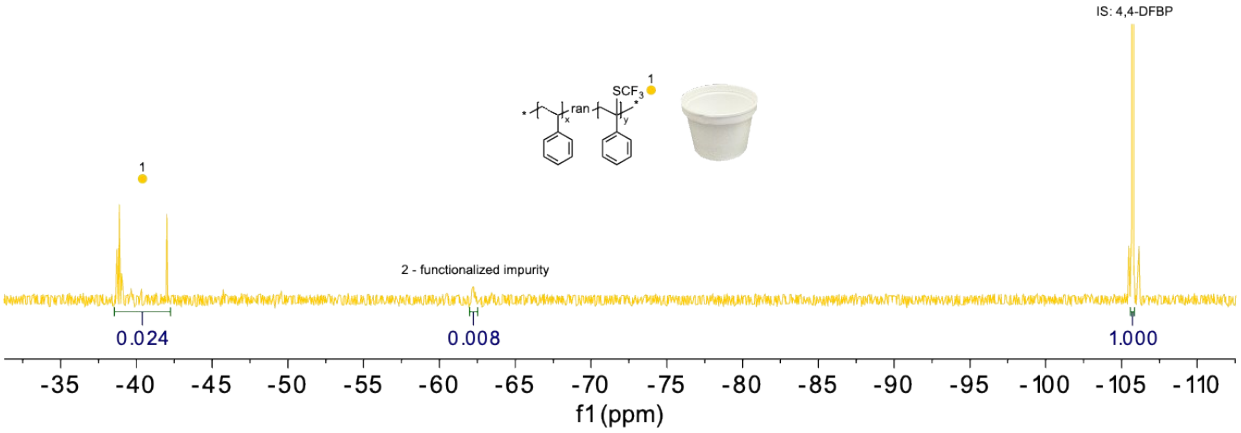

^{19}F NMR (376 MHz, $CDCl_3$) δ -38.64 – -42.32 (broad m), -62.21 (broad m), -105.73 (s).

Fig. S77. ^{1}H NMR of PS-Coffee-Lid in $CDCl_3$.

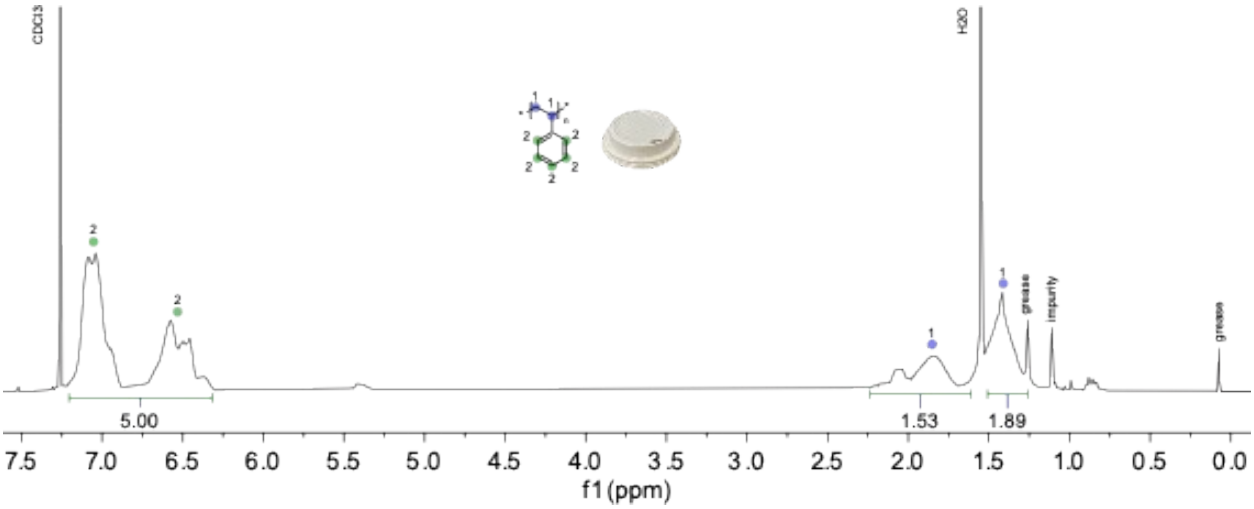

^{1}H NMR (400 MHz, $CDCl_3$) δ 7.21 – 6.28 (m, 5H), 2.22 – 1.70 (broad m, 1H), 1.51 – 1.22 (broad m, 2H).

Fig. S78. ^{1}H NMR of PS-Coffee-Lid-SCF_3 with 4,4-DFBP internal standard in $CDCl_3$.

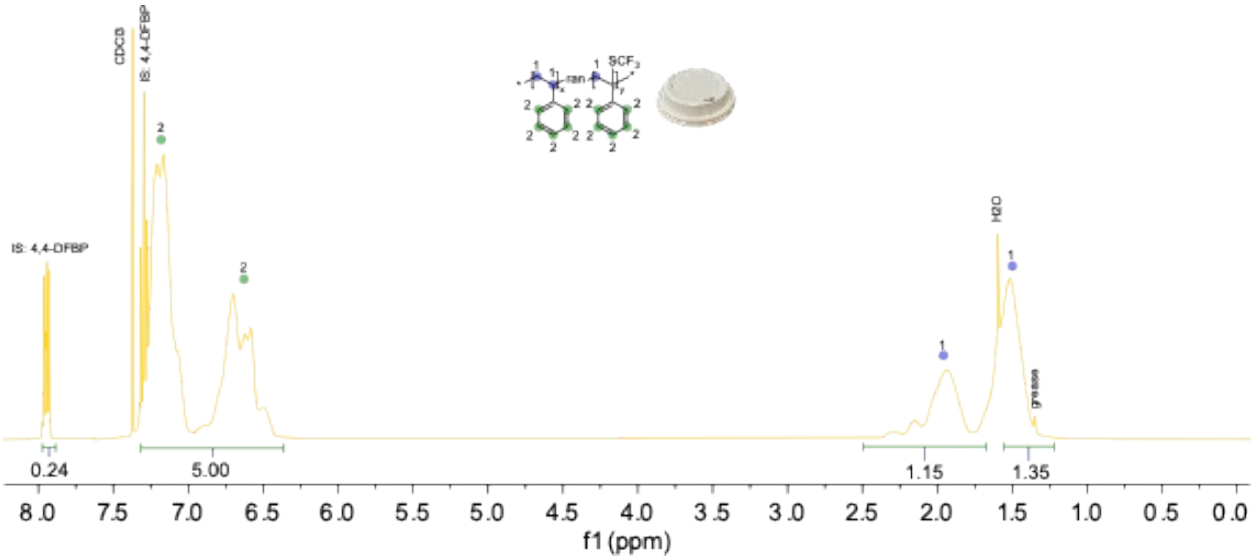

^{1}H NMR (400 MHz, $CDCl_3$) δ 7.93 (dd, *J* = 8.9, 5.4 Hz, 1H), 7.27 (t, *J* = 8.6 Hz, 1H), 7.18 – 6.42 (broad m, 5H), 2.37 – 1.68 (broad m, 1H), 1.58 – 1.20 (broad m, 2H).

Fig. S79. ^{19}F NMR of PS-Coffee-Lid-SCF_3 with 4,4-DFBP internal standard in $CDCl_3$.

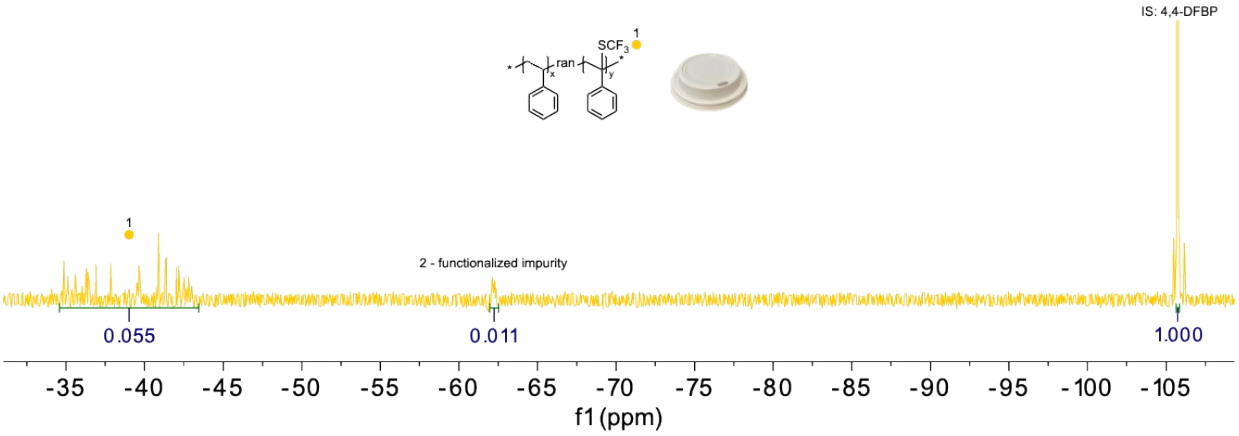

^{19}F NMR (376 MHz, $CDCl_3$) δ -34.64 – -42.67 (broad m), -62.21 (broad m), -105.73 (s).

Fig. S80. ^{1}H NMR of PS-Petri-Dish in $CDCl_3$.

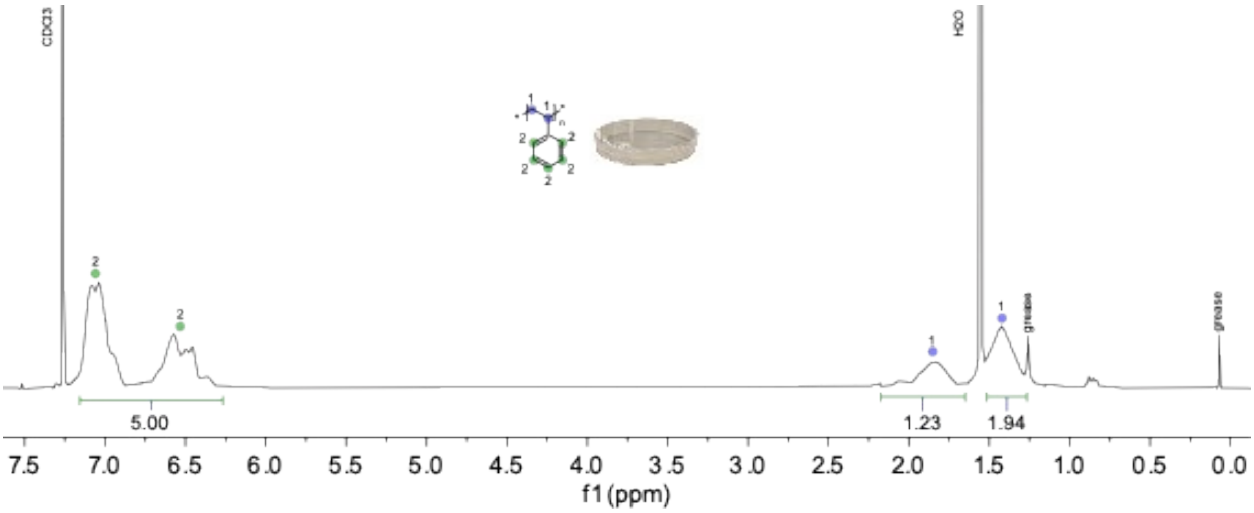

^{1}H NMR (400 MHz, $CDCl_3$) δ 7.20 – 6.25 (m, 5H), 2.21 – 1.62 (broad m, 1H), 1.52 – 1.30 (broad m, 2H).

Fig. S81. ^{1}H NMR of PS-Petri-Dish-SCF_3 with 4,4-DFBP internal standard in $CDCl_3$.

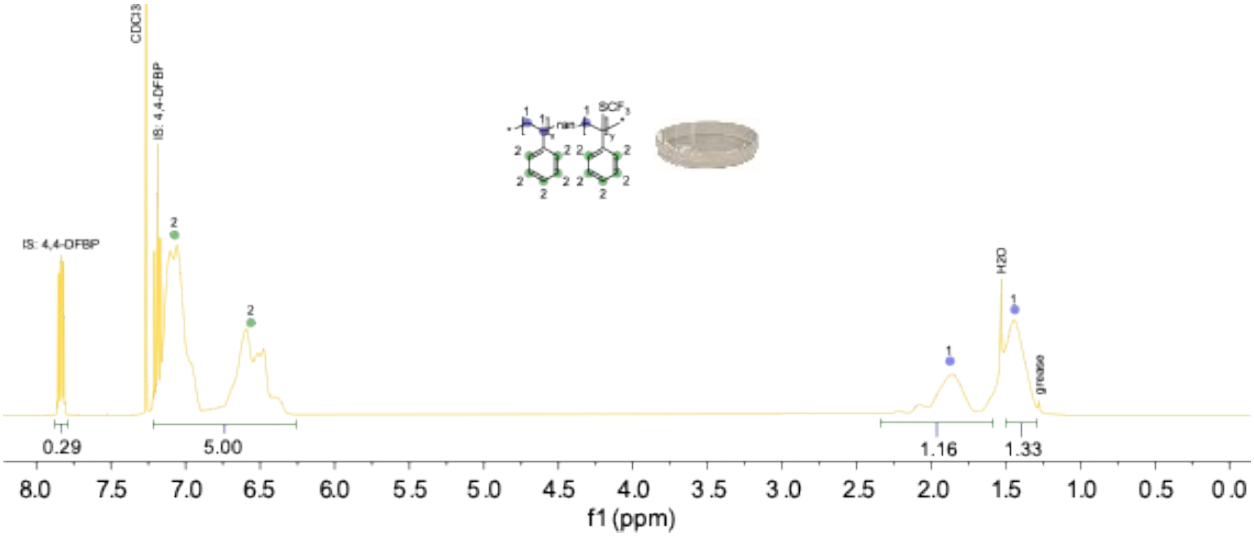

^{1}H NMR (400 MHz, $CDCl_3$) δ 7.83 (dd, *J* = 8.9, 5.4 Hz, 1H), 7.19 (t, *J* = 8.6 Hz, 1H), 7.13 – 6.25 (broad m, 5H), 2.25 – 1.60 (broad m, 1H), 1.50 – 1.25 (broad m, 2H).

Fig. S82. ^{19}F NMR of PS-Petri-Dish-SCF_3 with 4,4-DFBP internal standard in $CDCl_3$.

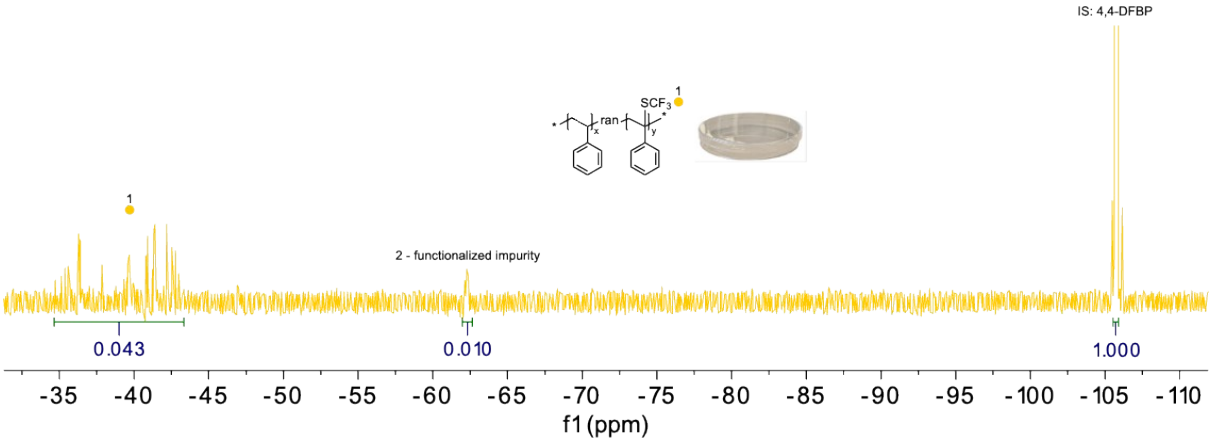

^{19}F NMR (376 MHz, $CDCl_3$) δ -34.9 – 42.89 (broad m), -62.21 (broad m), -105.73 (s).

Fig. S83. ^{1}H NMR of PS-Red-Solo-Cup in $CDCl_3$.

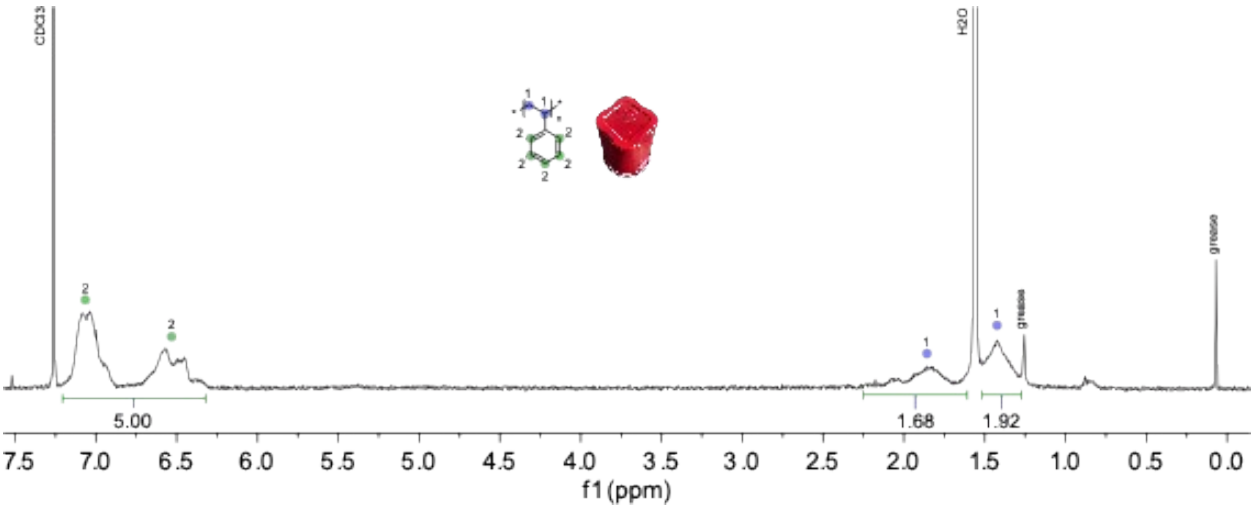

^{1}H NMR (400 MHz, $CDCl_3$) δ 7.19 – 6.24 (broad m, 5H), 2.25 - 1.65 (broad m, 1H), 1.51 – 1.34 (broad m, 2H).

Fig. S84. ^{1}H NMR of PS-Red-Solo-Cup-SCF_3 with 4,4-DFBP internal standard in $CDCl_3$.

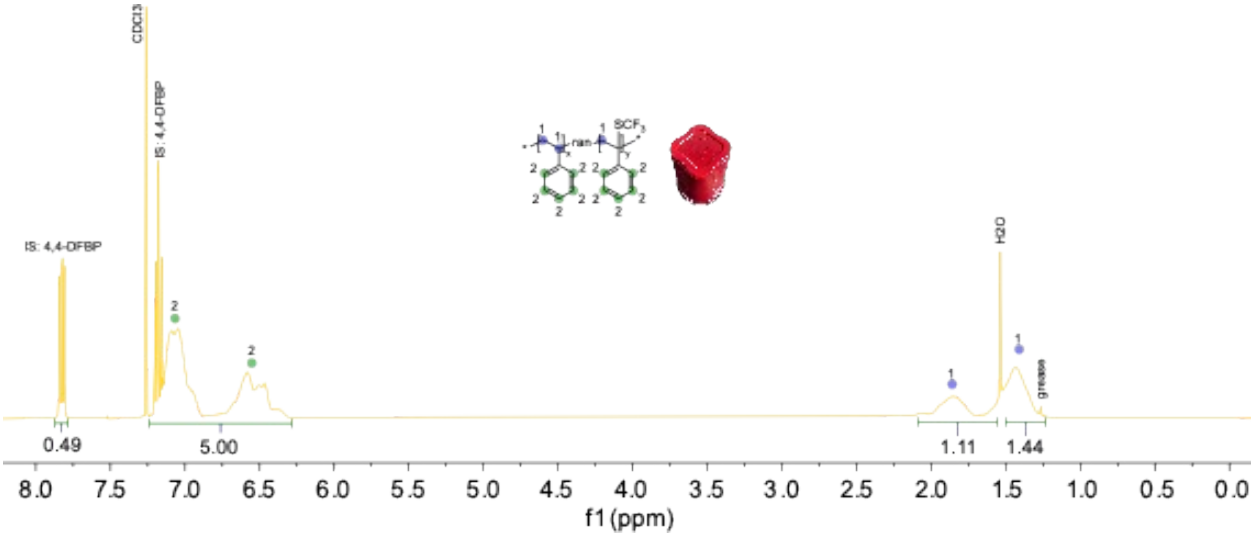

^{1}H NMR (400 MHz, $CDCl_3$) δ 7.83 (dd, *J* = 8.9, 5.4 Hz, 1H), 7.19 (t, *J* = 8.6 Hz, 1H), 7.19 – 6.30 (broad m, 5H), 2.15 – 1.58 (broad m, 1H), 1.52 – 1.25 (broad m, 2H).

Fig. S85. ^{19}F NMR of PS-Red-Solo-Cup-SCF_3 with 4,4-DFBP internal standard in $CDCl_3$.

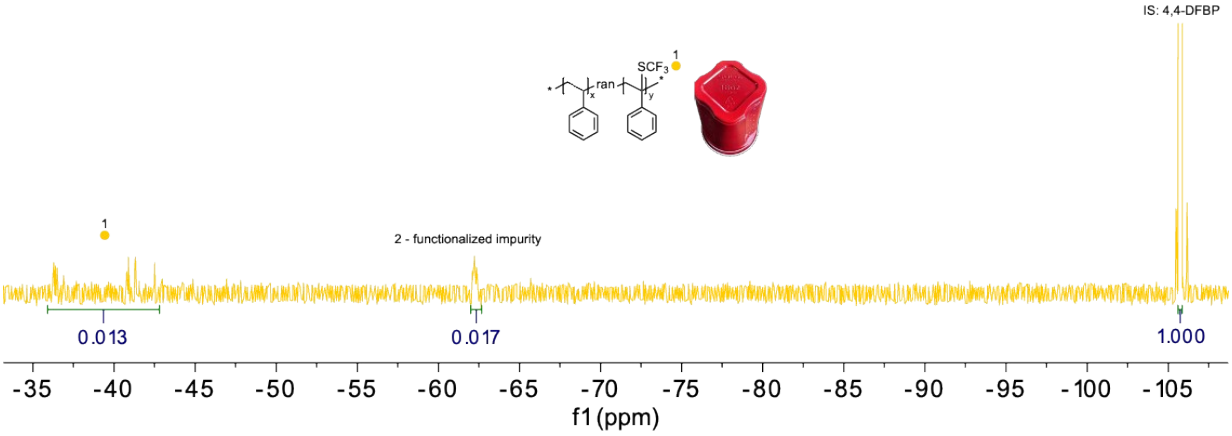

^{19}F NMR (376 MHz, $CDCl_3$) δ -36.15 – -42.64 (broad m), -62.21 (broad m), -105.73 (s).

Fig. S86. ^{1}H NMR of PS-Blue-Cup in $CDCl_3$.

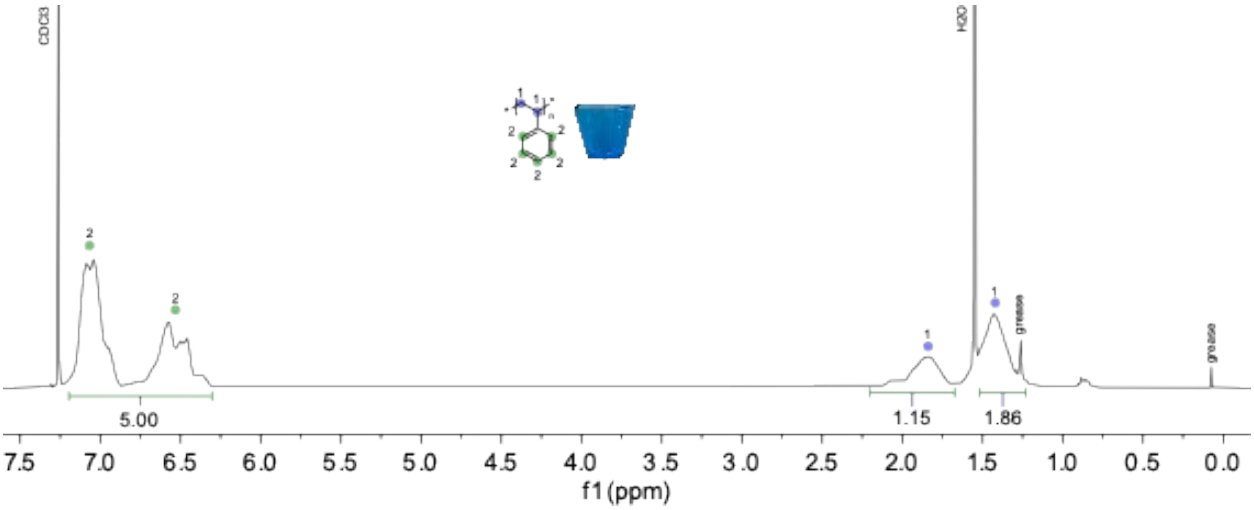

^{1}H NMR (400 MHz, $CDCl_3$) δ 7.20 – 6.28 (broad m, 5H), 2.23 – 1.68 (broad m, 1H), 1.50 – 1.22 (broad m, 2H).

Fig. S87. ^{1}H NMR of PS-Blue-Cup-SCF_3 with 4,4-DFBP internal standard in $CDCl_3$.

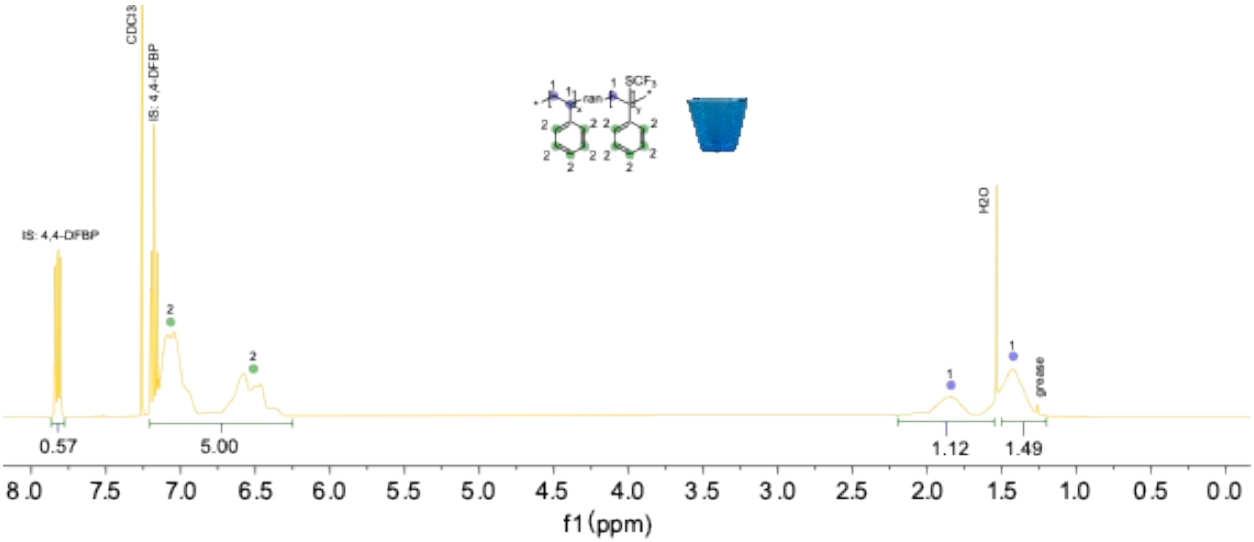

^{1}H NMR (400 MHz, $CDCl_3$) δ 7.83 (dd, *J* = 8.9, 5.4 Hz, 1H), 7.19 (t, *J* = 8.6 Hz, 1H), 7.19 – 6.27 (broad m, 5H), 2.22 – 1.60 (broad m, 1H), 1.52 – 1.20 (broad m, 2H).

Fig. S88. ^{19}F NMR of PS-Blue-Cup-SCF_3 with 4,4-DFBP internal standard in $CDCl_3$.

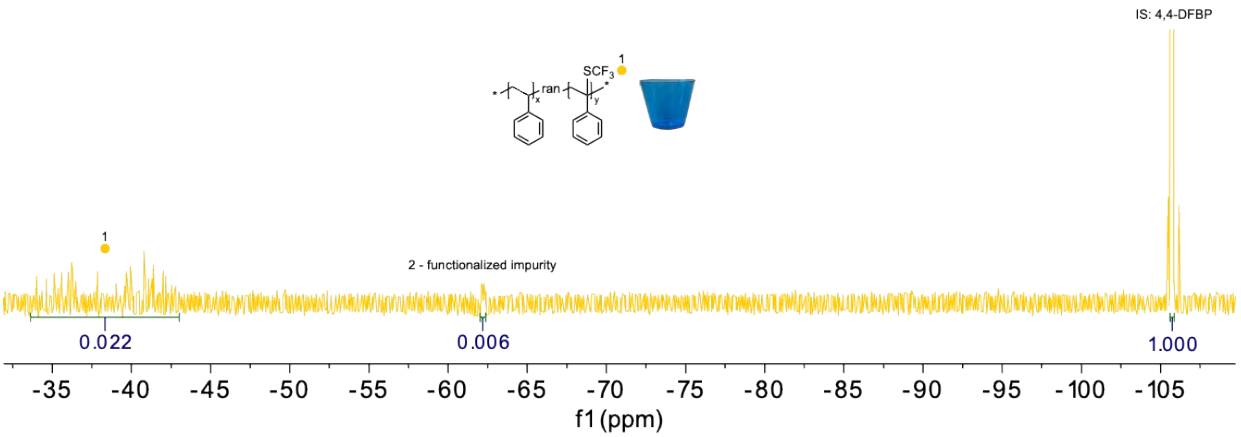

^{19}F NMR (376 MHz, $CDCl_3$) δ -33.24 – 42.80 (broad m), -62.21 (broad m), -105.73 (s).

Fig. S89. Isothermal TGA at 300°C of PS-Styrofoam and PS-Styrofoam-SCF_3.

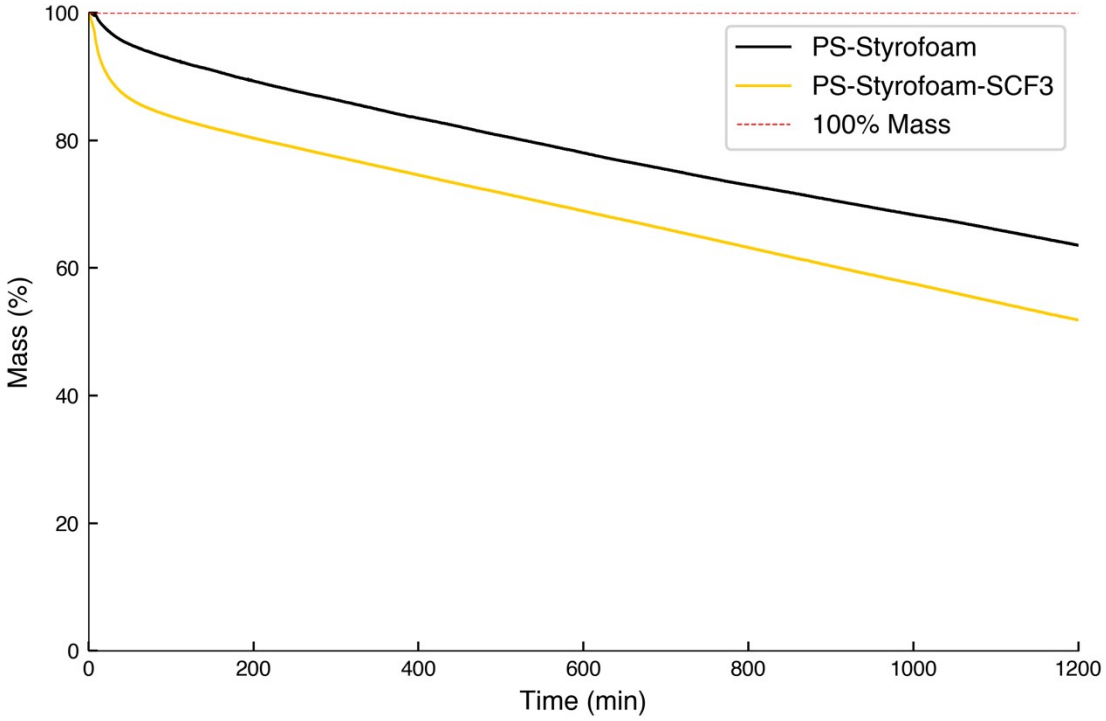

Fig. S90. Dynamic TGA of PS-Styrofoam and PS-Styrofoam-SCF_3.

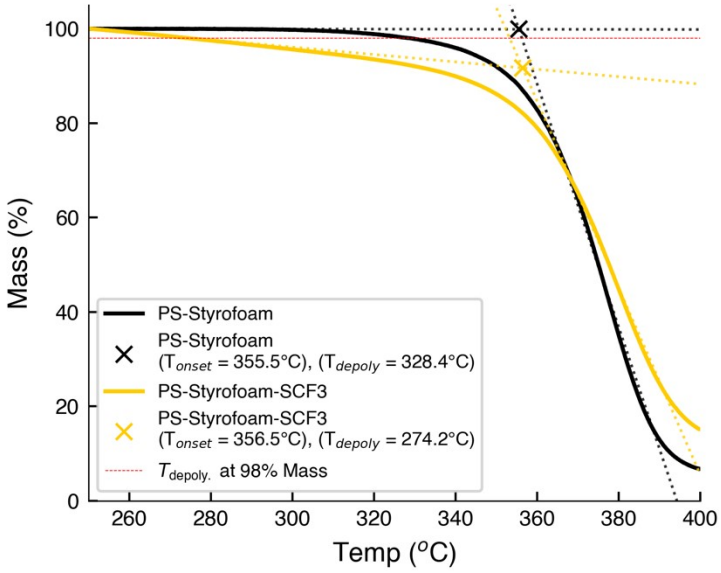

Fig. S91. Isothermal TGA at 300°C of PS-Petri-Dish and PS-Petri-Dish-SCF_3.

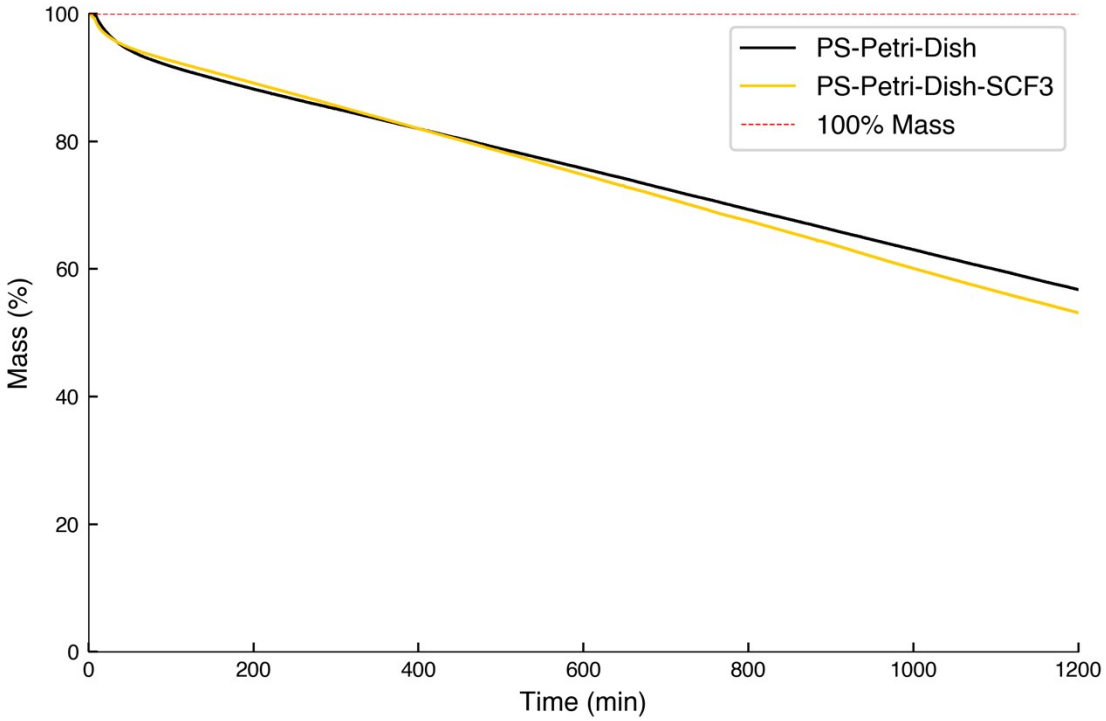

Fig. S92. Dynamic TGA of PS-Petri-Dish and PS-Petri-Dish-SCF_3.

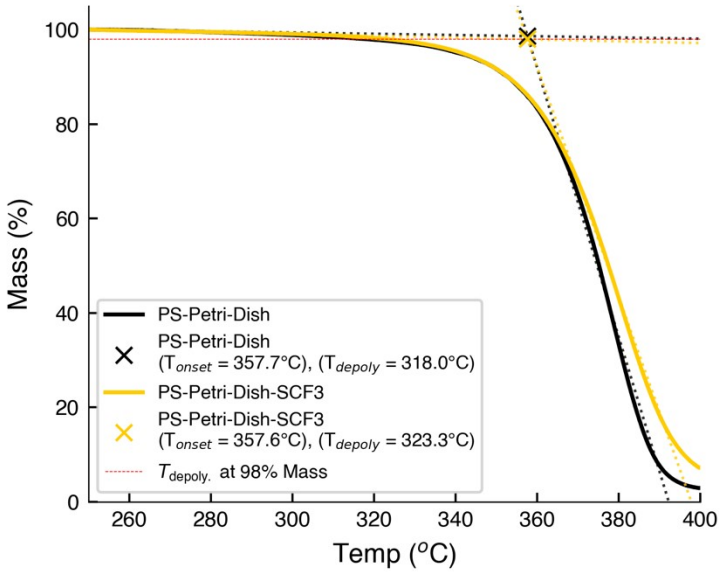

Fig. S93. Isothermal TGA at 300°C of PS-Blue-Cup and PS-Blue-Cup-SCF_3.

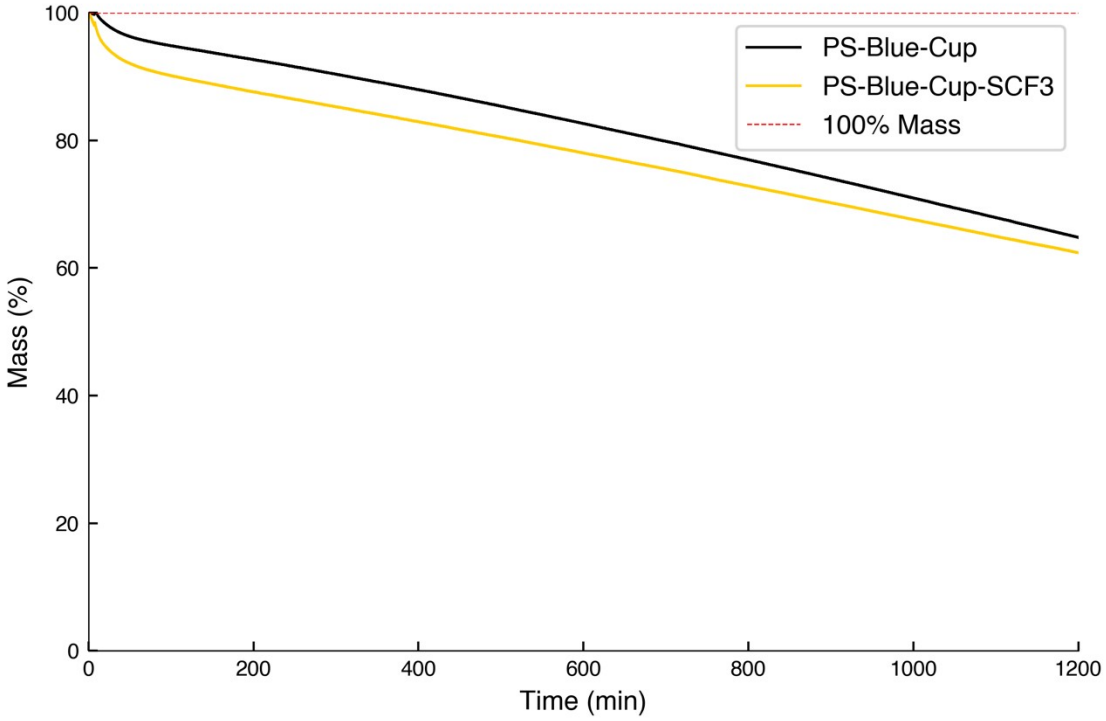

Fig. S94. Dynamic TGA of PS-Blue-Cup and PS-Blue-Cup-SCF_3.

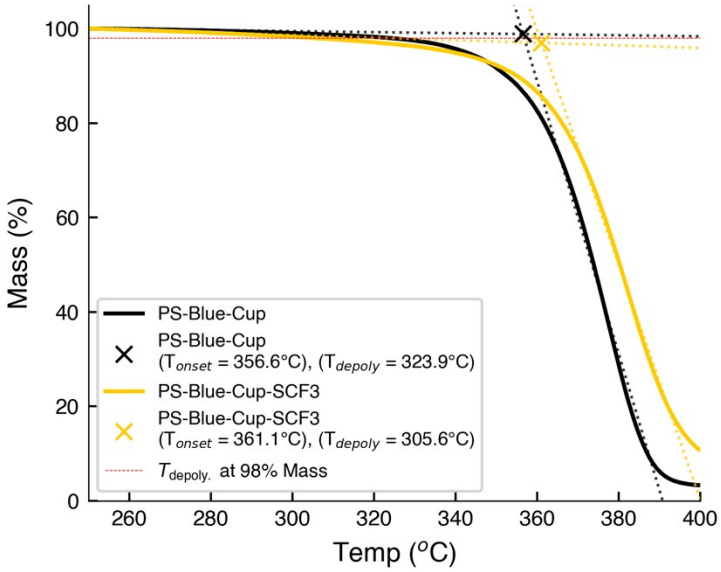

Fig. S95. Isothermal TGA at 300°C of PS-Container and PS-Container-SCF_3.

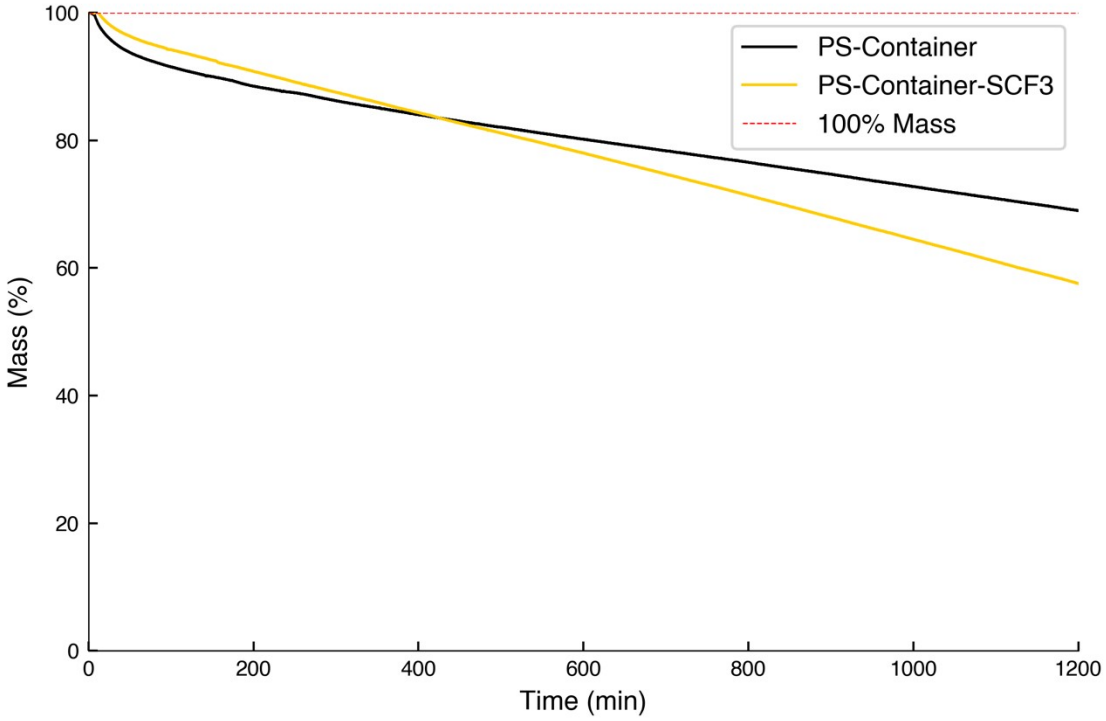

Fig. S96. Dynamic TGA of PS-Container and PS-Container-SCF_3.

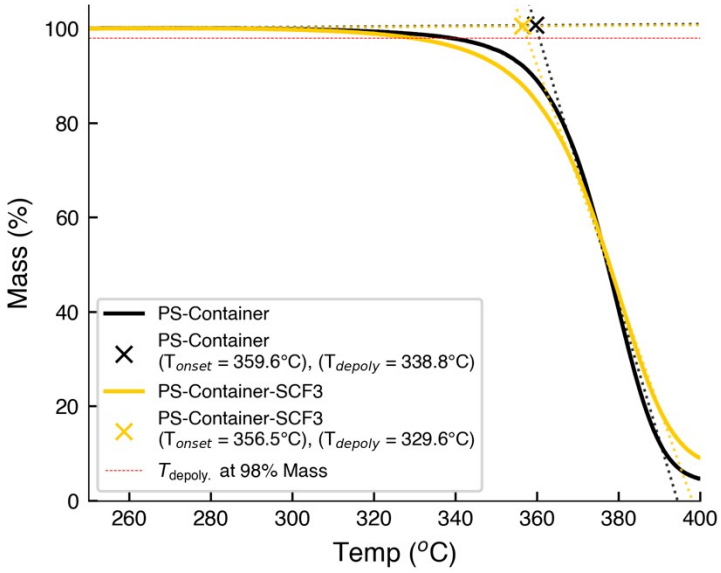

Fig. S97. Isothermal TGA at 300°C of PS-Coffee-Lid and PS-Coffee-Lid-SCF_3.

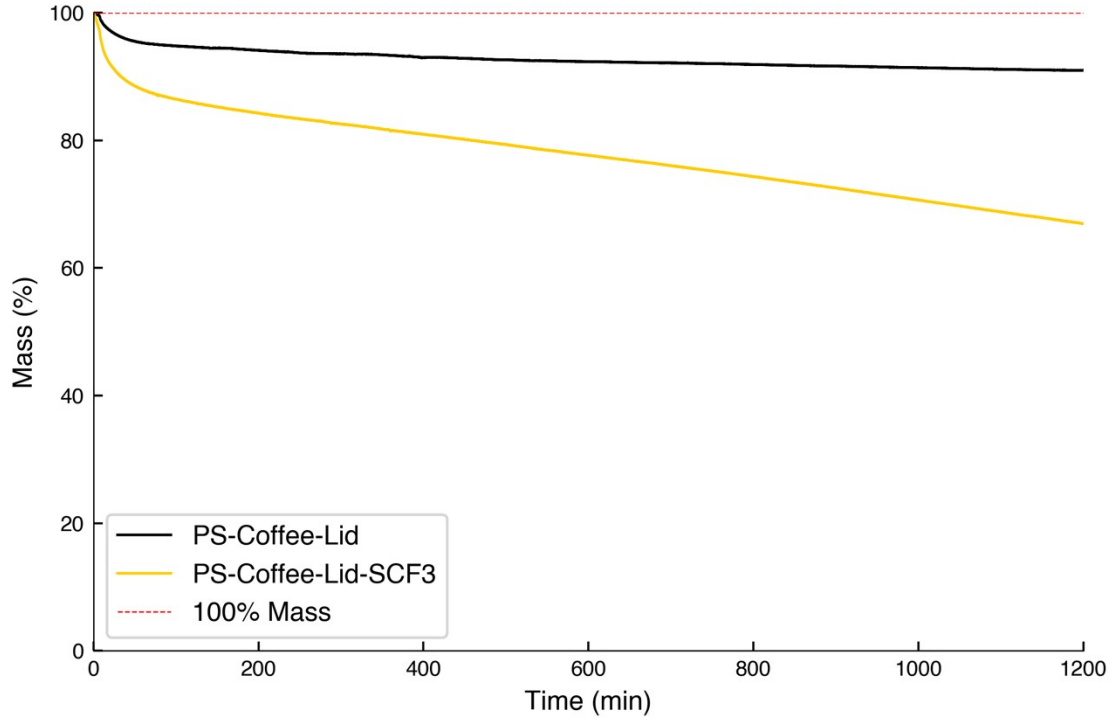

Fig. S98. Dynamic TGA of PS-Coffee-Lid and PS-Coffee-Lid-SCF_3.

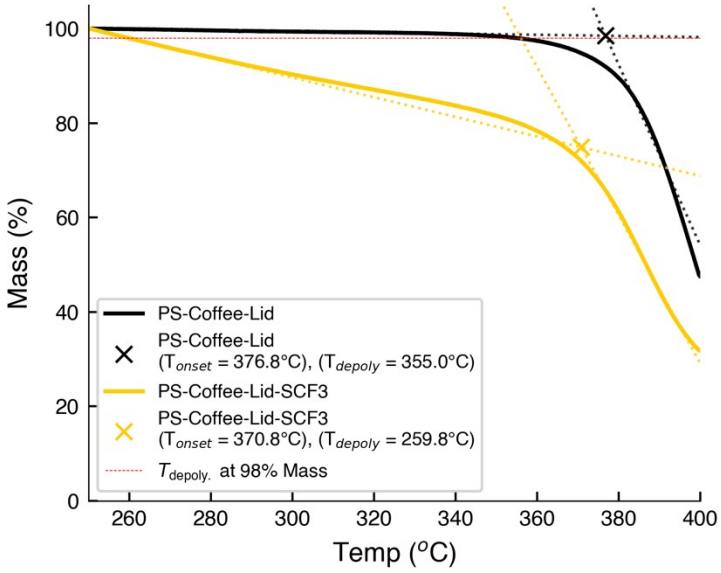

Fig. S99. Isothermal TGA at 300°C of PS-Red-Solo-Cup and PS-Red-Solo-Cup-SCF_3.

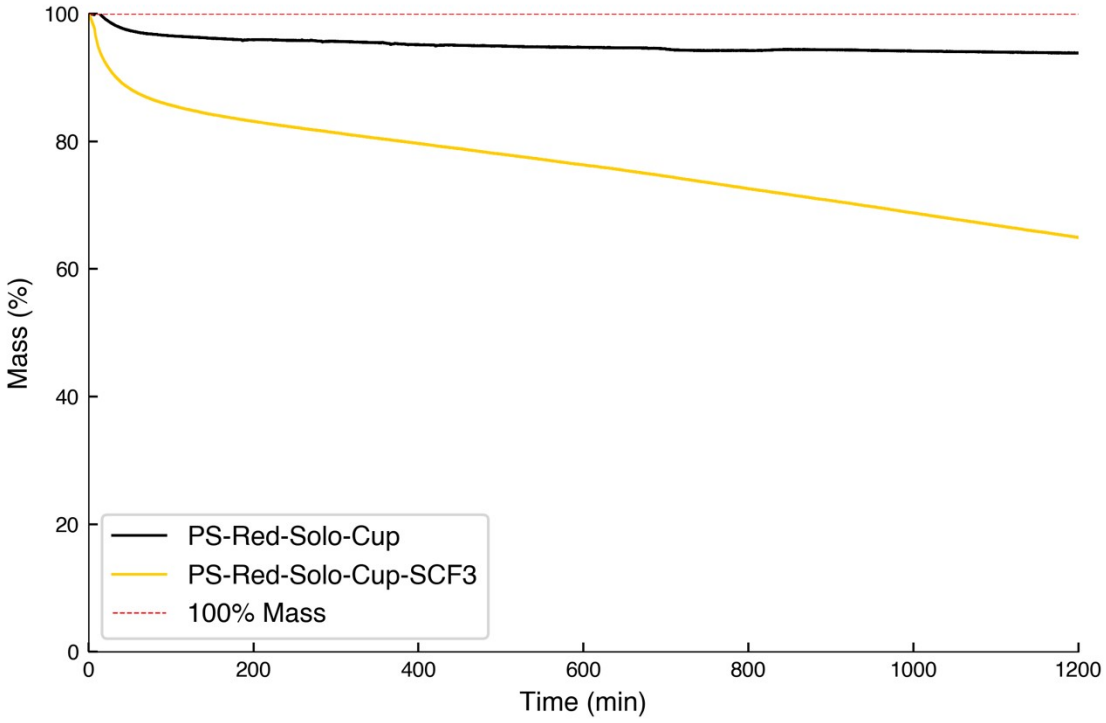

Fig. S100. Dynamic TGA of PS-Red-Solo-Cup and PS-Red-Solo-Cup-SCF_3.

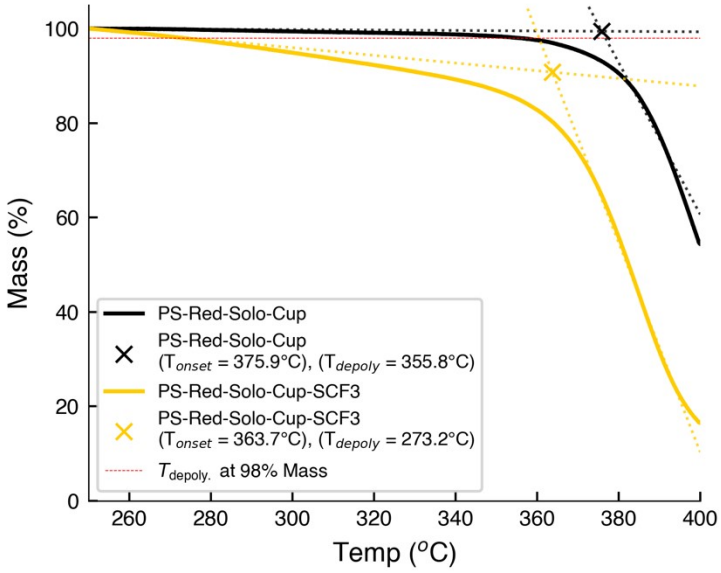

DFT Calculations

Fig. S101. Proposed mechanism for initial stages of depolymerization for unfunctionalized and post-functionalized polystyrene model systems. Solvated Gibbs free energies at 573 K for each reaction are reported (see **Computational Methods** for full details).

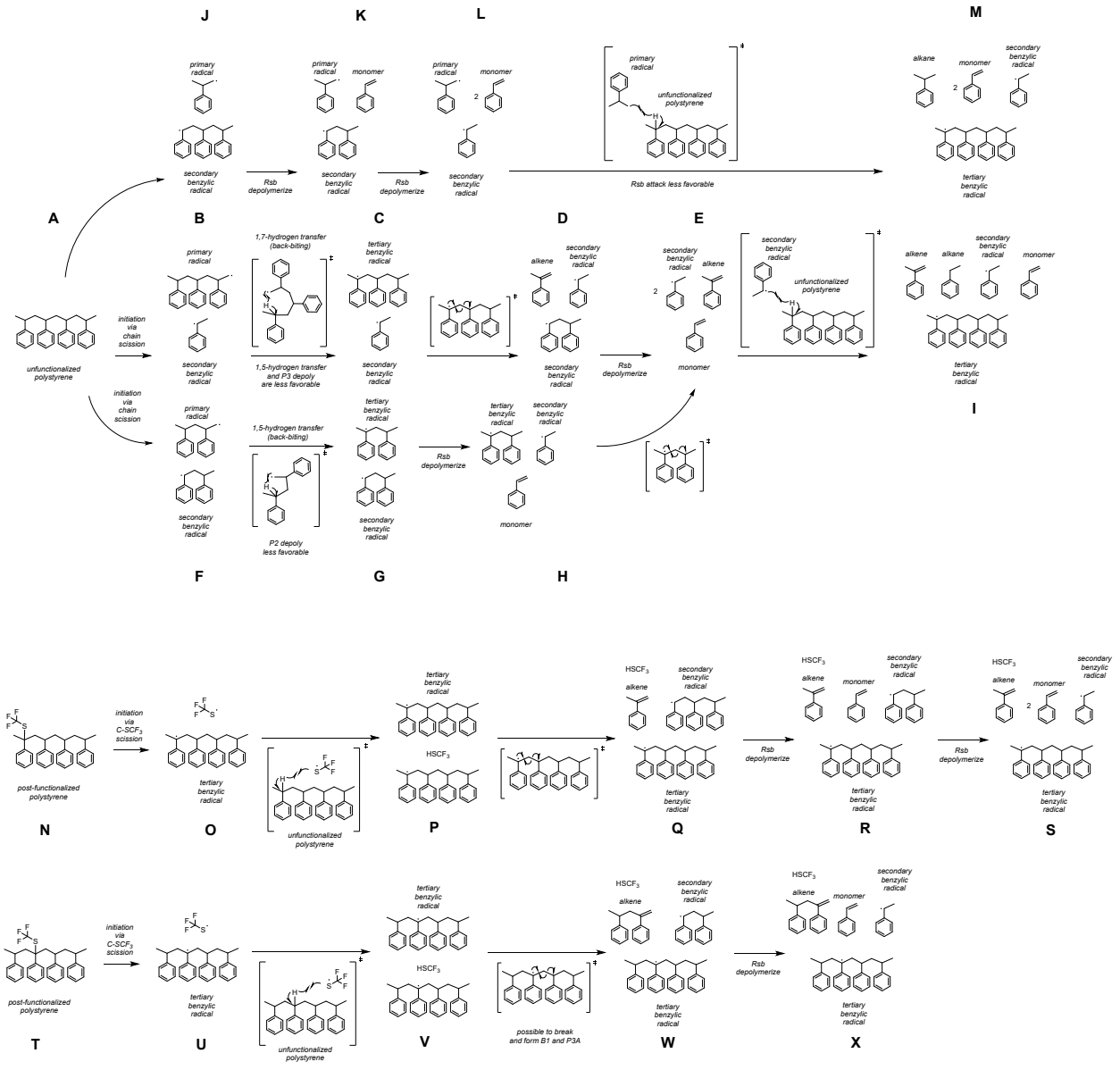

Proposed mechanism and density functional theory investigations

To further rationalize the relative ease of depolymerization of PS-SCF_3 compared to PS, we propose a mechanism to compare the initial stages of the depolymerization process using tetrameric model systems (**Fig. S101**). Our mechanism terminates at the stage where a radical abstracts a hydrogen from another PS tetramer, as all further downstream mechanistic steps are the same for both mechanisms (i.e., hydrogen abstraction from PS, followed by chain scission of a tertiary benzylic radical and repeated depolymerization of a secondary benzylic radical, R_{sb}). To simplify the model further, we consider that oligomeric radicals must depolymerize into monomeric

radicals, and that hydrogen abstraction from PS occurs only by monomeric primary (R_p) or secondary benzylic (R_{sb}) radicals on the first benzylic C-H of PS. This is also supported by the fact that depolymerization is in general calculated to be more facile than hydrogen abstraction at our level of theory (**Table S8**). We do not consider the role of radical termination processes in our mechanism and further note that a detailed investigation of the mechanism of depolymerization mechanism is beyond the scope of this work.

Table S8. Barriers for processes in depolymerization of PS and PS-SCF_3.

Reaction	**$\Delta G^{\ddagger}$ / kJ / mol @ 573 K**
R_p 1,7-hydrogen transfer	63.4 [trimeric]
R_p 1,5-hydrogen transfer	86.6 [trimeric], 92.6 [dimeric]
R_{tb} chain scission (reported as [R_{sb} length, alkene length])	99.2 [2, 1], 100.7 [1, 1], 106.9 [3, 1], 103.5 [2, 2],
R_{sb} depolymerization	99.4 [trimeric], 95.5 [dimeric]
R_p depolymerization	101.7 [trimeric], 111.6 [dimeric]
R_{sb} hydrogen abstraction (reported benzylic C-H abstraction site)	119.1 [1], 129.2 [2]
R_p hydrogen abstraction (reported benzylic C-H abstraction site)	106.5 [1], 105.3 [2]
SCF_3 hydrogen abstraction (reported benzylic C-H abstraction site)	71.0 [1], 78.8 [2]

The mechanism for the initiation of PS depolymerization follows prior well-established works,[37–39] where homolytic scission of the carbon chain can generates primary (R_p) and secondary benzylic (R_{sb}) radicals. At each juncture, a variety of reactions can happen between the multitude of intermediates, including hydrogen abstraction by multiple radicals, depolymerization, chain scission and back biting. Following the energy span model, we reduce the number of considerations and detail the minimum energy span for each path in the mechanism to arrive at their respective final states.[40]

From PS (**A**), homolytic chain scission can occur, with three possibilities for the formation of R_p and R_{sb} (**B**, **F**, **J**, **Fig. S101**).

- From **B**, R_p can undergo a 1,7-hydrogen transfer (known as back-biting) to form tertiary benzylic (R_{tb}) radicals (**C**). 1,5-hydrogen transfers for R_p are considerably less favorable as the five-membered transition state is more strained than the seven-membered transition state for 1,7-hydrogen transfer. R_{tb} subsequently undergoes scission to form an alkene and an oligomeric R_{sb} (**D**). The oligomeric R_{sb} depolymerizes (**E**), and the monomeric R_{sb} abstracts a hydrogen from another unfunctionalized PS chain, generating another R_{tb} capable of further chain scission (**I**). This path is shown in **Fig. S101**.
- From **F**, R_p can only undergo a 1,5-hydrogen transfer to form R_{tb} (**G**). Again, depolymerization or hydrogen abstraction by both R_p and R_{sb} are less favorable. The oligomeric R_{sb} formed from initial chain scission depolymerizes (**H**), and R_{tb} subsequently undergoes chain scission to form an alkene and R_{sb} (**E**). R_{sb} abstracts a hydrogen from PS to form R_{tb} for propagation (**I**). This path is shown in **Fig. S101**.

- From **J**, oligomeric R_{sb} undergoes two depolymerizations (**K**, **L**). R_p abstracts a hydrogen from PS to form R_{tb} for propagation (**M**). Abstraction by R_{sb} is less favored as it is a less reactive radical compared to R_p. This path is shown in **Fig. S101**.

The path from **B** through **I** is the most facile pathway for the depolymerization of PS in our mechanism, with the highest barrier for the process at +301.1 kJ/mol. In this path, the hydrogen abstraction by R_{sb} (**E-I**) is the rate-determining step, and all rearrangements and depolymerizations before are slightly more facile. Comparatively, the path from **F** to **I** is disfavored as the formation of the dimeric R_p and R_{sb} is less favorable, and that the dimeric R_p must undergo the less favorable 1,5-hydrogen transfer to form R_{tb}, with a barrier of +313.9 kJ/mol. The subsequent path after **G** is facile compared to this barrier. The path from **J** to **M** is also significantly less facile – while the formation of R_p and R_{sb} is slightly more facile than the other paths, R_p is unable to rearrange to form a more stable R_{tb} to lower the energy of the pathway. Consequently, while hydrogen abstraction by R_p is more facile than R_{sb}, it remains the highest amongst the three considered pathways at +346.2 kJ/mol.

Fig. S102. Reaction profile diagram for the depolymerization of tetrameric PS, via states **B** through **I**.

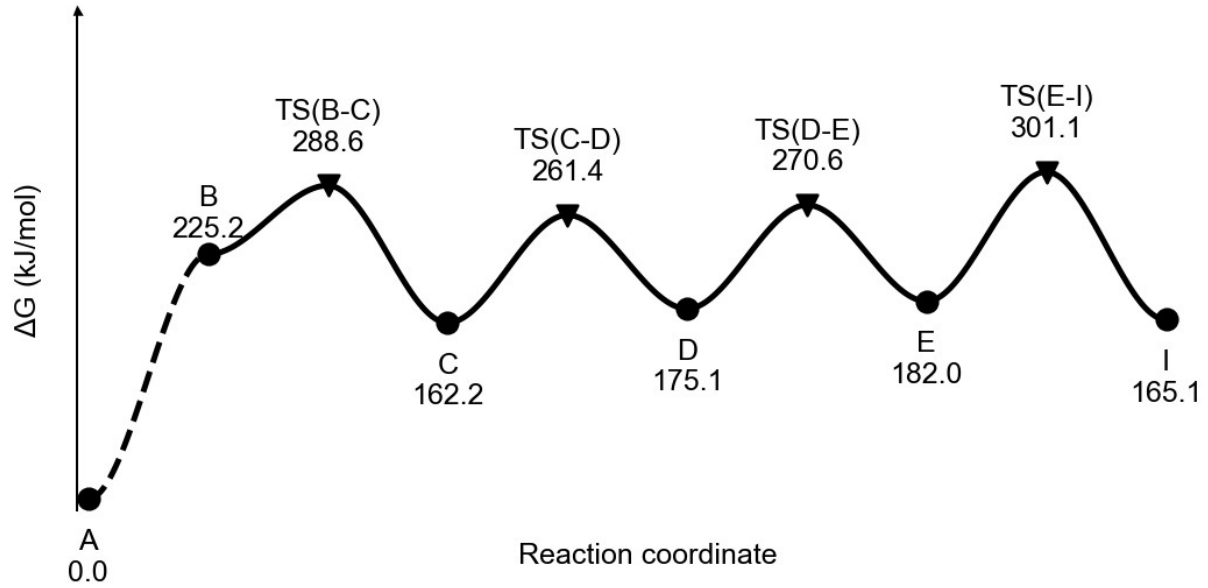

Fig. S103. Reaction profile diagram for the depolymerization of tetrameric PS, via states **F** through **I**.

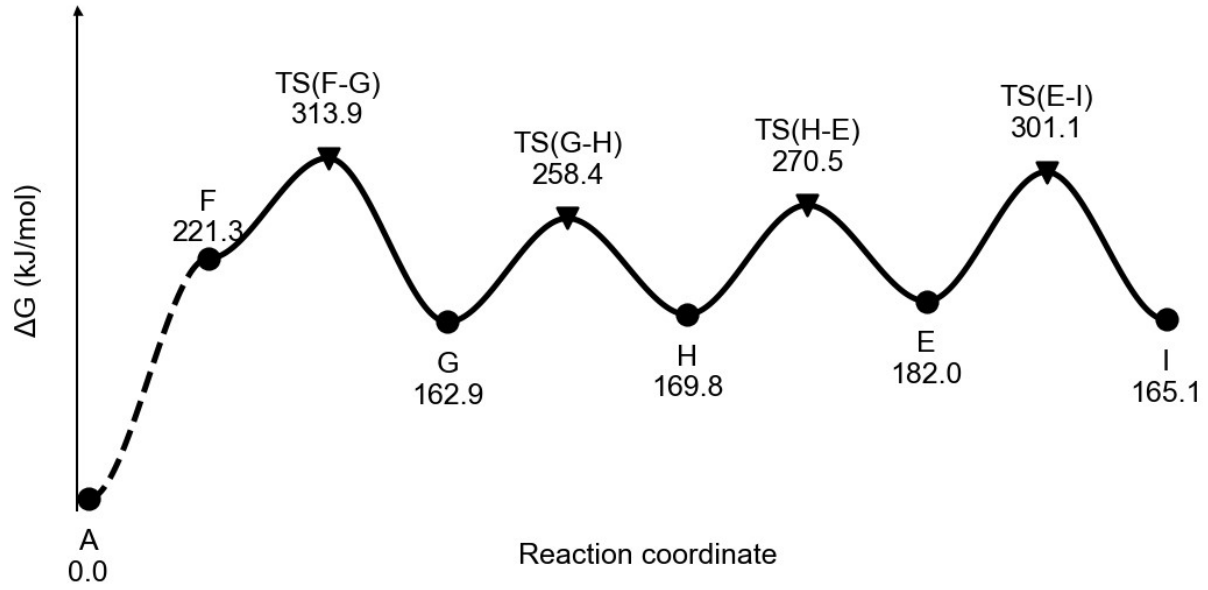

Fig. S104. Reaction profile diagram for the depolymerization of tetrameric PS, via states **F** through **I**.

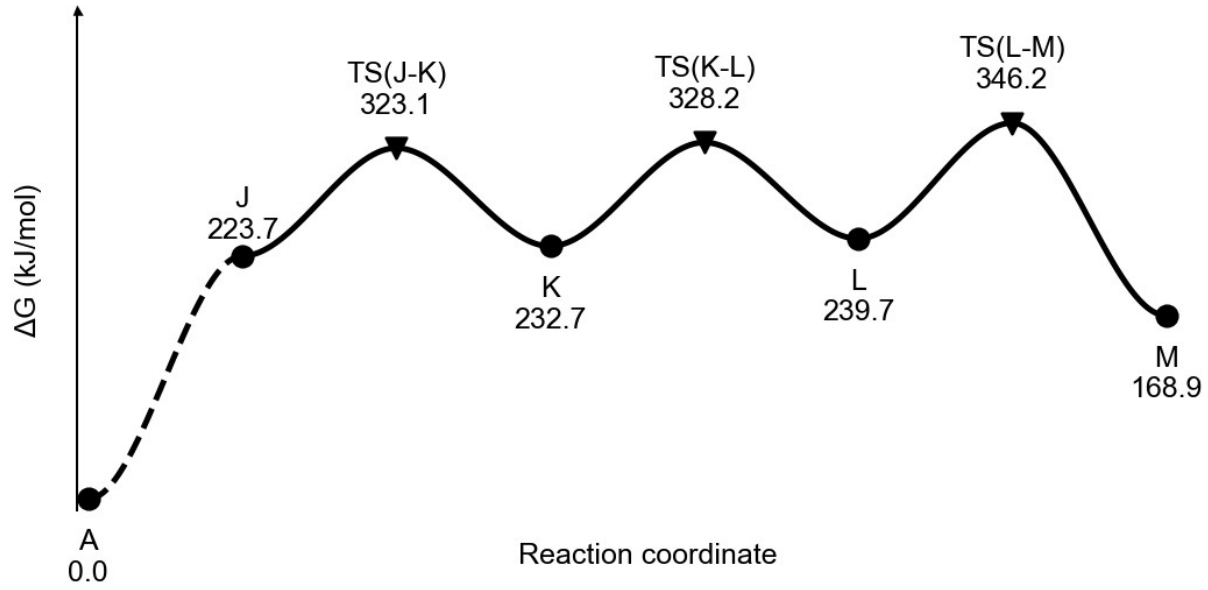

For PS-SCF_3 (**N**), homolytic fission occurs at the weaker C-S bond instead of the main carbon chain to form R_{tb} and the SCF_3 radical (**O**). The SCF_3 radical abstracts a proton from another unfunctionalized polystyrene chain to form another R_{tb} (**P**). In order to align the product states of

this mechanism with that of either **I** or **M** for PS, we further depolymerize R_{tb} to form an alkene and R_{sb} (**Q**), with two iterations of depolymerization for the trimeric R_{sb} (**R**, **S**). This pathway is shown in **Fig. S101** for 1-functionalized PS-SCF_3 (PS-1-SCF_3). A similar pathway involving 2-functionalized PS-SCF_3 (PS-2-SCF_3) shows a similar energetic profile compared to PS-1-SCF_3 (**Fig. S101**), with slightly lower barriers as one less styrene monomer is formed through this path. These processes are significantly lower in energy compared to PS, with a maximum barrier at +256.5 kJ/mol.

Fig. S105. Reaction profile diagram for the depolymerization of tetrameric PS-1-SCF_3, via states **N** through **S**.

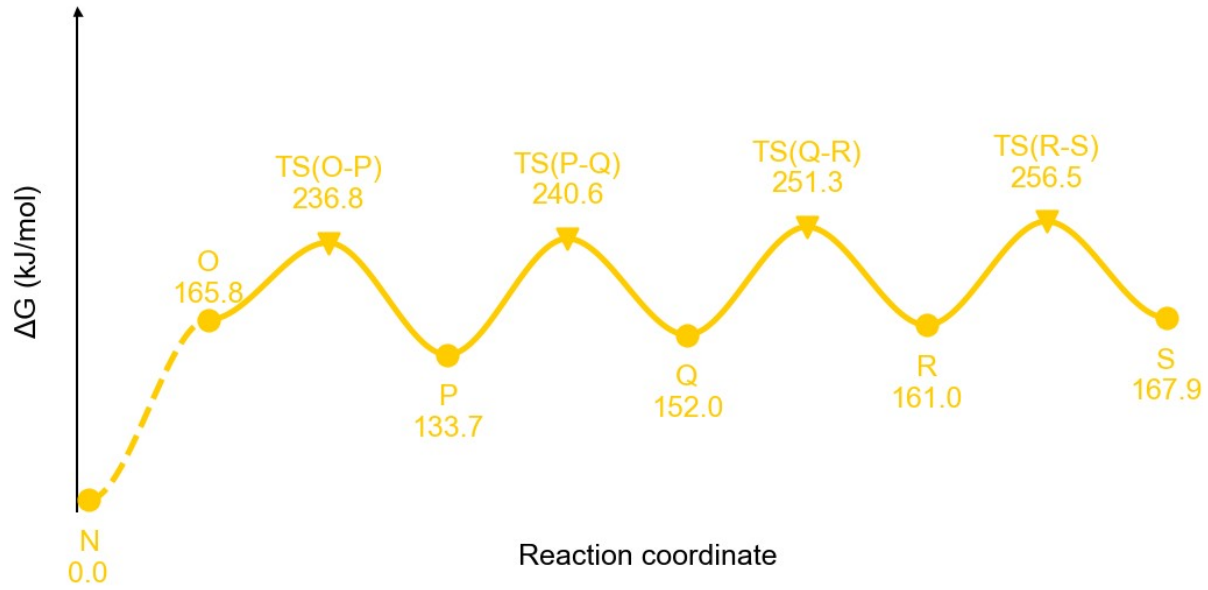

Fig. S106. Reaction profile diagram for the depolymerization of tetrameric PS-2-SCF_3, via states **T** through **X**.

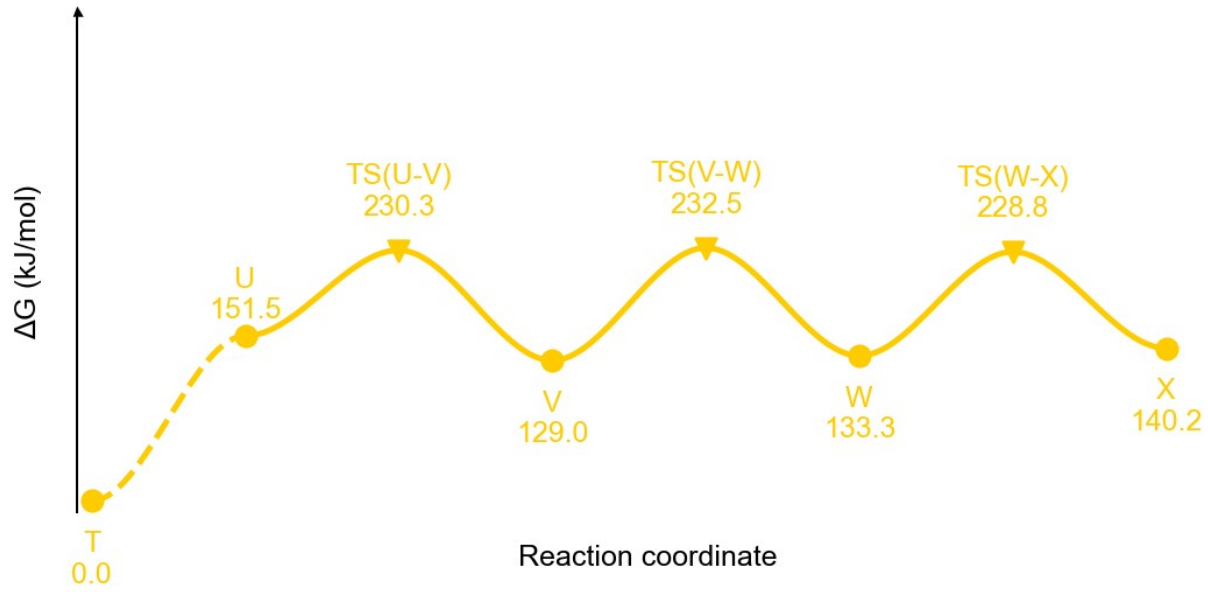

Fig. S107. Reaction profile diagram comparing the depolymerization of tetrameric PS and tetrameric PS-1-SCF_3.

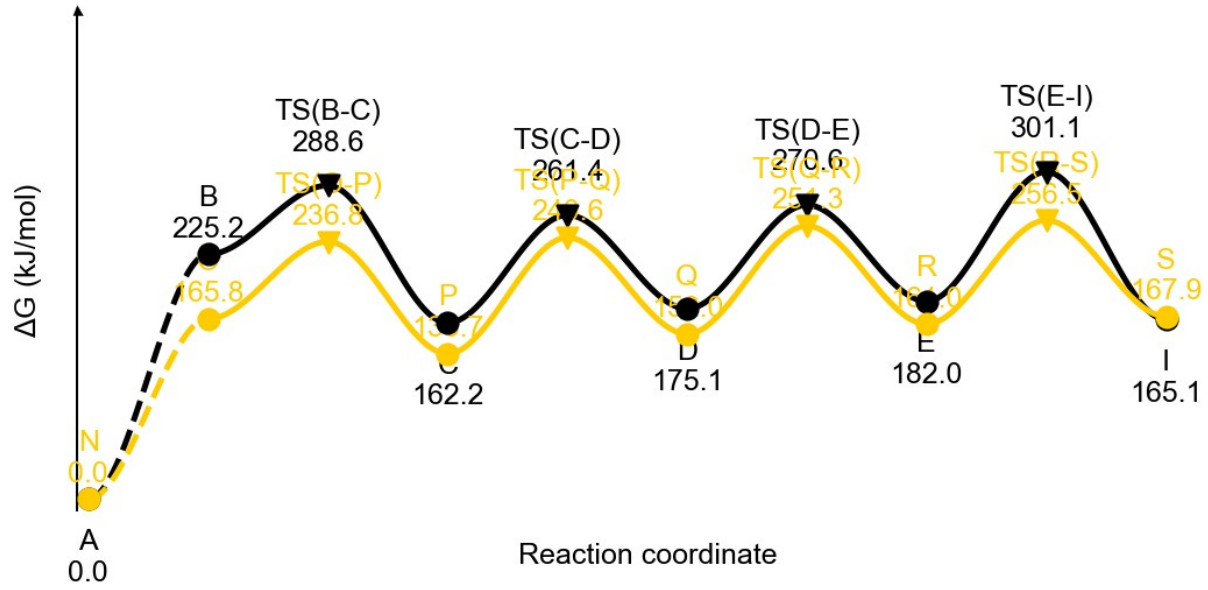

Flynn-Ozawa-Wall Analysis

The ASTM E1641 standard and ICTAC recommendations were followed closely to perform the Flynn-Ozawa-Wall method.[41,42] First, we performed a series of dynamic TGA experiments with different heating rates of 1°C/min, 2°C/min, 5°C/min, and 10°C/min on both the PS-10K and PS-10K-SCF_3 samples. By extracting the temperatures between 10-20% conversion, we can plot the heating rate (β) against the temperature (1/T). Using the plot (**Fig. 4c, e**) and equation below, we can estimate the apparent activation energy (E_a) at a specific conversion where R = 8.314J/mol*K and b = empirical value determined by following ASTM E1641.

$$\log(\beta) = constant - b\frac{E_a}{RT}$$

While the average apparent activation energy between 10-20% conversion for PS-10K is 308kJ/mol, the literature value for PS usually reports between 173kJ/mol to 200kJ/mol.[43–45] We attribute this difference to the fully head-to-tail topology of PS provided by Tosoh which is anionically polymerized and creates less weak links in the backbone compared to the samples reported in literature. Nevertheless, while the experimental mechanism is expected to be more complicated than our proposed DFT mechanism, our value from the Flynn-Ozawa-Wall analysis of 308kJ/mol corroborates well with the DFT calculated values of 301kJ/mol on a tetrameric model system.

Table S9. Flynn-Ozawa-Wall Analysis results and empirical parameters for PS-10K and PS-10K-SCF3.

Experiment Label	Conversion (%)	Apparent Activation Energy (E_a, kJ/mol)	R^2	E/RT	b
PS-10K	10	328.959	0.921004	63.5289452	0.4487
PS-10K	11	325.122218	0.92925238	62.5695005	0.4487
PS-10K	12	317.851786	0.93856815	60.9609448	0.4487
PS-10K	13	313.882223	0.94976776	60.0165665	0.4487
PS-10K	14	309.565523	0.95473821	59.0228183	0.44889544
PS-10K	15	303.779533	0.96114333	57.7635336	0.44919459
PS-10K	16	299.365274	0.96689418	56.7797406	0.44956608
PS-10K	17	294.292314	0.97040061	55.6833283	0.44986333
PS-10K	18	290.206236	0.97241649	54.7917587	0.45006247
PS-10K	19	287.249439	0.97698008	54.1170345	0.45026489
PS-10K	20	283.146559	0.97937301	53.2379138	0.45052863
PS-10K-SCF3	10	311.066526	0.99728457	59.8765091	0.4487247
PS-10K-SCF3	11	307.756227	0.99792944	59.0706305	0.44888587
PS-10K-SCF3	12	303.529698	0.99763767	58.0896797	0.44908206
PS-10K-SCF3	13	298.806519	0.99838894	57.0414238	0.44948343
PS-10K-SCF3	14	294.916773	0.99775564	56.1674302	0.44974977
PS-10K-SCF3	15	291.655239	0.99844702	55.4237611	0.44991525
PS-10K-SCF3	16	288.602323	0.99837521	54.7333309	0.45008
PS-10K-SCF3	17	286.722407	0.99826416	54.2718026	0.45021846
PS-10K-SCF3	18	283.747052	0.99820229	53.6072479	0.45041783
PS-10K-SCF3	19	281.501093	0.99804802	53.0891018	0.45057327

PS-10K-SCF3	20	280.068273	0.99794418	52.7290025	0.4506542

Pyrolysis Experimental Results

styrene: ^{1}H NMR (400 MHz, DMSO) δ 7.50 – 7.44 (m, 2H), 7.41 – 7.32 (m, 2H), 7.30 – 7.23 (m, 1H), 6.73 (dd, J = 17.7, 10.9 Hz, 1H), 5.83 (dd, J = 17.7, 1.0 Hz, 1H), 5.26 (dd, J = 10.9, 1.0 Hz, 1H).

1,3,5-trimethoxybenzene: ^{1}H NMR (400 MHz, DMSO) 6.09 (s, 3H), 3.70 (s, 9H).

Fig. S108. ^{1}H NMR of Depolymerized PS-110K (Tosoh) at 300°C for 20hrs in DMSO-d_6 with internal standard 1,3,5-trimethoxybenzene (reaction vial, cannula, and collection vial). Note: tentative assignments in grey.

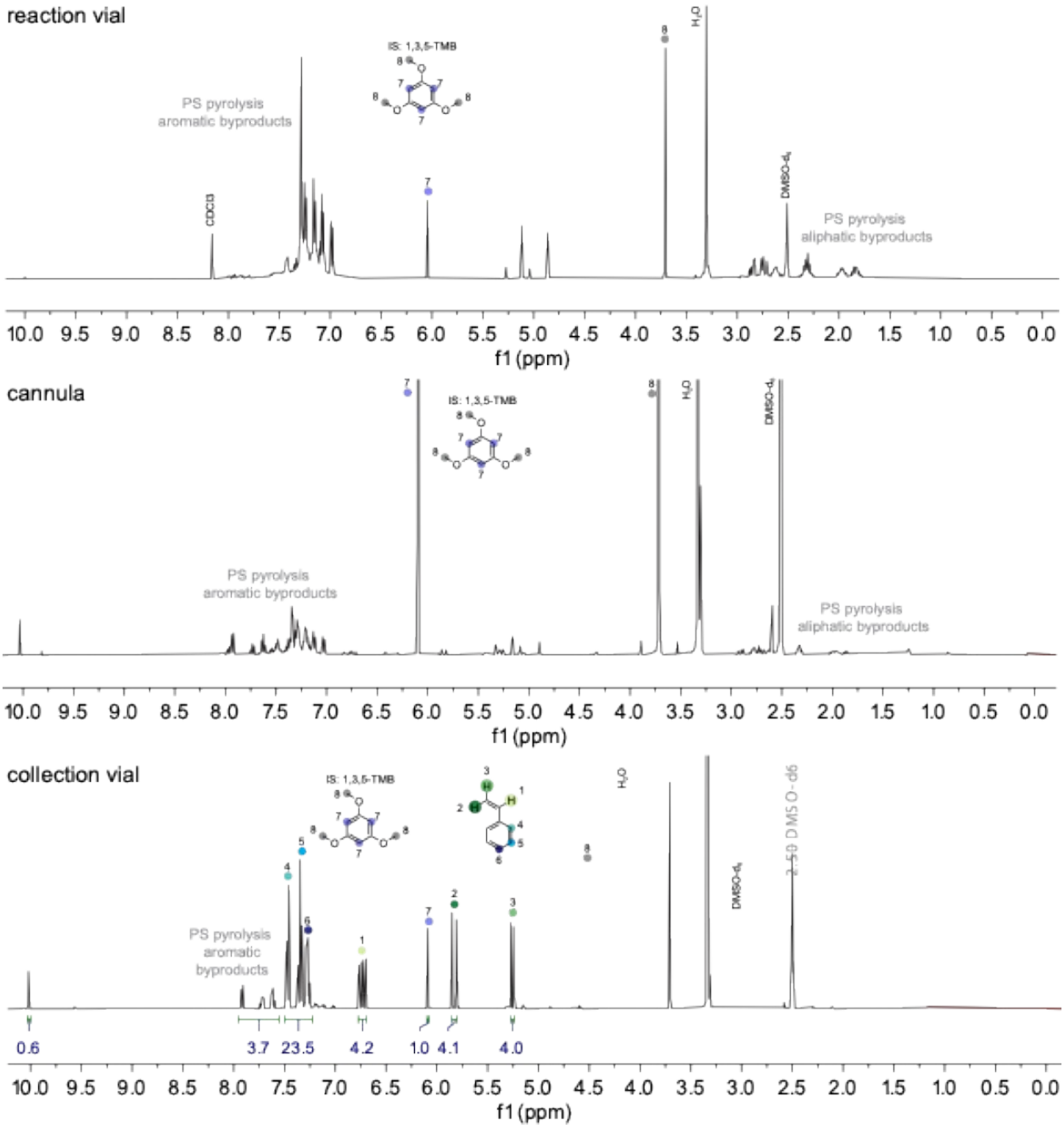

Fig. S109. ^{1}H NMR of Depolymerized PS-Coffee-Lid at 300°C for 20hrs in DMSO-d_6 with internal standard 1,3,5-trimethoxybenzene (reaction vial, cannula, and collection vial). Note: tentative assignments in grey. $CDCl_3$ was added to reaction vial to dissolve leftover polymer.

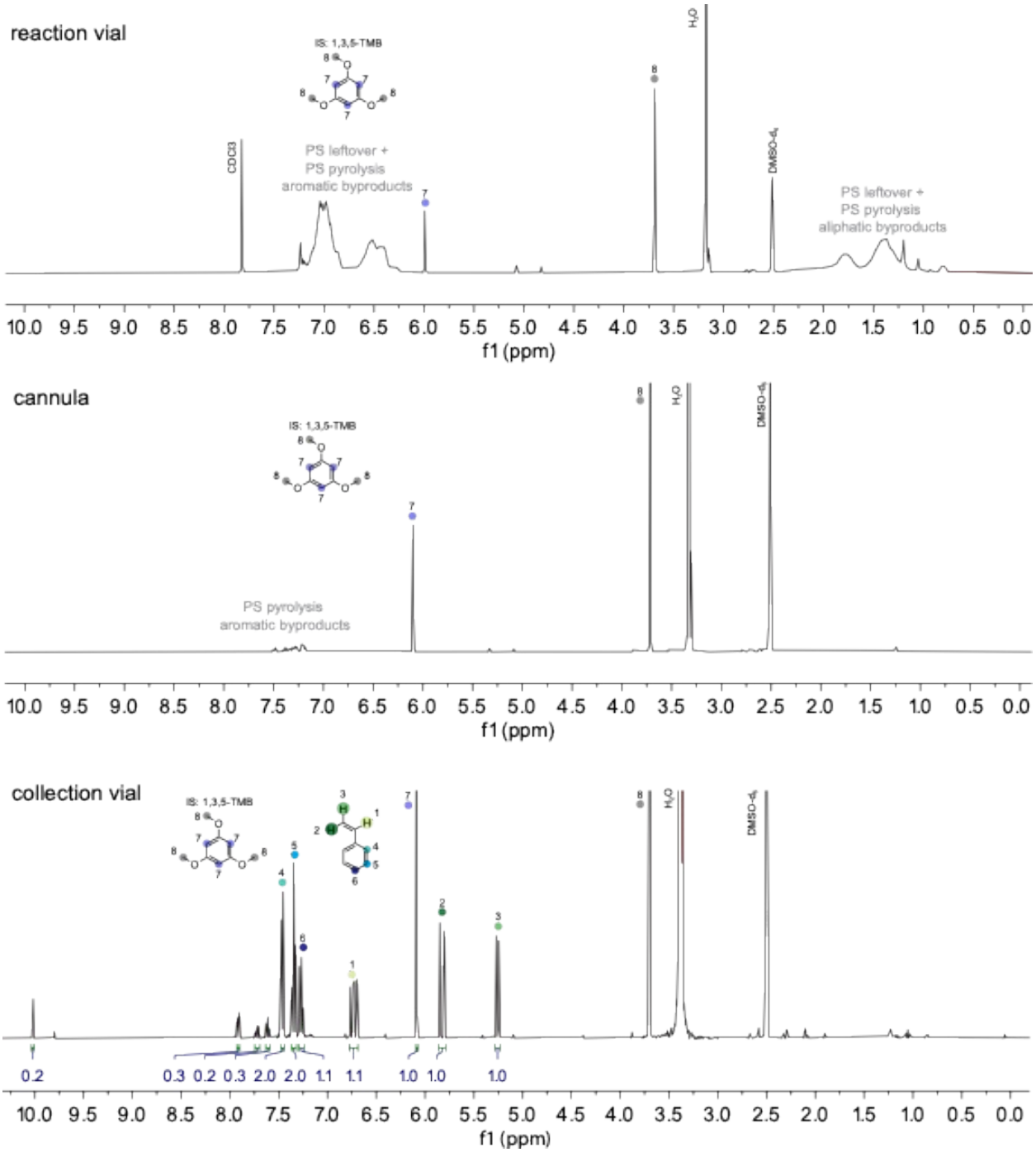

Fig. S110. ^{1}H NMR of Depolymerized PS-Container at 300°C for 20hrs in DMSO-d_6 with internal standard 1,3,5-trimethoxybenzene (reaction vial, cannula, and collection vial). Note: tentative assignments in grey.

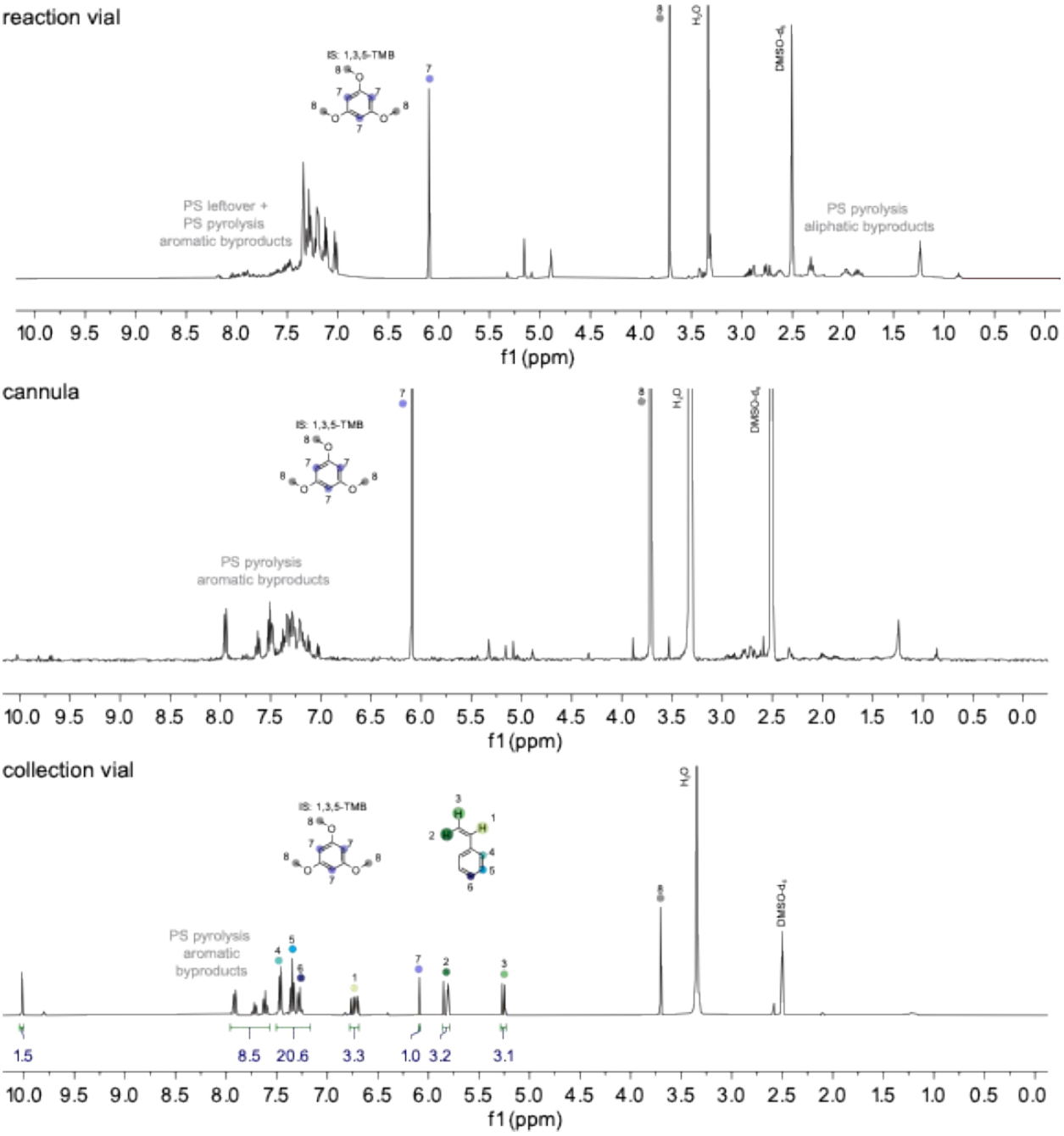

Fig. S111. ^{1}H NMR of Depolymerized PS-Red-Solo-Cup at 300°C for 20hrs in DMSO-d_6 with internal standard 1,3,5-trimethoxybenzene (reaction vial, cannula, and collection vial). Note: tentative assignments in grey. $CDCl_3$ was added to reaction vial to dissolve leftover polymer.

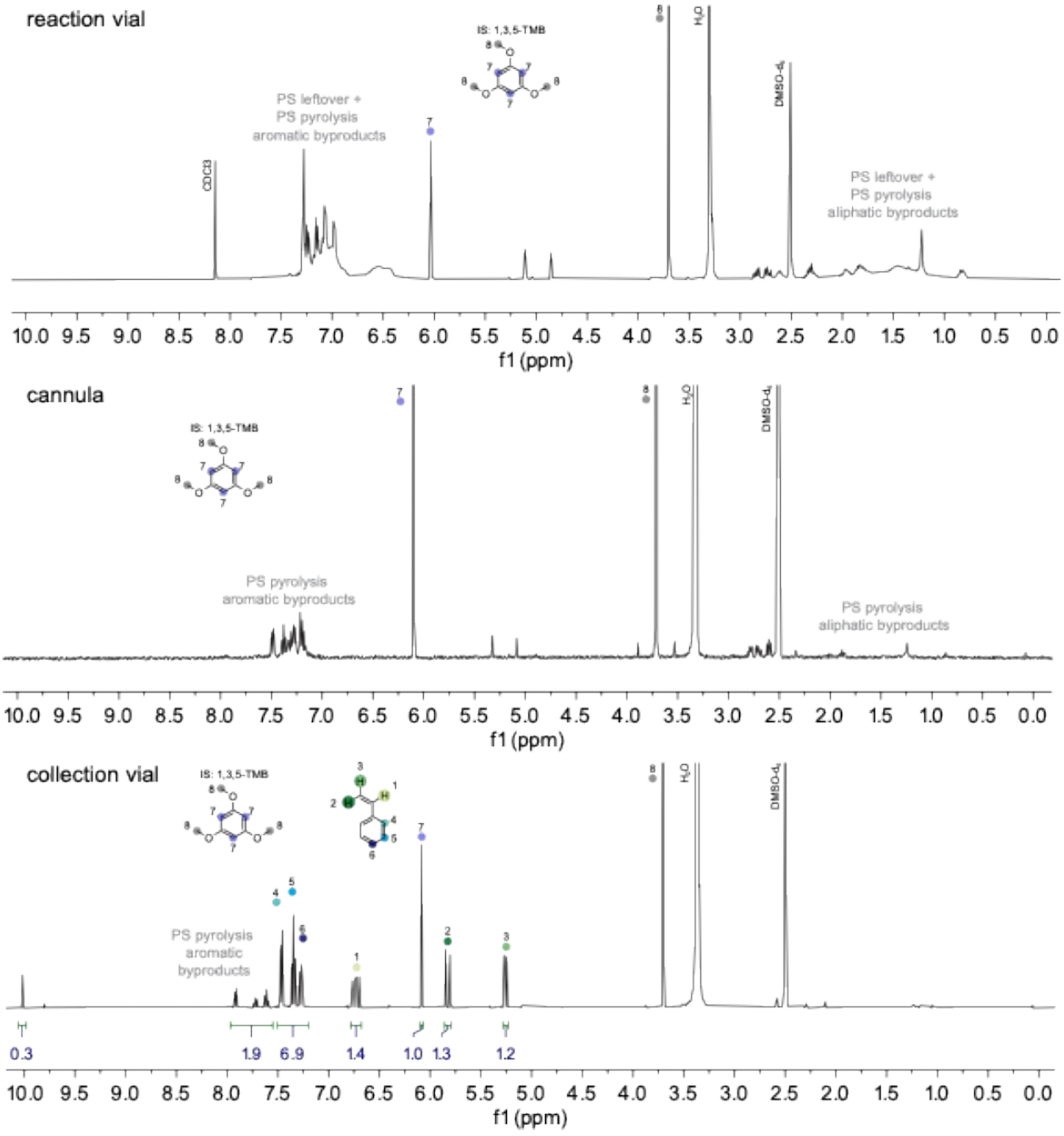

Fig. S112. ^{1}H NMR of Depolymerized PS-110K-SCF_3 (Tosoh) at 300°C for 20hrs in DMSO-d_6 with internal standard 1,3,5-trimethoxybenzene (reaction vial, cannula, and collection vial). Note: tentative assignments in grey. $CDCl_3$ was added to reaction vial to dissolve leftover polymer.

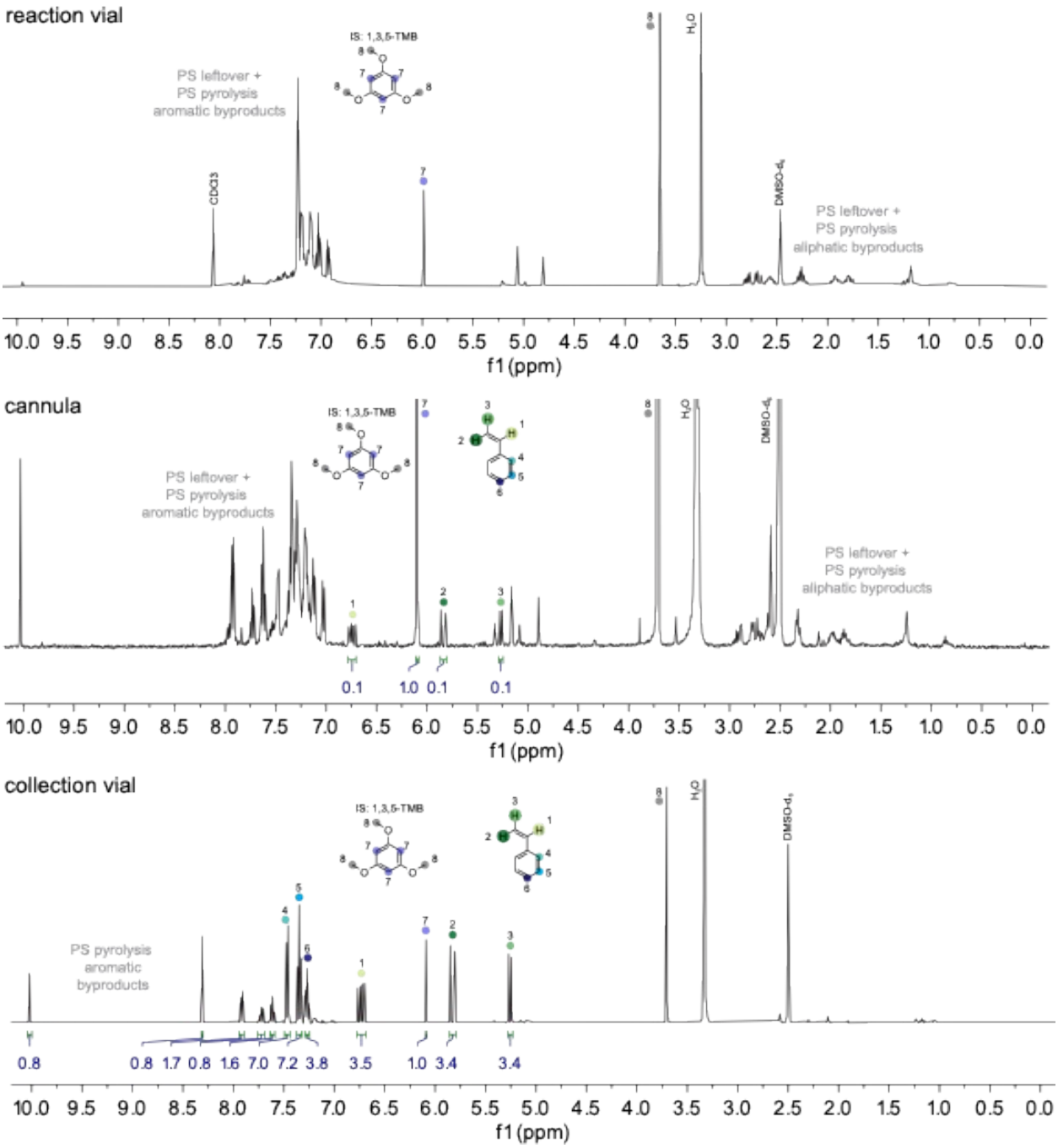

Fig. S113. ^{19}F NMR of Depolymerized PS-110K-SCF_3 (Tosoh) at 300°C for 20hrs in DMSO-d_6 with internal standard 1,3,5-trimethoxybenzene (reaction vial, cannula, and collection vial).

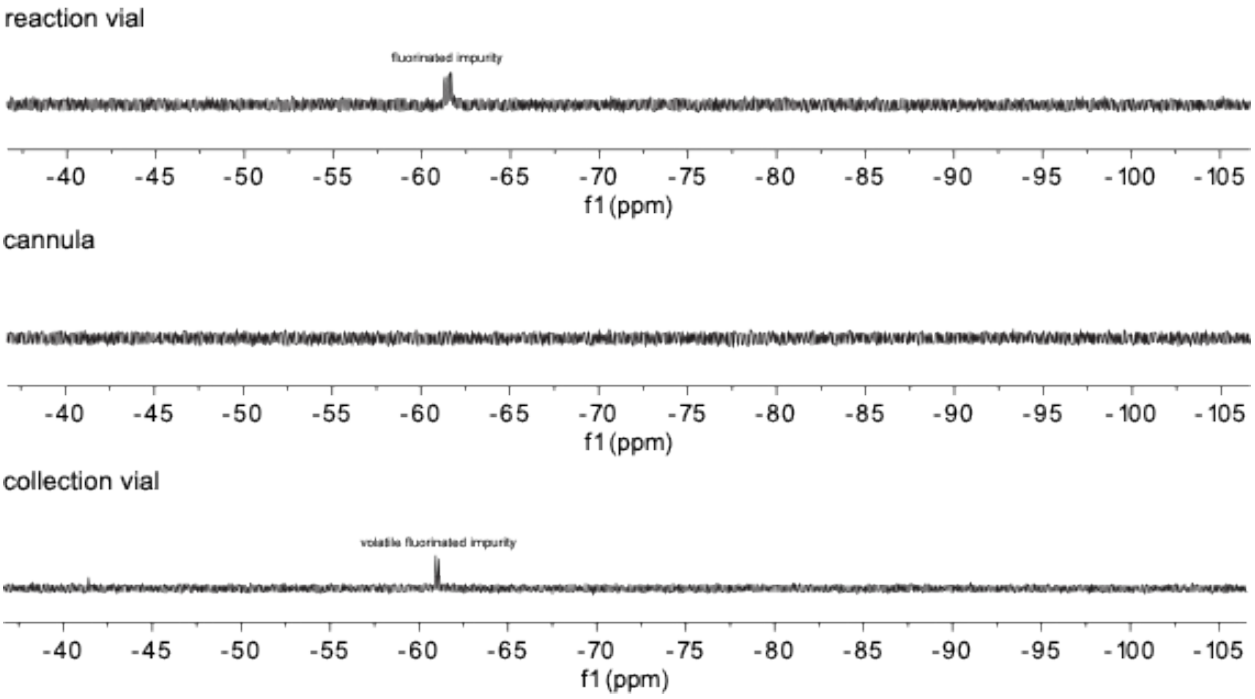

Fig. S114. ^{1}H NMR of Depolymerized PS-Coffee-Lid-SCF_3 at 300°C for 20hrs in DMSO-d_6 with internal standard 1,3,5-trimethoxybenzene (reaction vial, cannula, and collection vial). Note: tentative assignments in grey. $CDCl_3$ was added to reaction vial to dissolve leftover polymer.

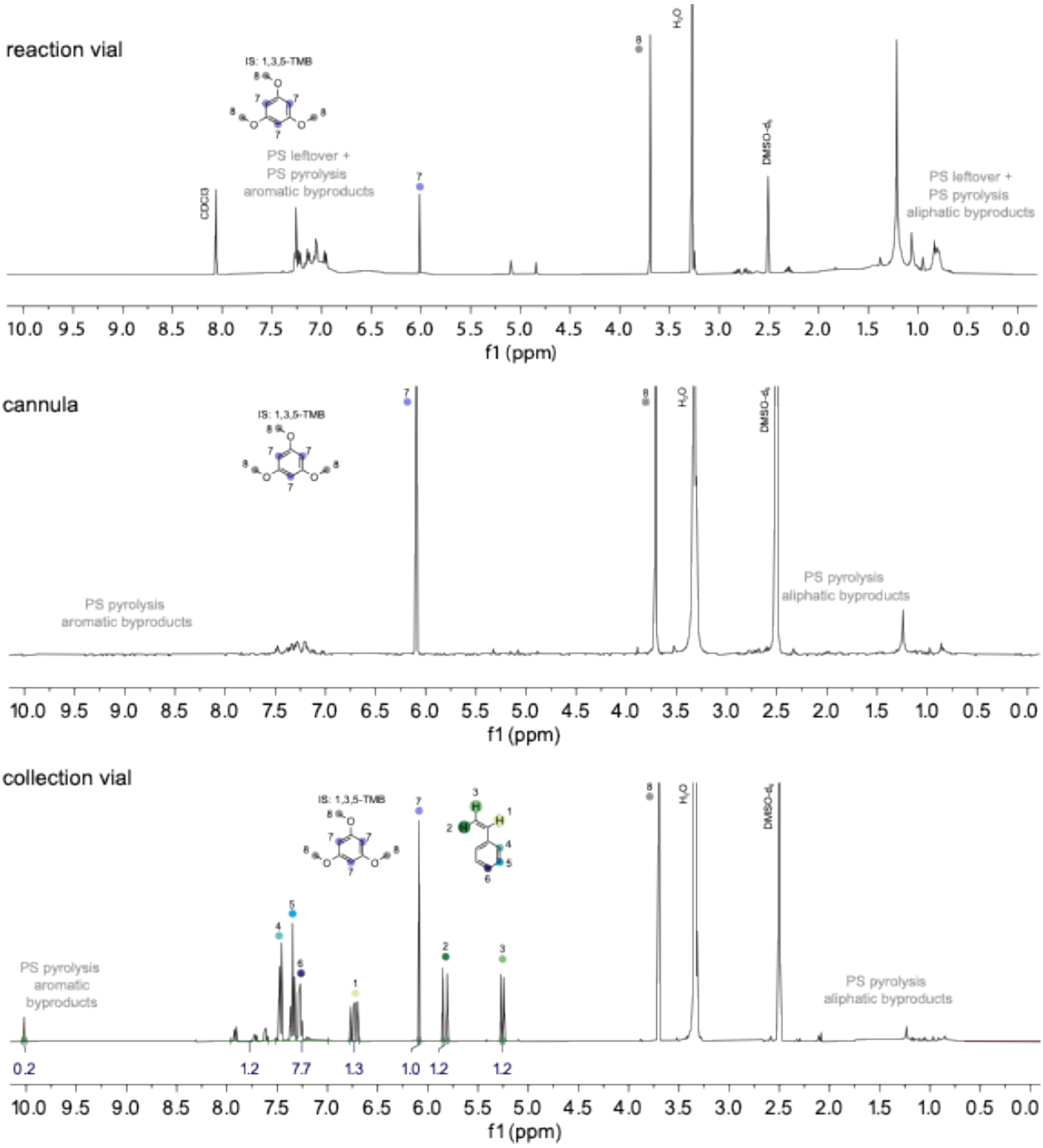

Fig. S115. ^{19}F NMR of Depolymerized PS-Coffee-Lid-SCF_3 at 300°C for 20hrs in DMSO-d_6 with internal standard 1,3,5-trimethoxybenzene (reaction vial, cannula, and collection vial).

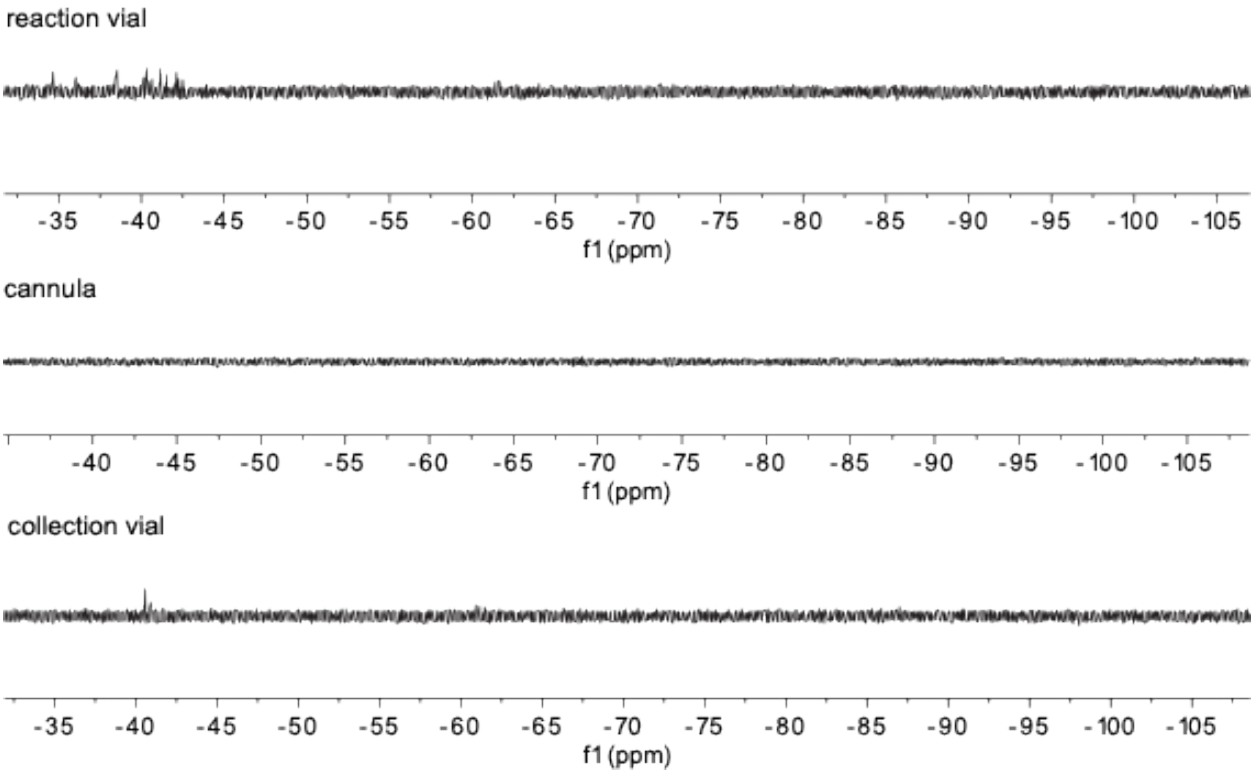

Fig. S116. ^{1}H NMR of Depolymerized PS-Container-SCF_3 at 300°C for 20hrs in DMSO-d_6 with internal standard 1,3,5-trimethoxybenzene (reaction vial, cannula, and collection vial). Note: tentative assignments in grey. $CDCl_3$ was added to reaction vial to dissolve leftover polymer.

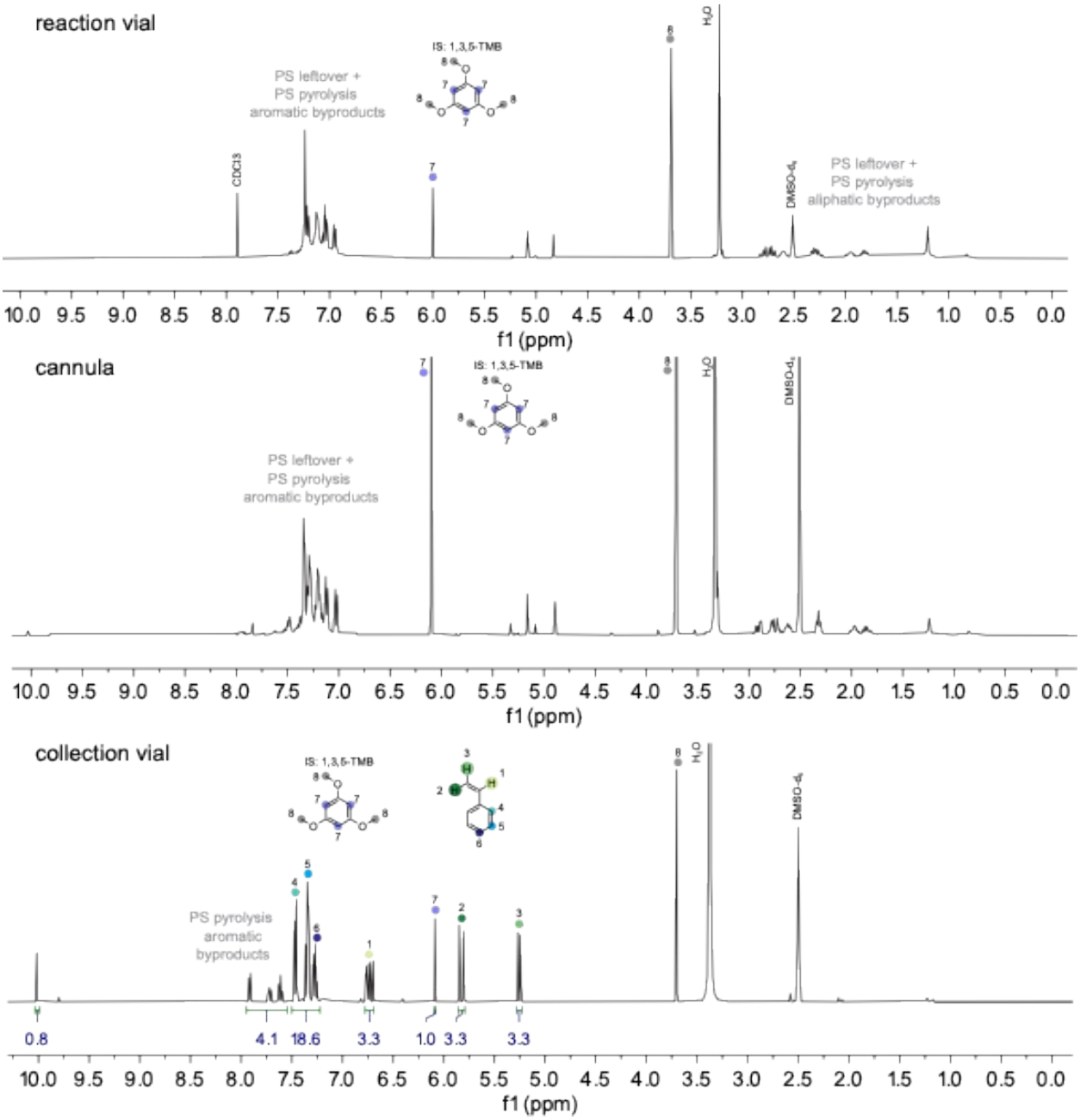

Fig. S117. ^{19}F NMR of Depolymerized PS-Container-SCF_3 at 300°C for 20hrs in DMSO-d_6 with internal standard 1,3,5-trimethoxybenzene (reaction vial, cannula, and collection vial). Note: tentative assignments in grey.

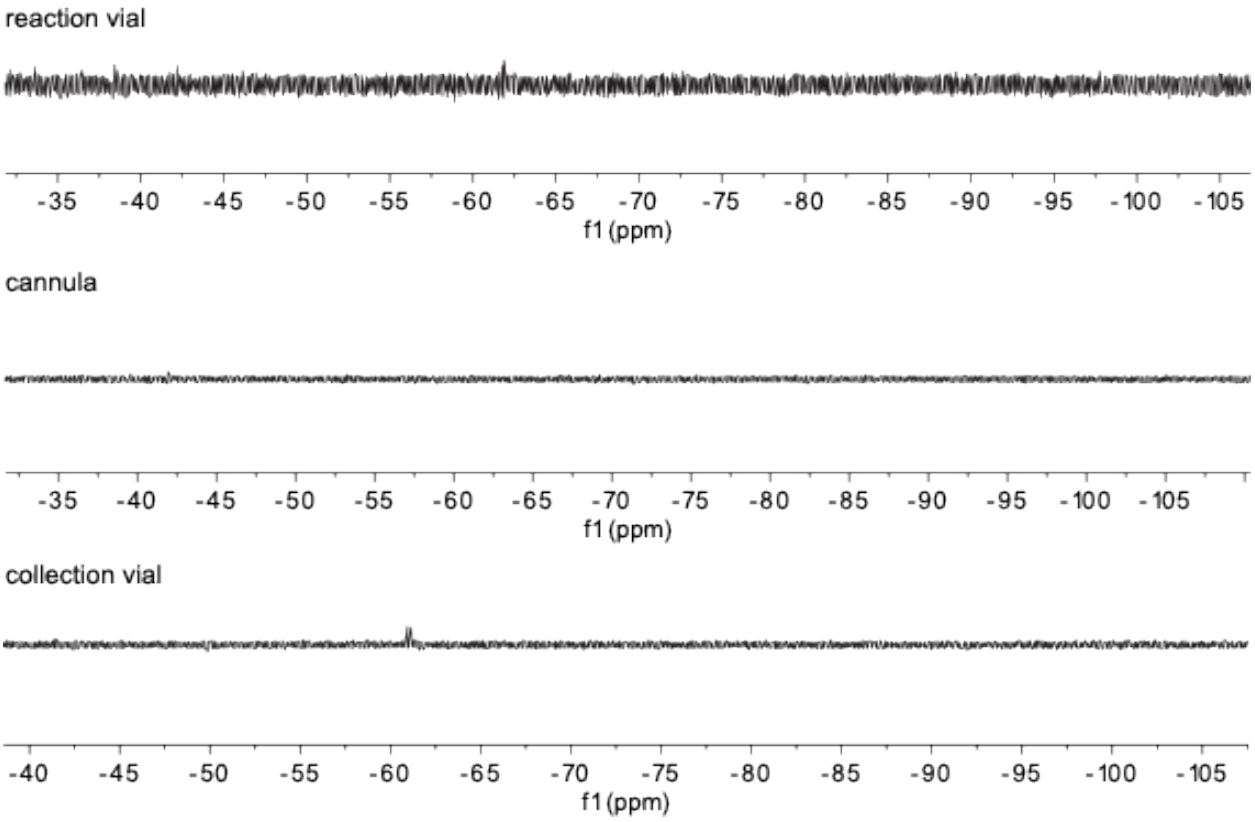

Fig. S118. ^{1}H NMR of Depolymerized PS-Red-Solo-Cup-SCF_3 at 300°C for 20hrs in DMSO-d_6 with internal standard 1,3,5-trimethoxybenzene (reaction vial, cannula, and collection vial). Note: tentative assignments in grey. $CDCl_3$ was added to reaction vial to dissolve leftover polymer.

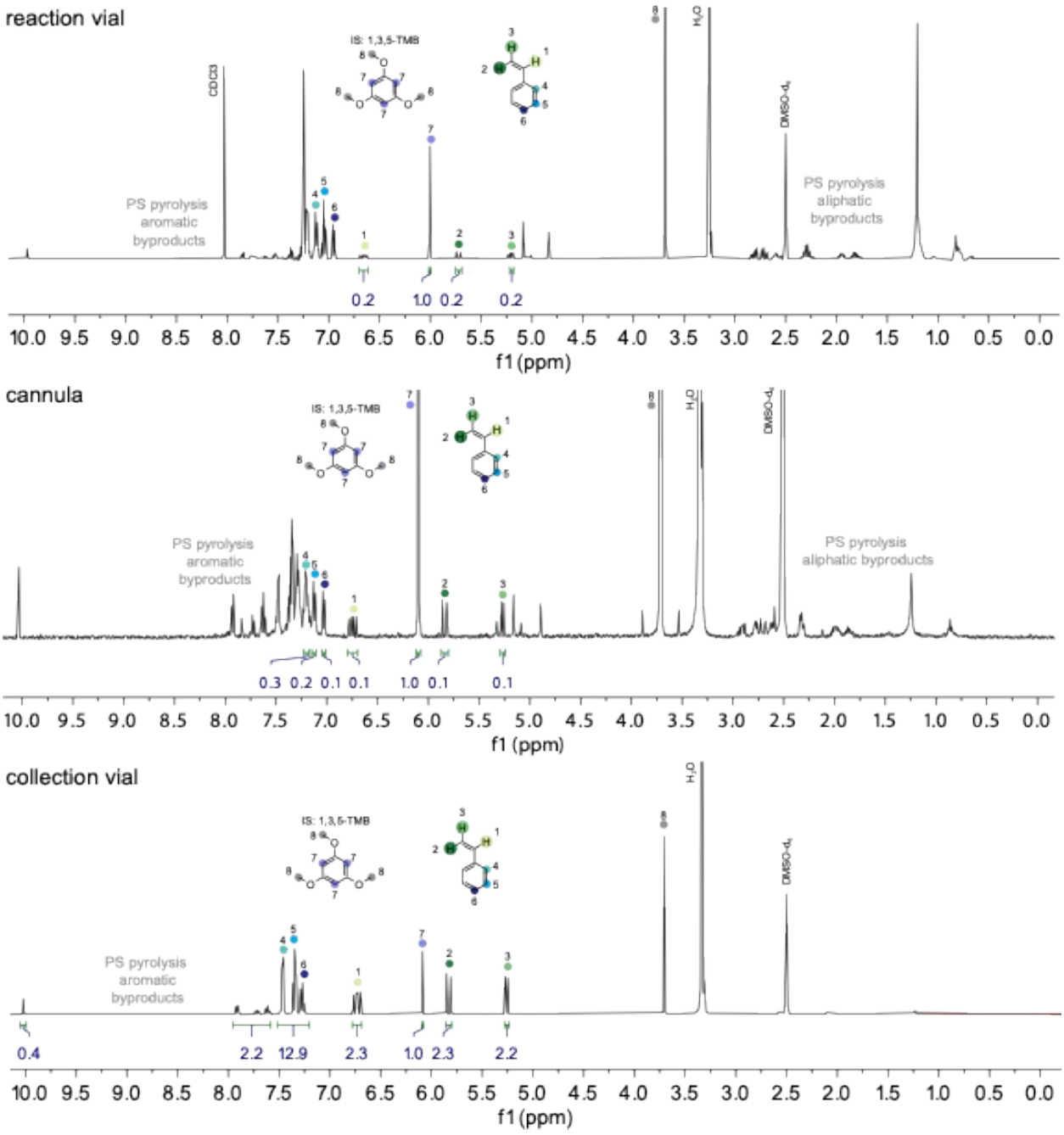

Fig. S119. ^{19}F NMR of Depolymerized PS-Red-Solo-Cup-SCF_3 at 300°C for 20hrs in DMSO-d_6 with internal standard 1,3,5-trimethoxybenzene (reaction vial, cannula, and collection vial). Note: tentative assignments in grey.

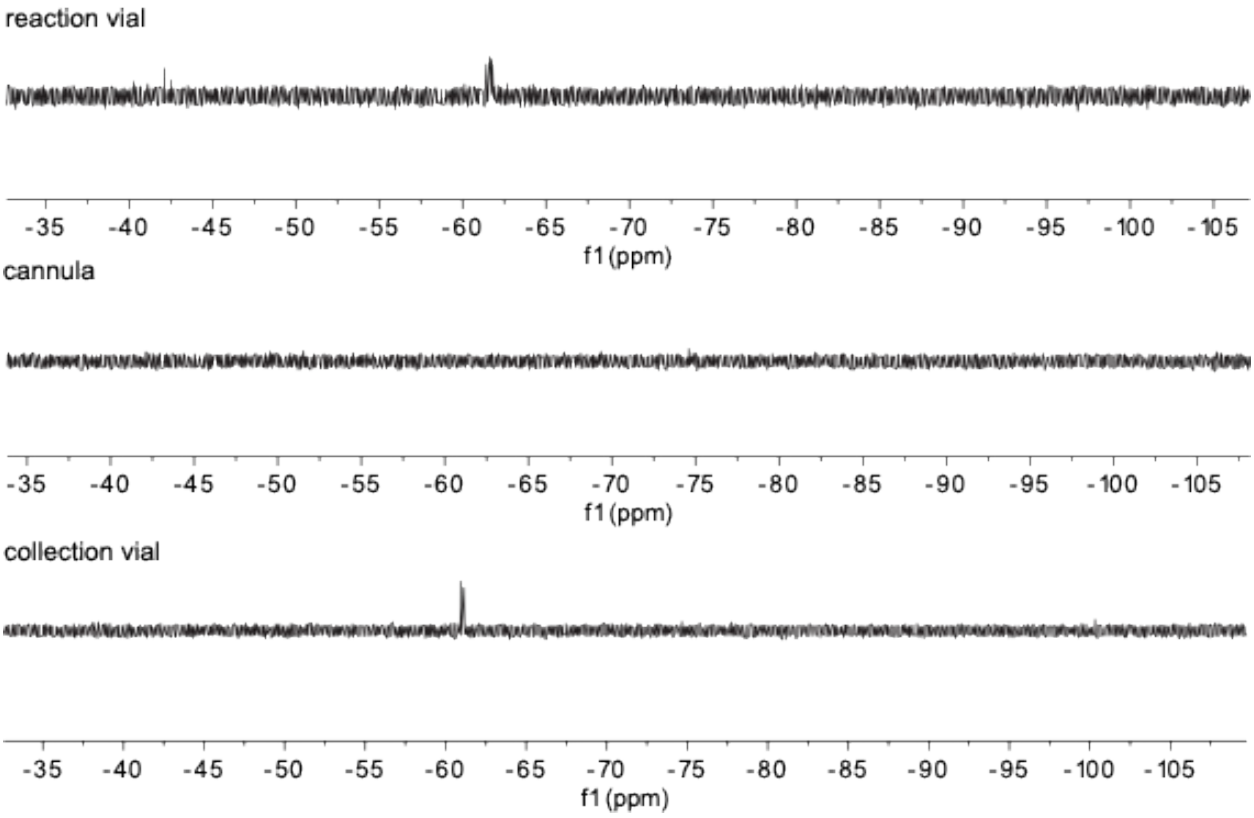

References

(1) Grimme, S. Exploration of Chemical Compound, Conformer, and Reaction Space with Meta-Dynamics Simulations Based on Tight-Binding Quantum Chemical Calculations. *J. Chem. Theory Comput.* **2019**, *15* (5), 2847–2862. https://doi.org/10.1021/acs.jctc.9b00143.

(2) Pracht, P.; Bohle, F.; Grimme, S. Automated Exploration of the Low-Energy Chemical Space with Fast Quantum Chemical Methods. *Phys. Chem. Chem. Phys.* **2020**, *22* (14), 7169–7192. https://doi.org/10.1039/C9CP06869D.

(3) Pracht, P.; Grimme, S.; Bannwarth, C.; Bohle, F.; Ehlert, S.; Feldmann, G.; Gorges, J.; Müller, M.; Neudecker, T.; Plett, C.; Spicher, S.; Steinbach, P.; Wesołowski, P. A.; Zeller, F. CREST—A Program for the Exploration of Low-Energy Molecular Chemical Space. *J. Chem. Phys.* **2024**, *160* (11), 114110. https://doi.org/10.1063/5.0197592.

(4) Bannwarth, C.; Ehlert, S.; Grimme, S. GFN2-xTB—An Accurate and Broadly Parametrized Self-Consistent Tight-Binding Quantum Chemical Method with Multipole Electrostatics and Density-Dependent Dispersion Contributions. *J. Chem. Theory Comput.* **2019**, *15* (3), 1652–1671. https://doi.org/10.1021/acs.jctc.8b01176.

(5) Ehlert, S.; Stahn, M.; Spicher, S.; Grimme, S. Robust and Efficient Implicit Solvation Model for Fast Semiempirical Methods. *J. Chem. Theory Comput.* **2021**, *17* (7), 4250–4261. https://doi.org/10.1021/acs.jctc.1c00471.

(6) Adamo, C.; Barone, V. Toward Reliable Density Functional Methods without Adjustable Parameters: The PBE0 Model. *J. Chem. Phys.* **1999**, *110* (13), 6158–6170. https://doi.org/10.1063/1.478522.
(7) Ernzerhof, M.; Scuseria, G. E. Assessment of the Perdew–Burke–Ernzerhof Exchange-Correlation Functional. *J. Chem. Phys.* **1999**, *110* (11), 5029–5036. https://doi.org/10.1063/1.478401.
(8) Caldeweyher, E.; Bannwarth, C.; Grimme, S. Extension of the D3 Dispersion Coefficient Model. *J. Chem. Phys.* **2017**, *147* (3), 034112. https://doi.org/10.1063/1.4993215.
(9) Caldeweyher, E.; Ehlert, S.; Hansen, A.; Neugebauer, H.; Spicher, S.; Bannwarth, C.; Grimme, S. A Generally Applicable Atomic-Charge Dependent London Dispersion Correction. *J. Chem. Phys.* **2019**, *150* (15), 154122. https://doi.org/10.1063/1.5090222.
(10) Caldeweyher, E.; Mewes, J.-M.; Ehlert, S.; Grimme, S. Extension and Evaluation of the D4 London-Dispersion Model for Periodic Systems. *Phys. Chem. Chem. Phys.* **2020**, *22* (16), 8499–8512. https://doi.org/10.1039/D0CP00502A.
(11) Weigend, F.; Ahlrichs, R. Balanced Basis Sets of Split Valence, Triple Zeta Valence and Quadruple Zeta Valence Quality for H to Rn: Design and Assessment of Accuracy. *Phys. Chem. Chem. Phys.* **2005**, *7* (18), 3297–3305. https://doi.org/10.1039/B508541A.
(12) Garcia-Ratés, M.; Neese, F. Effect of the Solute Cavity on the Solvation Energy and Its Derivatives within the Framework of the Gaussian Charge Scheme. *Journal of Computational Chemistry* **2020**, *41* (9), 922–939. https://doi.org/10.1002/jcc.26139.
(13) Garcia-Ratés, M.; Becker, U.; Neese, F. Implicit Solvation in Domain Based Pair Natural Orbital Coupled Cluster (DLPNO-CCSD) Theory. *Journal of Computational Chemistry* **2021**, *42* (27), 1959–1973. https://doi.org/10.1002/jcc.26726.
(14) Guo, Y.; Riplinger, C.; Becker, U.; Liakos, D. G.; Minenkov, Y.; Cavallo, L.; Neese, F. Communication: An Improved Linear Scaling Perturbative Triples Correction for the Domain Based Local Pair-Natural Orbital Based Singles and Doubles Coupled Cluster Method [DLPNO-CCSD(T)]. *J. Chem. Phys.* **2018**, *148* (1), 011101. https://doi.org/10.1063/1.5011798.
(15) Bistoni, G.; Riplinger, C.; Minenkov, Y.; Cavallo, L.; Auer, A. A.; Neese, F. Treating Subvalence Correlation Effects in Domain Based Pair Natural Orbital Coupled Cluster Calculations: An Out-of-the-Box Approach. *J. Chem. Theory Comput.* **2017**, *13* (7), 3220–3227. https://doi.org/10.1021/acs.jctc.7b00352.
(16) Riplinger, C.; Pinski, P.; Becker, U.; Valeev, E. F.; Neese, F. Sparse Maps—A Systematic Infrastructure for Reduced-Scaling Electronic Structure Methods. II. Linear Scaling Domain Based Pair Natural Orbital Coupled Cluster Theory. *J. Chem. Phys.* **2016**, *144* (2), 024109. https://doi.org/10.1063/1.4939030.
(17) Riplinger, C.; Sandhoefer, B.; Hansen, A.; Neese, F. Natural Triple Excitations in Local Coupled Cluster Calculations with Pair Natural Orbitals. *J. Chem. Phys.* **2013**, *139* (13), 134101. https://doi.org/10.1063/1.4821834.
(18) Riplinger, C.; Neese, F. An Efficient and near Linear Scaling Pair Natural Orbital Based Local Coupled Cluster Method. *J. Chem. Phys.* **2013**, *138* (3), 034106. https://doi.org/10.1063/1.4773581.
(19) Neese, F.; Wennmohs, F.; Hansen, A. Efficient and Accurate Local Approximations to Coupled-Electron Pair Approaches: An Attempt to Revive the Pair Natural Orbital Method. *J. Chem. Phys.* **2009**, *130* (11), 114108. https://doi.org/10.1063/1.3086717.
(20) Neese, F.; Hansen, A.; Liakos, D. G. Efficient and Accurate Approximations to the Local Coupled Cluster Singles Doubles Method Using a Truncated Pair Natural Orbital Basis. *J. Chem. Phys.* **2009**, *131* (6), 064103. https://doi.org/10.1063/1.3173827.
(21) Neese, F. Software Update: The ORCA Program System—Version 5.0. *WIREs Computational Molecular Science* **2022**, *12* (5), e1606. https://doi.org/10.1002/wcms.1606.

(22) Neese, F. An Improvement of the Resolution of the Identity Approximation for the Formation of the Coulomb Matrix. *Journal of Computational Chemistry* **2003**, *24* (14), 1740–1747. https://doi.org/10.1002/jcc.10318.
(23) Garcia-Ratés, M.; Neese, F. Efficient Implementation of the Analytical Second Derivatives of Hartree–Fock and Hybrid DFT Energies within the Framework of the Conductor-like Polarizable Continuum Model. *Journal of Computational Chemistry* **2019**, *40* (20), 1816–1828. https://doi.org/10.1002/jcc.25833.
(24) Bykov, D.; Petrenko, T.; Izsák, R.; Kossmann, S.; Becker, U.; Valeev, E.; Neese, F. Efficient Implementation of the Analytic Second Derivatives of Hartree–Fock and Hybrid DFT Energies: A Detailed Analysis of Different Approximations. *Molecular Physics* **2015**, *113* (13–14), 1961–1977. https://doi.org/10.1080/00268976.2015.1025114.
(25) Helmich-Paris, B.; de Souza, B.; Neese, F.; Izsák, R. An Improved Chain of Spheres for Exchange Algorithm. *J. Chem. Phys.* **2021**, *155* (10), 104109. https://doi.org/10.1063/5.0058766.
(26) Neese, F. The SHARK Integral Generation and Digestion System. *Journal of Computational Chemistry* **2023**, *44* (3), 381–396. https://doi.org/10.1002/jcc.26942.
(27) Neese, F.; Wennmohs, F.; Hansen, A.; Becker, U. Efficient, Approximate and Parallel Hartree–Fock and Hybrid DFT Calculations. A 'Chain-of-Spheres' Algorithm for the Hartree–Fock Exchange. *Chemical Physics* **2009**, *356* (1–3), 98–109. https://doi.org/10.1016/j.chemphys.2008.10.036.
(28) Harvey, J. N.; Himo, F.; Maseras, F.; Perrin, L. Scope and Challenge of Computational Methods for Studying Mechanism and Reactivity in Homogeneous Catalysis. *ACS Catal.* **2019**, *9* (8), 6803–6813. https://doi.org/10.1021/acscatal.9b01537.
(29) Xu, W.; Wang, W.; Liu, T.; Xie, J.; Zhu, C. Late-Stage Trifluoromethylthiolation of Benzylic C-H Bonds. *Nat Commun* **2019**, *10* (1), 4867. https://doi.org/10.1038/s41467-019-12844-9.
(30) *Facile Synthesis of Sequence‐Regulated Synthetic Polymers Using Orthogonal SuFEx and CuAAC Click Reactions - Yang - 2018 - Angewandte Chemie International Edition - Wiley Online Library*. https://onlinelibrary.wiley.com/doi/10.1002/anie.201811051 (accessed 2025-02-07).
(31) Hohorst, F. A.; Shreeve, J. M. Fluorine-19 Chemical Shifts in Nuclear Magnetic Resonance Spectra of Fluorosulfate-Containing Compounds. *Inorg. Chem.* **1966**, *5* (11), 2069–2069. https://doi.org/10.1021/ic50045a057.
(32) Sawaguchi, T.; Sasaki, D.; Takamura, A. On the Entanglement-Based Mechanism in Thermal Degradation of Vinyl Polymers. *Polymer Degradation and Stability* **2019**, *169*, 108990. https://doi.org/10.1016/j.polymdegradstab.2019.108990.
(33) Madorsky, S. L.; McIntyre, D.; O'Mara, J. H.; Straus, S. Thermal Degradation of Fractionated High and Low Molecular Weight Polystyrenes. *J. RES. NATL. BUR. STAN. SECT. A.* **1962**, *66A* (4), 307. https://doi.org/10.6028/jres.066A.029.
(34) Bryden, M. A.; Zysman-Colman, E. Organic Thermally Activated Delayed Fluorescence (TADF) Compounds Used in Photocatalysis. *Chem Soc Rev* **2021**, *50* (13), 7587–7680. https://doi.org/10.1039/d1cs00198a.
(35) Rasouli, S.; Moghbeli, M. R.; Nikkhah, S. J. A Comprehensive Molecular Dynamics Study of a Single Polystyrene Chain in a Good Solvent. *Current Applied Physics* **2018**, *18* (1), 68–78. https://doi.org/10.1016/j.cap.2017.10.010.
(36) Besford, Q. A.; Liu, M.; Beattie, J. K.; Gray-Weale, A. The Coalescence of Polystyrene in Correlated Binary Solvents. *Journal of Polymer Science Part B: Polymer Physics* **2016**, *54* (10), 948–955. https://doi.org/10.1002/polb.24003.
(37) Kruse, T. M.; Woo, O. S.; Wong, H.-W.; Khan, S. S.; Broadbelt, L. J. Mechanistic Modeling of Polymer Degradation: A Comprehensive Study of Polystyrene. *Macromolecules* **2002**, *35* (20), 7830–7844. https://doi.org/10.1021/ma020490a.

(38) Faravelli, T.; Pinciroli, M.; Pisano, F.; Bozzano, G.; Dente, M.; Ranzi, E. Thermal Degradation of Polystyrene. *Journal of Analytical and Applied Pyrolysis* **2001**, *60* (1), 103–121. https://doi.org/10.1016/S0165-2370(00)00159-5.
(39) Poutsma, M. L. Mechanistic Analysis and Thermochemical Kinetic Simulation of the Pathways for Volatile Product Formation from Pyrolysis of Polystyrene, Especially for the Dimer. *Polymer Degradation and Stability* **2006**, *91* (12), 2979–3009. https://doi.org/10.1016/j.polymdegradstab.2006.08.015.
(40) Kozuch, S.; Shaik, S. How to Conceptualize Catalytic Cycles? The Energetic Span Model. *Acc. Chem. Res.* **2011**, *44* (2), 101–110. https://doi.org/10.1021/ar1000956.
(41) E37 Committee. Test Method for Decomposition Kinetics by Thermogravimetry Using the Ozawa/Flynn/Wall Method. https://doi.org/10.1520/E1641-23.
(42) Vyazovkin, S.; Burnham, A. K.; Criado, J. M.; Pérez-Maqueda, L. A.; Popescu, C.; Sbirrazzuoli, N. ICTAC Kinetics Committee Recommendations for Performing Kinetic Computations on Thermal Analysis Data. *Thermochimica Acta* **2011**, *520* (1), 1–19. https://doi.org/10.1016/j.tca.2011.03.034.
(43) Şenocak, A.; Alkan, C.; Karadağ, A. Thermal Decomposition and a Kinetic Study of Poly(Para-Substituted Styrene)s. *AJAC* **2016**, *07* (03), 246–253. https://doi.org/10.4236/ajac.2016.73021.
(44) Blaine, R. L.; Hahn, B. K. Obtaining Kinetic Parameters by Modulated Thermogravimetry. *Journal of Thermal Analysis and Calorimetry* **1998**, *54* (2), 695–704. https://doi.org/10.1023/A:1010171315715.
(45) Snegirev, A. Yu.; Talalov, V. A.; Stepanov, V. V.; Harris, J. N. Formal Kinetics of Polystyrene Pyrolysis in Non-Oxidizing Atmosphere. *Thermochimica Acta* **2012**, *548*, 17–26. https://doi.org/10.1016/j.tca.2012.08.021.